# The Changjiang Estuary: A highly turbid estuary in transition

Lin, J.

**DOI**
10.4233/uuid:5cd38c3b-f0f5-405f-9f9f-02512ebb77dd

**Publication date**
2022

**Document Version**
Final published version

**Citation (APA)**
Lin, J. (2022). *The Changjiang Estuary: A highly turbid estuary in transition*. [Dissertation (TU Delft), Delft University of Technology]. https://doi.org/10.4233/uuid:5cd38c3b-f0f5-405f-9f9f-02512ebb77dd

# The Changjiang Estuary: A highly turbid estuary in transition

## Dissertation

for the purpose of obtaining the degree of doctor
at Delft University of Technology
by the authority of Rector Magnificus prof.dr.ir. T.H.J.J. van der Hagen
chair of the Board for Doctorates
to be defended publicly on
Wednesday 6 July 2022 at 10:00 o'clock

by

Jianliang LIN

Bachelor of Science in Marine Science and Coastal Engineering,
Sun Yat-sen University, China
born in Foshan, China

This dissertation has been approved by the promotors.

Composition of the doctoral committee:

| | |
|---|---|
| Rector Magnificus, | chairman |
| Prof.dr.ir. Z.B. Wang | Delft University of Technology, *promotor* |
| Prof.dr. Q. He | East China Normal University, *promotor* |
| Dr.ir. B.C. van Prooijen | Delft University of Technology, *promotor* |

Independent members:

| | |
|---|---|
| Prof.dr.ir. J.C. Winterwerp | Delft University of Technology |
| Prof.dr.ir. W.S.J. Uijttewaal | Delft University of Technology |
| Prof.dr. D.S. van Maren | Deltares and East China Normal University |
| Dr. F. Grasso | Ifremer, France |
| Dr.ir. C. Chassagne | Delft University of Technology, reserve member |

The doctoral research has been carried out in the context of an agreement on joint doctoral supervision between East China Normal University, China and Delft University of Technology, the Netherlands.

This work has been carried out as part of the Sino-Dutch collaboration project 'Coping with deltas in transition' funded by the Royal Netherlands Academy of Arts and Sciences (KNAW, No. PSA-SA-E-02) and the Ministry of Science and Technology of the People's Republic of China (No. 2016YFE0133700) within the Programme of Strategic Scientific Alliance between China and the Netherlands.


Printed by Ridderprint
ISBN 978-94-6458-315-1
An electronic version of this dissertation is available at
https://repository.tudelft.nl/.

*To my family*
*for patience and encouragement*

# Contents

# Summary

Many estuaries worldwide are engineered (e.g., dredging and reclamation) to accommodate city development. These human interventions affect hydro-morphodynamics adaptation, leading to changes in tidal range, sediment concentration, pollutant dispersal, primary production, flood risk and others. Although the regime shift from low- to hyper-turbid states is of increasing concern, hydrodynamic and sediment dynamic changes in estuaries with a significant river discharge remain unclear. In addition to local human interventions, fluvial sediment supply has declined worldwide due to the damming and irrigation in river basins, which may alter estuarine sediment dynamics. Based on the observations in the North Passage of the Changjiang Estuary, this thesis systematically investigated the response of sediment dynamics to declined fluvial sediment supply and local human interventions (e.g., deepening and narrowing).

One of the critical issues in identifying the transition from low to high turbidity is accessing accurate and reliable suspended sediment concentrations. However, the accurate measurement of sediment concentration in highly turbid environments has been a problem due to signal saturation and attenuation. The saturation returns a limited measurement range (<9 g/L), while the attenuation raises an ambiguity problem that a low optical or acoustic output could mean a low or a high sediment concentration. This thesis proposes an integrated optic and acoustic (IOA) approach to resolve the ambiguity problem and access high-resolution (1 cm) sediment concentration profiles. The sediment concentration given by ASM (optic) is preferred in this approach, as it has the lowest relative error (~25%). The OBS (optic) can recover the missing estimate when the ASM is saturated, with a relative error of ~30%. The ADV (acoustic) provides a rough estimation (relative error > 80%) and assists the OBS conversion. Since the ambiguity problem is solved, the measurement range is extended to >60 g/L.

The application in the Changjiang Estuary indicates the reliability of the IOA approach with a relative error of 17-34%. Concentrated benthic suspensions (10-80 g/L) were captured, and near-bed sediment concentration was up to 63 g/L. The sediment concentration profiles in the Changjiang Estuary exhibit seasonal variations. High sediment concentrations are confined in the benthic layer (within 2 m above the bed) in the wet season, whereas the suspension is well mixed throughout the water column in the dry season, returning a more uniform profile.

Observations from 1988 to 2015 were collected and analysed to reveal the sediment dynamics changes in the North Passage. During this period, the fluvial sediment load

decreased by ~70%, from 470 to 130 million tons per year (at Datong), while the yearly averaged river discharge (28,500 $m^3/s$) remained stable. In addition, a Deep Waterway Project (DWP) was conducted in the North Passage from 1998 to 2010, increasing channel depth from 6.5 m to 12.5 m. Meanwhile, the North Passage was narrowed with the expectation of strengthening flow velocities and reducing back siltation.

The observations show that the estuarine (gravitational) circulation and the stratification induced by salinity and sediment are strengthened after the DWP. The increases in estuarine circulation ($U_e$) vary along the North Passage, reaching the maximum in the middle and lower reaches where $U_e$ is more than 3-fold (up to ~0.3 m/s). The residual flows confirm the enhanced estuarine circulation. The outflows near the surface are up to 1.2 m/s, while the inflows near the bottom are up to 0.1 m/s. Both deepening and narrowing contribute to this enhanced estuarine circulation. Our analysis suggests that narrowing (estuary width) has effects as critical as deepening (channel depth) on the estuarine circulation by modifying eddy viscosity (stratification) and along-channel salinity gradient. The increases in (salinity- and sediment-induced) potential energy anomaly and gradient Richardson number indicate enhanced density stratification after the DWP. Tidally averaged salinity-induced potential energy anomaly is 3-fold (up to 140 $J/m^3$), and the sediment-induced is 30-fold to 330 $J/m^3$. Surprisingly, the stratification at the salt intrusion limit, where sediment from the river and sea converge, is dominated by suspended sediment.

The enhanced stratification triggers positive feedback between vertical mixing and hindered settling. Because of increased stratification, eddy viscosity and diffusivity reduce (i.e., turbulence damping). Vertical sediment mixing (resuspension) to the upper water column is thus suppressed, resulting in sediment accumulation near the bottom. With increasing sediment concentration, hindered settling becomes important and accelerates near-bed sediment accumulation. Consequently, considerable vertical gradients in sediment concentration (i.e., sediment-induced stratification) form, hence enhancing stratification. This positive feedback favours the formation and stability of concentrated benthic suspensions. A mobile pool of concentrated benthic suspension was detected after the DWP, with a tidally averaged length of ~20 km, a thickness of ~4 m and limited width of <1 km.

Concentrated benthic suspensions, driven by the strengthened near-bed inflows of estuarine circulation, produce significant landward sediment transport and generate sediment trapping at the salt intrusion limit. Along-channel sediment concentration gradients thus develop. In addition, flow velocity gradients are notable after the DWP, with higher flow velocity in the middle reaches than the upstream and the

downstream. Hence, dispersive flux (sediment concentration gradients) and spatial lag (velocity gradients) become important, resulting in the tidal pumping that drives the sediment transport from high-concentration (high-energy) to low-concentration (low-energy) regions. Overall, after the DWP, the sediment import/trapping is primarily controlled by the estuarine circulation, while the tidal pumping is responsible for the along-channel extension of the ETM.

Moreover, an integrated tripod system quantified the drag reduction by sediment concentrations. The drag/friction coefficient decreases with increasing suspended sediment concentrations when sediment concentrations < 10 g/L and maintains at its minimum (with a drag reduction of 60%) in the presence of concentrated benthic suspensions (10-80 g/L). The drag reduction predominately results from turbulence damping, whereas the drag increases because of increasing viscous stress at higher concentrations. In this range of concentrations, turbulence damping and viscous stress are equally important, leading to a nearly constant minimum drag coefficient. Hence, when the estuary shifts from low- to hyper-turbid states, the friction experienced by water motion significantly reduces, while the bed shear stress causing erosion maintains as high as in a low-turbid state. It implies that increased viscous stress is another mechanism supporting sediment in suspension in addition to hindered settling.

After the DWP, the changes in vertical sediment concentration profiles were observed, with decreasing concentrations in the upper water column and increasing near-bed concentrations. The increase near the bed is attributed to near-bed sediment accumulation by the above-mentioned positive feedback and along-channel sediment convergence by estuarine circulation. However, two processes are responsible for decreasing concentrations in the upper water column, i.e., declined fluvial sediment supply and reduced sediment mixing due to enhanced stratification.

Unlike the typical strain-induced periodic stratification, which implies stratification development during ebb tides and destruction during flood tides (Simpson et al., 1990), an unexpected strain-induced stratification was observed during the early flood tide. This stratification results from the reversed velocity shear, as the maximum flooding velocity occurs in the mid-lower layers. During the early flood tide, the salter water in the mid-lower layers moves faster than the fresher water near the surface, producing a stronger stratification. This stratification is amplified by the positive feedback (among stratification, turbulence damping and hindered settling) and sediment-induced stratification.

In summary, this thesis unveils several critical processes of sediment dynamics in response to the human interventions in estuaries with a large river discharge,

including quantifying the drag reduction, the changes in sediment concentration profiles, the sediment import/trapping by estuarine circulation and the ETM extension by tidal pumping. In addition, an IOA approach is proposed for measuring sediment concentrations in highly turbid environments. These insights and methods support the management of estuaries.

# Samenvatting *

Veel estuaria over de wereld zijn aangepast (bijvoorbeeld door baggeren en landaanwinning) om stadsontwikkeling mogelijk te maken. Deze menselijke interventies beïnvloeden de hydromorfodynamische aanpassing, wat leidt tot veranderingen in het getijverschil, sedimentconcentratie, verspreiding van verontreinigende stoffen, primaire productie, overstromingsrisico en dergelijken. Hoewel de regimeverschuiving van laag- naar hypertroebele toestand steeds zorgwekkender is, blijven hydrodynamica en sedimentdynamiekveranderingen in estuaria met een significante rivierafvoer onduidelijk. Bovendien is, naast lokale menselijke interventies, de aanvoer van riviersediment de afgelopen decennia wereldwijd afgenomen als gevolg van dammen en irrigatie in stroomgebieden, wat ook de dynamiek van estuariene sedimenten kan veranderen. Gebaseerd op de waarnemingen in de North Passage van het Changjiang-estuarium, wordt in dit proefschrift onderzocht wat de systematisch de reactie is van sedimentdynamiek op verminderde aanvoer van fluviaal sediment en lokale menselijke interventies (bijv. verdieping en vernauwing).

Een cruciaal punt bij het identificeren van de overgang van een lage naar een hoge sedimentconcentratie is toegang tot nauwkeurige en betrouwbare metingen. Nauwkeurige metingen van sedimentconcentraties in zeer troebele omgevingen waren echter een probleem vanwege signaalverzadiging en -verzwakking. De verzadiging levert een beperkt meetbereik op (<9 g/L), terwijl de demping een ambiguïteitsprobleem oproept dat bij een lage optische of akoestische output een lage of hoge sedimentconcentratie zou kunnen betekenen. Dit proefschrift stelt een geïntegreerde optische en akoestische (Integrated Optical and Acoustic = IOA) benadering voor om het ambiguïteitsprobleem op te lossen en toegang te krijgen tot sedimentconcentratieprofielen met een hoge resolutie (1 cm). De sedimentconcentratie gegeven door ASM (optisch) heeft de voorkeur in deze benadering, omdat deze de laagste relatieve fout heeft (~ 25%). De OBS (optisch) kan de ontbrekende schatting herstellen wanneer de ASM verzadigd is, met een relatieve fout van ~30%. De ADV (akoestisch) geeft een ruwe schatting (relatieve fout > 80%) en ondersteunt de OBS-conversie. Omdat het ambiguïteitsprobleem is opgelost, wordt het meetbereik uitgebreid tot >60 g/L.

De toepassing in het Changjiang-estuarium geeft de betrouwbaarheid van de IOA-benadering aan met een relatieve fout van 17-34%. Geconcentreerde benthische

* This abstract is translated from English to Dutch by Dr. Bram van Prooijen, but the author himself is responsible for the accuracy.

suspensies (10-80 g/L) werden opgevangen en de sedimentconcentratie in de buurt van het bed was tot 63 g/L. De sedimentconcentratieprofielen in het Changjiang-estuarium vertonen seizoensvariaties. Hoge sedimentconcentraties werden in het natte seizoen in de bentische laag (binnen 2 m boven de bodem) gevangen, terwijl de suspensie in het droge seizoen goed door de waterkolom werd gemengd, waardoor een meer uniform profiel werd verkregen.

Waarnemingen van 1988 tot 2015 werden verzameld en geanalyseerd om de veranderingen in de sedimentdynamiek in de North Passage te bepalen. Tijdens deze periode daalde de sedimentaanvoer vanuit de rivier met ~70%, van 470 naar 130 miljoen ton per jaar (bij Datong), terwijl de jaarlijkse gemiddelde rivierafvoer (28.500 $m^3/s$) stabiel bleef. Daarnaast is van 1998 tot 2010 een Deep Waterway Project (DWP) uitgevoerd in de North Passage, waardoor de geuldiepte is vergroot van 6,5 m naar 12,5 m. Ondertussen werd de North Passage versmald om de stromingen te versterken en aanslibbing te verminderen.

De waarnemingen laten zien dat de estuariene circulatie en de gelaagdheid veroorzaakt door zoutgehalte en sediment zijn versterkt als gevolg van de DWP. De toename van de estuariene circulatie (Ue) varieert langs de North Passage en bereikt het maximum in de midden- en benedenloop waar Ue meer dan driemaal zo groot is (tot ~0,3 m/s). Verbeterde estuariene circulatie wordt bevestigd door reststromen, met uitstromen nabij het oppervlak tot 1,2 m/s en instromen nabij de bodem tot 0,1 m/s. Zowel verdieping als vernauwing dragen bij aan deze versterkte estuariene circulatie. De gevoeligheidsanalyse suggereert dat de effecten van vernauwing even belangrijk zijn als van verdieping op de estuariene circulatie. Dit is het gevolg van aanpassing van de eddy-viscositeit (bijvoorbeeld stratificatie) en langsgradiënt in zoutgehalte. De toename van (zout- en sediment-geïnduceerde) *potential energy anomaly* en *gradient Richardson*-getal duiden op verhoogde dichtheidsstratificatie na de DWP. De getijdegemiddelde *anomaly* voor potentiële energie veroorzaakt door zoutgehalte is 3-voudig (tot 140 $J/m^3$) en de door sediment veroorzaakte afwijking is 30-voudig tot 330 $J/m^3$. Verrassend genoeg overheersen sedimentconcentraties de stratificatie nabij de zoutintrusiegrens waar het sediment uit rivier en zee samenkomt.

Verhoogde stratificatie activeert de positieve feedback tussen verticale menging en *hindered settling*. Door verbeterde gelaagdheid verminderen eddy-viscositeit en diffusiviteit (d.w.z. turbulentiedemping). Verticale opmenging van sediment naar de bovenste waterkolom wordt zo onderdrukt, wat resulteert in sedimentophoping nabij de bodem. Met toenemende sedimentconcentratie wordt *hindered settling* essentieel en versnelt de ophoping van sediment in de buurt van de bodem. Dientengevolge ontwikkelen zich significante verticale gradiënten van sedimentconcentratie (d.w.z.

door sediment geïnduceerde stratificatie) nabij de bodem, waardoor de stratificatie verder toeneemt. Een dergelijke positieve terugkoppeling bevordert de vorming en stabiliteit van geconcentreerde bentische suspensies. Een mobiele pool van geconcentreerde bentische suspensies werd gedetecteerd na de DWP, met een getijdengemiddelde lengte van ~20 km, een dikte van ~4 m en een beperkte breedte van <1 km.

Geconcentreerde bentische suspensies, aangedreven door een verhoogde instroom nabij de bodem van de estuariene circulatie, produceren significante landwaarts sedimenttransporten en genereren sedimentinvang bij de zoutintrusielimiet. Aldus ontwikkelen zich langs het kanaal sedimentconcentratiegradiënten. Bovendien is de stroomsnelheidsgradiënt significant na de DWP, met een hogere stroomsnelheid in het middengebied dan stroomopwaarts en stroomafwaarts. Daarom worden dispersieve flux (sedimentconcentratiegradiënten) en ruimtelijke vertraging (snelheidsgradiënten) essentieel, wat resulteert in *tidal pumping* dat sedimenttransport van hoge concentratie (hoge energie) naar lage concentratie (lage energie) gebieden drijft. Kortom, na de DWP wordt de sedimentimport/invang voornamelijk gecontroleerd door de estuariene circulatie, terwijl *tidal pumping* verantwoordelijk is voor de longitudinale uitbreiding van ETM.

Met behulp van een tripod meetsysteem is de weerstandsvermindering door sedimentconcentraties gemeten. Waarnemingen geven aan dat de weerstandscoëfficiënt afneemt bij toenemende sedimentconcentraties voor concentraties <10 g/L. Bij hogere concentraties (>80g/L) is de weerstandscoëfficiënt minimaal en onafhankelijk van de concentratie. De weerstandsvermindering is voornamelijk het gevolg van turbulentiedemping, terwijl de weerstand toeneemt door toenemende viskeuze spanning bij hogere concentraties. In dit concentratiebereik zijn turbulentiedemping en viskeuze spanning even belangrijk, wat leidt tot een bijna constante minimale weerstandscoëfficiënt. Dus wanneer het estuarium verschuift van een lage naar een hypertroebele toestand, vermindert de wrijving die wordt ervaren door waterbeweging aanzienlijk, terwijl de bodemschuifspanning die erosie veroorzaakt even hoog blijft als in een laagtroebele toestand. Het impliceert dat verhoogde viskeuze stress een ander mechanisme is dat sediment in suspensie ondersteunt, naast *hindered settling*.

Na de DWP werden veranderingen in het verticale sedimentconcentratieprofiel waargenomen, met afnemende concentraties in het bovenste deel van de waterkolom en toenemende concentraties nabij de bodem. De toename in de buurt van de bodem wordt toegeschreven aan de accumulatie van sediment in de buurt van de bodem door de bovengenoemde positieve feedback en convergentie van sediment langs het kanaal door estuariene circulatie. Er zijn echter twee processen

verantwoordelijk voor de afnemende concentraties in de bovenste waterkolom, namelijk de verminderde aanvoer van sediment vanaf de rivier en verminderde menging van sediment door sterkere gelaagdheid.

Verrassend genoeg ontwikkelt zich tijdens de vroege vloed een door spanning geïnduceerde gelaagdheid, die verschilt van de klassieke door spanning geïnduceerde periodieke stratificatie die de ontwikkeling van gelaagdheid tijdens eb en vernietiging tijdens vloed suggereert (Simpson et al., 1990). Deze gelaagdheid is het gevolg van de omgekeerde snelheidsschuifkracht, aangezien de maximale overstromingssnelheid optreedt in de midden-lagere lagen. Tijdens de vroege vloed beweegt het zoute water in de middelste lagere lagen sneller dan het zoetere water aan de oppervlakte, waardoor een sterkere gelaagdheid ontstaat. Deze gelaagdheid wordt versterkt door de positieve feedback (onder gelaagdheid, turbulentiedemping en belemmerde bezinking) en sediment-geïnduceerde gelaagdheid.

Samenvattend behandelt dit proefschrift verschillende kritische processen van veranderingen in sedimentdynamiek als reactie op menselijk ingrijpen in estuaria met een grote rivierafvoer, zoals kwantificering van weerstandsvermindering, veranderingen in sedimentconcentratieprofielen, sedimentimport/invang door estuariene circulatie en ETM-uitbreiding door *tidal pumping*. Daarnaast is een IOA-benadering ontwikkeld voor het meten van sedimentconcentratie in zeer troebele omgevingen. Deze inzichten en methodes kunnen gebruikt worden om het beheer van deze complexe estuariene systemen te verbeteren.

# 摘要

河口是陆海相互作用的核心区域，具有重要的自然生态和社会经济价值。其中，水沙动力是控制河口地貌演变、通航能力以及初级生产力的关键过程。20 世纪初以来，不断加剧的人类活动，如流域筑坝、河口浚深、滩涂围垦等，给河口带来了巨大压力，驱动河口泥沙动力场的格局转换。然而，该格局转换多发生于潮控河口（如 Ems 河口和 Loire 河口）。大径流的河口（如长江口）如何响应的机制尚不清楚，并且叠加流域减沙的作用，导致此类河口的格局转换的过程和主控因子甄别更为复杂。**本论文重点探究在流域减沙和河口深水航道等工程背景下河口最大浑浊带的水沙动力场格局转换，主要贡献包括：（1）构建基于声学和光学探头集成的宽量程高精度的泥沙浓度观测系统；（2）阐明长江口航道泥沙浓度剖面的格局转换特征演化过程，量化给出近底高浓度的发育机制及其制紊减阻效应；（3）揭示河口窄深化对最大浑浊带泥沙输运及演化的控制机制。**

**（1）构建高浊度河口泥沙浓度多探头高精度集成观测系统**

准确、高效地测量泥沙浓度是研究泥沙输运的重要基础，同时也是探究河口泥沙浓度格局转换的关键技术。常用仪器包括光学后向散射浊度计（OBS），高分辨率剖面浊度仪（ASM）和声学多普勒点流速仪（ADV），三者反演泥沙的精度由高到低为 ASM、OBS、ADV，误差分别为 25%、30%、90%。此外，ASM 可反演的饱和泥沙浓度约为 9 g/L；OBS 和 ADV 在高浓度中存在信号衰减问题，导致反演的不确定性。因此单一仪器对泥沙浓度的反演存在量程小、精度低和阈值难以判断等关键问题，制约对河口近底高浓度输沙过程和机理的认识。

本文根据 ASM、OBS 和 ADV 对泥沙浓度响应及阈值的不同，综合各自优势，提出了一套多探头集成观测泥沙浓度的方法（IOA 法），即当 ASM 未饱和时，由 ASM 反演泥沙浓度；ASM 饱和后，由 OBS 提供反演结果；ADV 协助提高 OBS 的反演精度并提供高频泥沙浓度。这一方法通过多探头集成互较，可以有效克服 OBS 和 ADV 信号反演中的不确定性问题，获取高量程和高精度的泥沙浓度。在长江口的应用研究表明，相比传统观测方法，IOA 方法可提高测量精度至相对误差 25%，扩展量程至>60 g/L，并提供高分辨率（1 cm）的泥沙浓度剖面。此方法成功获取长江口北槽近底浓度高于 10g/L 的剖面。该集成观测系统的构建为探讨河口水沙格局转换和近底高浓度发育机制奠定了基础。

**（2）阐明长江口航道水沙动力格局转换特征，量化近底高浓度的制紊减阻效应**

近年来，长江口的流域来沙已大幅下降 70%。1998 年至 2010 年，河口深水航道工程导致主槽窄深化：航道水深从 6.5 m 增加到 12.5 m，并通过丁坝束窄了北槽。在此背景下，河口泥沙浓度的变化特征及高浓度的发育机制是应对河口格局转换的关键问题，而高浓度的制紊减阻效应是控制河口泥沙浓度格局转变的关键过程。

研究表明，**河口浑浊带表层泥沙浓度降低，而近底浓度显著增大。**其中，近底高浓度的发育归因于航道工程（即窄深化）触发的密度层化、紊动制约和受阻沉降之间的正反馈机制：河口的窄深化引起水体密度分层增强，进而制约垂向紊动扩散，导致泥沙在近底聚集。随着泥沙浓度的增加，阻滞沉降效应愈发显著，有助泥沙的悬浮，并产生显著的垂向浓度梯度（即泥沙诱导的密度分层），从而进一步增强层化。这种正反馈机制有利于近底高浓度的形成和稳定。深水航道工程后，长江口北槽发育了可移动的近底高浓度泥沙库，平均长度约 20 km，平均宽度小于 1 km，平均厚度约 4 m，主要集中在航槽中段和南侧，分别受憩流不对称和横向流不对称的影响，对疏浚区和抛泥区的设计和管理具有重要的指示意义。表层泥沙浓度的下降有两方面原因：（1）深水航道工程导致密度层化的增强，抑制河口垂向混合和泥沙悬扬；（2）流域减沙导致低浓度水体输送到河口，稀释了河口的表层泥沙浓度。

**基于多探头高精度集成观测系统的近底边界层原位观测，量给出泥沙浓度制紊减阻效应。**结果表明：（1）在低浓度（<10 g/L），摩阻系数随泥沙浓度的增加而近于线性下降；（2）高浓度时（10-80 g/L），摩阻系数达到最小（减阻高达 60%）。摩阻的减小主要是由于（盐度或泥沙）层化对湍流的抑制，而高浓度时粘性应力的增加则可引起摩阻的增加。在 10-80 g/L 的浓度范围内，湍流应力和粘性应力相当，导致摩阻系数近于恒定并达到最小值。这表明，当河口从低浊度转变为高浊度时，虽然上层水体运动所受的摩擦力会显著减小，但增大的粘性应力可使聚集的泥沙维持悬浮，即除阻滞沉降之外，粘性应力的增大是维持近底高浓度的另一机制。

**（3）揭示河口窄深化对最大浑浊带泥沙输运及发育演变的控制机制**

长江口深水航道的多站点同步观测结果表明，**河口重力环流和盐度于泥沙诱导的密度分层在深水航道工程后显著增强。**河口环流的增加在北槽中下段达到最大值，其量值增加 3 倍以上（达到 0.3 m/s）。表层向海余流高达 1.2 m/s，底层向陆余流可达 0.1 m/s。窄深化是河口环流增强的主要原因。束窄通过增强密度分层（减小涡粘系数）和增大沿河口的盐度梯度来增强河口环流。深水航道工程后，盐度和泥沙导致的密度分层势能分别增强了 3 倍（140 J/m$^3$）和 30 倍（高达 330 J/m$^3$），且泥沙密度分层在近底和盐水楔前缘占主导地位。

**河口环流是航道工程后口外泥沙输入和近底高浓度发育的主要动力。**河口的窄深化触发了密度层化、紊动制约和受阻沉降之间的正反馈机制，导致泥沙在近底的聚集，形成近底高浓度。近底高浓度在增强的河口环流驱动下产生显著的向陆泥沙输运，并在盐水楔前缘形成泥沙辐聚。此外，近底高浓度发育引起纵向泥沙浓度梯度显著增大，加之深水航道工程后北槽中段的流速高于上、下游，产生较大的纵向流速梯度。泥沙浓度梯度和速度梯度导致潮泵输运显著增加，促使近底高浓度的纵向延伸。

综上所述，本论文提出的多探头高精度集成观测系统为研究河口水沙动力格局转换、近底高浓度泥沙输运提供了重要的技术支撑。基于自主研发的坐底三脚架观测系统，量化了高泥沙浓度的制紊减阻效应，阐明了长江口近底高浓度的发育机制：密度层化、紊动制约和受阻沉降之间的正反馈。通过比较深水航道工程前后的泥沙输运机制，明晰了河口环流是主导泥沙从口外输入河口的主要动力，而潮泵作用驱动最大

浑浊带沿航道的延伸。这些研究成果加深了对径潮流共同作用高浊度河口水沙格局转换的认识，为河口生态系统的高效管理提供了理论基础。

# 1. Introduction

*No research without action;*
*No action without research.*

Kurt Lewin

*Research is formalized curiosity.*
*It is poking and prying with a purpose.*

Zora Neale Hurston

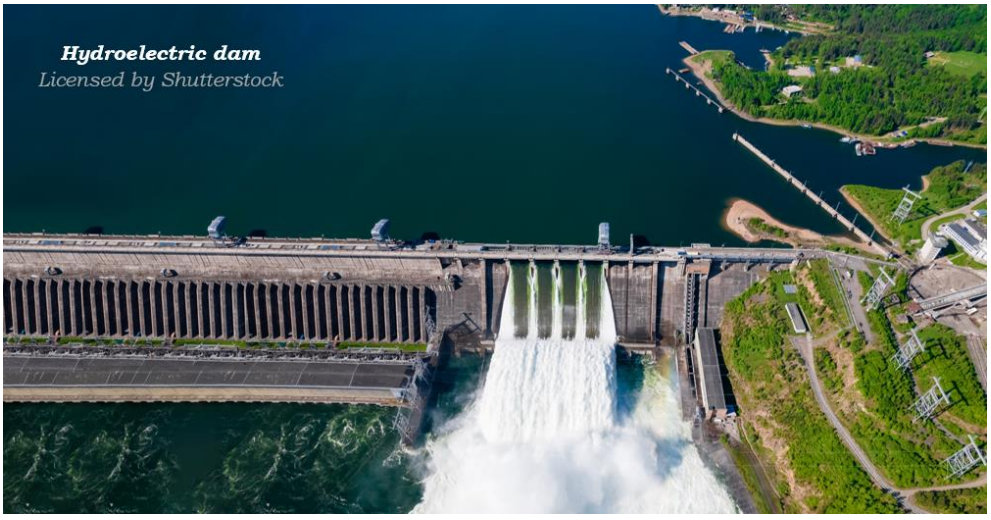

## 1.1. Estuaries in transition

The ecological and economic values of estuaries are subject to tremendous environmental and anthropogenic changes globally (Neumann et al., 2015). Since the beginning of the 20th Century, human society has developed rapidly, with a surge in population and human activities. In particular, large cities developed and expanded around estuaries, e.g., New York and Shanghai (Figure 1-1). Increasing human population and activities impose significant pressures on estuaries, leading to anthropogenic-driven environmental changes (Rockström et al., 2009; Waters et al., 2016). These pressures include but are not limited to (1) modification of seabed and habitats (e.g., land reclamations, sand mining and harbour dredging); (2) modification of water cycle (e.g., dam construction, river diversion and freshwater abstraction); (3) climate change and related sea-level rise and stronger coastal storms (Rockström et al., 2009; Parmesan et al., 2013; Little et al., 2017; Elliott et al., 2019). Note that these pressures are not independent but link and interact with each other. They can generate cumulative, synergistic and antagonistic effects on estuaries over a range of spatial and temporal scales (Steffen et al., 2007; Brown et al., 2013; Elliott et al., 2019), see Figure 1-2. This thesis focuses specifically on dredging and reclamation in estuaries.


*Figure 1-1: The development of cities around estuaries. The top panels show New York in (a) 1609 and (b) 2009 (Image courtesy: Ken Ashford). The bottom panels show Shanghai in (c) 1987 and (d) 2013 (Image courtesy: Carlos Barria).*

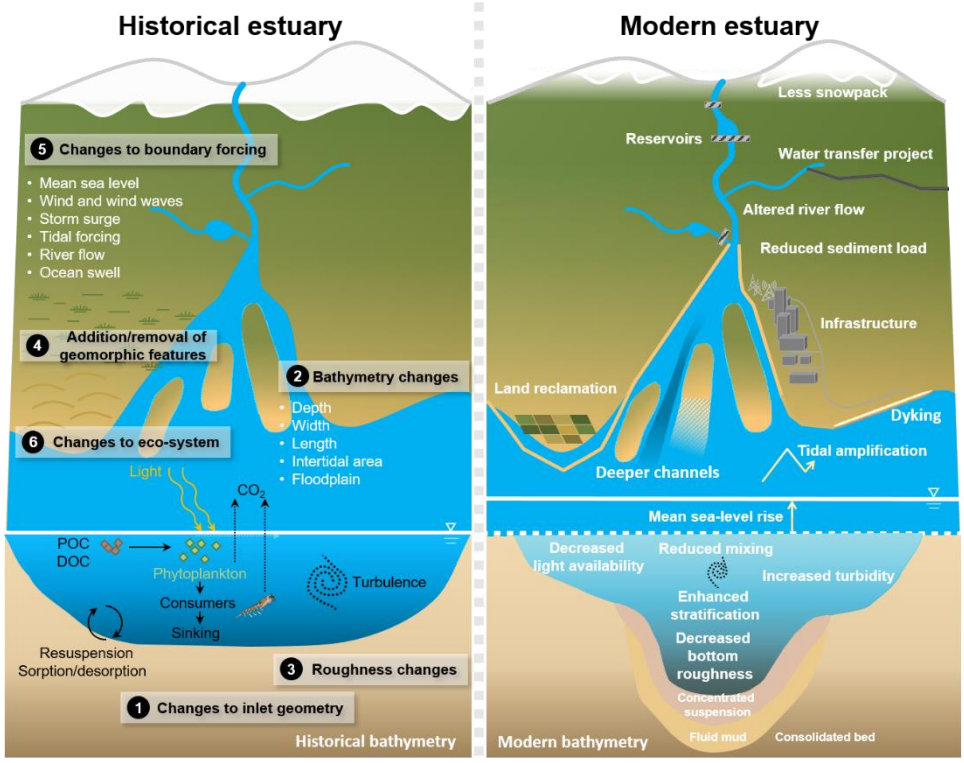


*Figure 1-2: Schematic of natural and anthropogenic changes within rivers, estuaries, and coastal embayments that can lead to an evolution in community structure and functioning, modified from Talke and Jay (2020).*

An estuary is a semi-enclosed coastal body of water with a free connection to the open sea, where saltwater from the ocean mixes with fresh water from rivers and streams (Pritchard, 1967; Valle-Levinson, 2010; Geyer and MacCready, 2014). Estuaries and their surrounding lands function as transition zones between riverine and maritime environments (Figure 1-2). Therefore, estuaries are subject both to marine forces, such as tides, waves, and the influx of saltwater and to fluvial influences, such as inputs of freshwater and sediment (Dalrymple et al., 1992). The mixing pattern between saltwater and freshwater varies between different estuaries and generally depends on the volume of freshwater and the tidal range in the estuary. According to the mixing condition, four categories of estuaries are distinguished (Cameron and Pritchard, 1963; Valle-Levinson, 2010), see Figure 1-3: salt wedge (e.g., Mississippi), strongly stratified (e.g., Fraser), partially mixed (e.g., Changjiang) and well mixed (e.g., Western Scheldt) estuaries.

Estuaries provide services with significant ecological and economic value. They play an important role in biodiversity and biogeochemical cycles regarding ecological

value. Rivers and tides bring a wealth of nutrients to estuaries, which provide a foundation for biological growth, making estuaries among the most productive ecosystems on the earth (Cloern et al., 2014; Elliott et al., 2019). As a transition zone from land to sea, terrestrial and marine species are extremely rich in estuaries, forming a vast and complex food web. The food web, combined with estuarine hydrodynamics and sediment dynamics, processes significant quantities of organic matter and controls the fluxes of carbon, nitrogen, phosphorus and heavy metals to the coastal ocean (Bianchi, 2006; Canuel and Hardison, 2016; Cai et al., 2021). In terms of economic value, estuaries support productive fishing and shipping. Estuaries and coastal seas produce almost half of global fish catch, although their areas are only a tiny fraction (~5%) of the marine and brackish regions (Palomares and Pauly, 2019). Moreover, estuaries are crucial hubs for ships accessing inland ports, supporting global trading and city development (van Koningsveld et al., 2021).

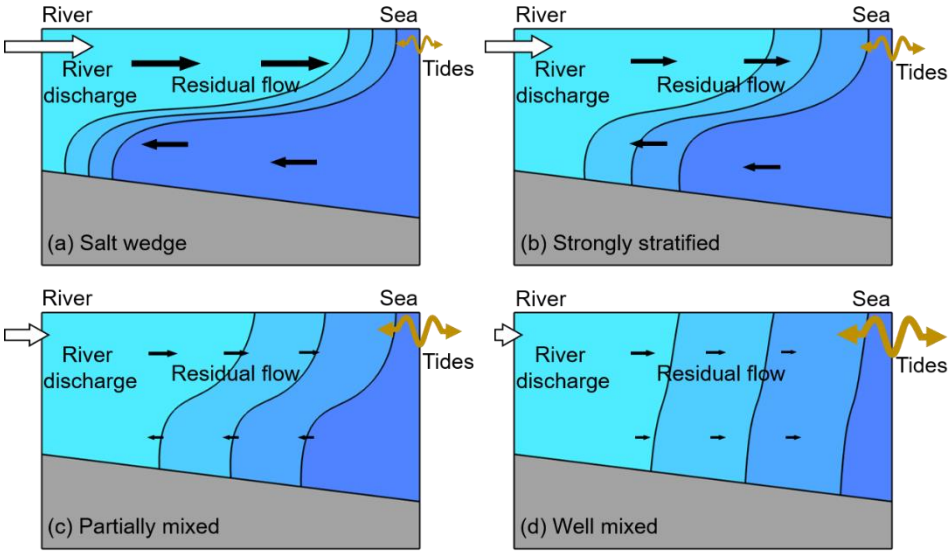


*Figure 1-3: Sketch of tidally-averaged salinity profiles in a (a) salt-wedge, (b) strongly stratified, (c) weakly stratified and (d) well-mixed estuary with different tidal forcing (tidal range and tidal currents) and river discharge.*

Many estuaries worldwide have been reclaimed for urban expansion and deepened to accommodate larger ships. These engineering works alter estuarine hydrodynamics and sediment dynamics and upset the natural balance of estuarine ecosystems. For example, increased suspended sediment concentrations in the Ems River (Netherlands, Germany) and Loire River (France) were observed after the channel deepening. This transition in sediment concentration is the so-called regime shift in estuaries from low-turbid to hyper-turbid states (Winterwerp and Wang,

2013; Winterwerp et al., 2013). High sediment concentration limits the light availability to benthic phytoplankton and produces a low level of oxygen (i.e., hypoxia), degrading the living conditions for estuarine organisms (Uncles et al., 1998; Talke et al., 2009a; Cloern et al., 2014; Winterwerp et al., 2017). In addition, the high siltation in channels and harbour basins is often related to the formation of concentrated benthic suspensions (Liu et al., 2011; de Nijs, 2012). Therefore, frequent dredging is required to maintain the high navigability in estuaries after deepening, which is costly.

Based on the observations in other European estuaries, e.g., Elbe (Germany) and Scheldt (Netherlands, Belgium), Winterwerp et al. (2013) suggested that these estuaries would be at the risk of hyper-turbid if they are further narrowed and deepened. It is worth noting that these estuaries are tide-dominated, with relatively small freshwater discharge and sediment load from the river (Winterwerp et al., 2013). However, observational or modelling evidence for changing sediment dynamics due to deepening is scarce in estuaries with a large freshwater discharge. Therefore, no one is confident about whether the regime shift would occur or not in this kind of estuary. Moreover, the river flow supplies sediment to these estuaries. Due to dam construction and irrigation, the fluvial sediment supply has declined in recent decades (Syvitski et al., 2005; Besset et al., 2019; Li et al., 2020a). Therefore, contrary to the regime shift (i.e., increasing sediment concentration) induced by deepening, decreased fluvial supply may reduce estuarine sediment concentrations. It is unclear how the sediment concentration changes in strongly intervened estuaries with a large river discharge (e.g., the Changjiang, Mekong or Mississippi).

## 1.2. Estuarine sediment dynamics

A better understanding of estuarine sediment dynamics is the key to predicting, preventing, or mitigating increasing sediment concentrations in estuaries. Estuarine hydrodynamics and sediment dynamics vary in time and in all three spatial dimensions. First, freshwater discharge interacts with denser seawater, resulting in vertical circulation patterns that capture and recirculate suspended sediment. Second, tides rise and fall, causing flow velocities to wax, wane and reverse direction in diurnal or semi-diurnal cycles. Third, ocean waves propagate into estuaries, joining locally generated wind waves to stir the bottom sediment and produce longshore currents and sediment transport. Moreover, wind-induced currents and storm surges may complicate these hydrodynamics and sediment transport processes.

Systematically studying the processes that contribute to estuarine sediment dynamics will help us better understand the regime of sediment dynamics and how

it evolves in response to the changing conditions in estuaries. Since this thesis is concerned with long-term dynamics, intra-tidal variations are filtered out, and the focus is instead on tidally averaged (subtidal) sediment transport processes. An overview of tidally averaged processes (e.g., estuarine circulation, tidal pumping and barotropic flux) that have been described in the literature is given in this section.



### 1.2.1. Estuarine circulation

In estuaries where seawater and riverine freshwater meet, seawater tends to intrude beneath the freshwater outflow, implying that the deeper water moves into the estuary below the outflowing surface layer. This bidirectional flow is known as the estuarine circulation, also called the gravitational circulation or exchange flow (MacCready and Geyer, 2010; Geyer and MacCready, 2014). The estuarine circulation has two distinctive features. First, regardless of the net seaward flow through any cross-section due to the river flow, the deeper part of the water typically flows landward. Second, quantified as a volume flux, the estuarine circulation is often several times greater than the river flow, highlighting its importance (MacCready and Geyer, 2010).

Initially, it was believed that the estuarine circulation was typically generated by horizontal salinity gradients (Hansen and Rattray, 1965). In tidally energetic systems, however, several additional mechanisms are recognized as critical contributors to the formation of estuarine circulation. These mechanisms are related to internal tidal asymmetry (Jay and Musiak, 1994; Stacey, 1996) or lateral rectification of along-channel momentum (Lerczak and Geyer, 2004; Becherer et al., 2015; Schulz et al., 2015). Both mechanisms work similarly by creating the ebb-flood asymmetry in the vertical profile of along-channel velocities, which results in a tidally averaged flow with a vertical structure similar to that of classical gravitational circulation (Lerczak and Geyer, 2004). These flows are called eddy viscosity-shear covariance (ESCO) circulation (Burchard et al., 2013; Dijkstra et al., 2017). Particularly in well-mixed and highly energetic systems, it is more critical than gravitational circulation in the formation of estuarine circulation (Burchard and Hetland, 2010; Burchard et al., 2011; Schulz et al., 2015; Wei et al., 2018). Additionally, it has been shown recently that circulation in the lateral direction affects the along-channel flow and hence estuarine circulation (Lerczak and Geyer, 2004; Huijts et al., 2009; Burchard and Schuttelaars, 2012; Schulz et al., 2015; Zhu et al., 2018). Furthermore, high sediment concentrations play an important role in water density, thus contributing to estuarine circulations (Talke et al., 2009b; Zhu et al., 2021b).

Estuarine circulation is critical for fine sediment transport and sedimentation. Postma and Kalle (1955) were probably the first to observe the upstream sediment transport driven by estuarine circulation on a tidally averaged scale. The up-estuary near-bottom flow traps a significant portion of the downstream fluvial sediment flux, leading to sediment accumulation at the salinity intrusion limit. Therefore, an estuarine turbidity maximum (ETM) develops (Festa and Hansen, 1978; Burchard et al., 2018). The up-estuary near-bottom flow also contributes to importing marine sediment into estuaries. During periods of low flow velocity, this sediment settles on the bed. It is resuspended during high tidal currents, causing a significant rise in turbidity.

### 1.2.2. Tidal pumping

Among tidally averaged sediment transport mechanisms, estuarine circulation is not the only mechanism for up-estuary sediment transport. Tidal pumping is equally vital in tidally energetic estuaries with significant tidal asymmetries in velocity and sediment concentration (Allen et al., 1980; Uncles et al., 1985; Geyer et al., 2001; Scully and Friedrichs, 2007; Chernetsky et al., 2010; McSweeney et al., 2016; Becherer et al., 2016). Tidal pumping results from three contributors: (1) temporal asymmetries (i.e., differences between ebb and flood tides) in flow velocity, sediment concentration, or water level; (2) temporal lag (i.e., the delayed response of concentration to locally varying flow velocity); and (3) spatial lag (associated with horizontal gradients) of flow velocity and sediment concentration.

Temporal asymmetries in flow velocity, sediment concentration, and water level can be formed by non-linear tidal propagation in shallow water (Friedrichs, 2010). Temporally asymmetric flow (e.g., stronger flood currents than ebb currents) includes non-linear advection, unbalanced return flow and the flow induced by asymmetric external tidal forcing (Chernetsky et al., 2010; Kumar et al., 2017). Since sediment resuspension and deposition are both velocity-dependent processes, each contribution to the asymmetric flow results in an asymmetric sediment concentration. Tidal variations in settling velocity (e.g., flocculation (Winterwerp, 2011)) can cause additional temporal asymmetry in the vertical sediment distribution, turbulence, or sediment availability from the bed. Strain-induced periodic stratification (SIPS) is an example of tidal variations in turbulence (Simpson et al., 1990). The SIPS leads to more sediment mixed higher up into the water column during flood than during ebb. As a result, sediment is transported more easily during flood than during ebb, resulting in net up-estuary sediment transport (Burchard and Baumert, 1998; Scully and Friedrichs, 2003).

Similarly, the influence of sediment on density causes variations in turbulence, known as mud-induced periodic stratification (MIPS) (Becker et al., 2018), which also leads to net up-estuary sediment transport following the same reasoning. Furthermore, the asymmetry in the sediment availability from the bed (known as the scour lag) can develop if the critical shear stress for deposition is less than the critical shear stress for erosion (Dyer, 1997; Gatto et al., 2017). This asymmetry contributes to the temporal asymmetry in sediment concentration, resulting in tidally averaged sediment transport.

Even without temporal asymmetries in velocity, eddy diffusivity, or sediment availability, tidal pumping can occur due to the spatial or temporal lag of sediment transport (see Postma, 1954; van Straaten and Kuenen, 1957). These lag effects include four sub-mechanisms: settling lag, threshold lag, entrainment lag, and slack water asymmetry (Gatto et al., 2017). The concept of settling lag is based on the interaction of non-vertical settling trajectories and the time lag between when a particle starts sinking and when it touches the bed. For example, with horizontal gradients of flow velocity, the settling lag produces sediment transport towards the locations with the lowest tidal velocity amplitude or sediment concentration (Friedrichs, 2010; Gatto et al., 2017). It is, therefore, a particularly effective trapping mechanism near the landward limits of bays and estuaries where the tidal velocity reduces to a nil value. Note that assuming a critical velocity (bed-shear stress) for erosion is not necessary for settling lag.

Nonetheless, settling lag is enhanced by a mechanism known as threshold lag (Gatto et al., 2017). Due to the landward damping of tidal currents, the time of re-entrainment during ebb tide (i.e., when the velocity of the driving water parcel reaches the erosion threshold) will be gradually delayed, leading to a progressive landward displacement after each tidal cycle. Compared to a no-lag situation, settling lag enhances advection by delaying deposition in adjacent control volumes, whereas threshold lag reduces advection by restricting erosion. The entrainment lag consists of the time required for a particle to pass through the bed-load layer and be lifted into the water column after being picked up from the bed (Nichols 1986). Slack-water asymmetry is also known as acceleration/deceleration asymmetry (Gatto et al., 2017). A longer slack after high water than after low water, for example, suggests that sediment has more time to settle at the end of flood tides than at the end of ebb tides, leading to a net up-estuary sediment transport.

### 1.2.3. Barotropic flux

Following the decomposition of velocity and sediment concentration into a tidal average and a remaining part, it is possible to divide the tidally averaged sediment

flux into an advective contribution and a tidal pumping contribution (Geyer et al., 2001; Scully and Friedrichs, 2007; Burchard et al., 2013; McSweeney et al., 2016). By vertical integration, the advective flux can be subdivided into two main contributions: a barotropic flux and a component that is purely driven by estuarine circulation. The barotropic flux includes all contributions of residual barotropic flows, e.g., river discharge, barotropic ebb-flood asymmetries and wind stress (Becherer et al., 2016).



## 1.3. The Changjiang (Yangtze) Estuary

The Yangtze River starts from Qinghai Province in western China and eastwards into the East China Sea. Various sections of the Yangtze River have their local names. At its source, the river is known as the Dangqu (当曲, literally "marsh river" from the Tibetan). It runs through deep gorges parallel to the Mekong and the Salween before emerging onto the plains of Sichuan, which is famous as the Jinsha River (金沙江). The "Yangzi River", from which the English name Yangtze is derived, is the local name for the lower Yangtze in Yangzhou. Because it was the name first heard by missionaries and traders, it was applied in English to the entire river (Jamieson, 1911). The Yangtze River is the longest river in Asia and the third-longest river on the earth, with a length of 6,300 km. This gives it the modern Chinese name, Chang Jiang (长江, pinyin: Cháng Jiāng), literally meaning "long river". The Yangtze River is thus also called the Changjiang River. This name is increasingly being adopted as the common name in English.

In terms of river discharge and sediment load, the Changjiang River is the largest river in Asia and among the largest rivers in the world. The daily freshwater discharge ranges between 6,000 and 92,000 $m^3/s$ at Datong, with a long-term (1950-2010) average of ~28,500 $m^3/s$ (CWRM, 2015). The annual sediment load has an average of 390 million tons (1953-2014) (CWRM, 2015). Both river discharge and sediment load exhibit seasonal variations. The discharge is approximately 41,000 $m^3/s$ in the wet season (May-October) and 16,500 $m^3/s$ in the dry season (November-April) (CWRM, 2015). More than 70% of sediment load is delivered to the estuary in the wet season. Due to the soil conservation strategies and dam constructions, the annual sediment load declined from 470 (1953-1985) to 132 (2003-2015) million tons (Guo et al., 2019), while no significant change was shown in the long-term average of river discharge (Guo et al., 2018), see Figure 1-5a.

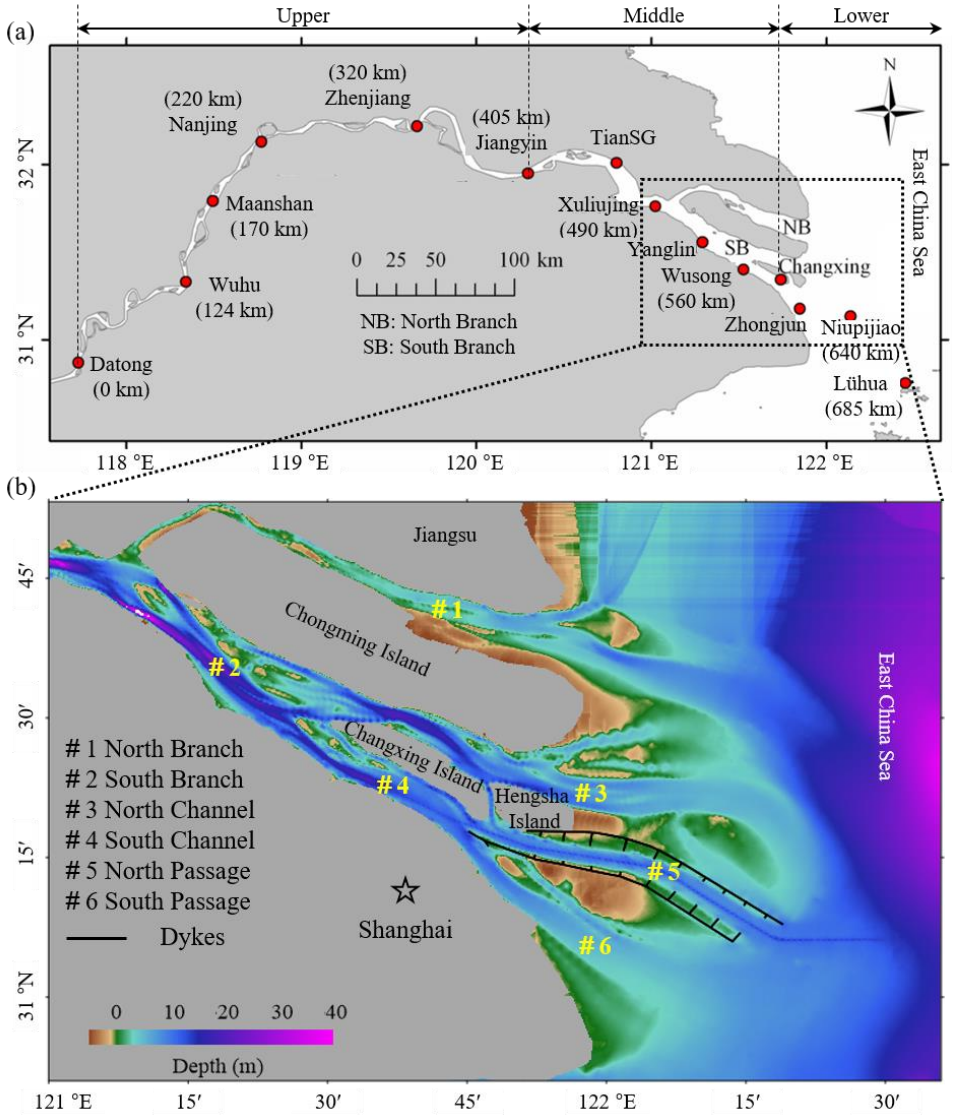


*Figure 1-4: (a) The topography of the Changjiang Estuary and the location of the tidal gauge stations. (b) The bathymetry of the middle and lower Changjiang Estuary.*

The Changjiang Estuary is the mouth of the Changjiang River, located in eastern China, with four outlets (i.e., North Branch, North Channel, North Passage, and South Passage) to the East China Sea (Figure 1-4). It stretches from Niupijiao to Datong, where the tidal wave limit (approximately 640 km upstream) is located. The width at the mouth of the estuary is about 90 km. The estuary is traditionally divided into three reaches (Figure 1-4), based on along-estuary variations of fluvial and tidal

energies (Guo, 2014). The part between Datong and Jiangyin (the tidal current limit) is the upper estuary where river forcing is dominant. River and tidal forcings are equally vital in the middle estuary between Jiangyin and Zhongjun. This thesis mainly focuses on the lower Changjiang Estuary (seaward of Changxing), where tidal forcing is predominant while the river force still plays a role.

According to the magnitude of tidal ranges, the lower Changjiang Estuary has a meso-tidal regime. At Niupijiao, the mean tidal range is 2.7 m. Since the tidal wave damps upstream, the tidal range decreases landward to 2.4 m at Xuliujing, 1.6 m at Jiangyin and 0.7 m at Nanjing (Guo et al., 2015). The lower Changjiang Estuary is partially mixed with combined river and tidal forcing. River discharge is the main factor controlling the stratification on a seasonal scale, while spring-neap tidal changes determine the stratification on a fortnightly scale (Wang et al., 2010; Pu et al., 2015). The estuary is well mixed when river discharge is extremely low (on spring tides), whereas it is strongly stratified with a high river discharge (on neap tides) (Pu et al., 2015).

Massive riverine sediment is supplied into the mouth zone, forming one of the most remarkable ETMs in the world. More than 95% of suspended sediment is fine sediment in the Changjiang Estuary, and the median size of suspended sediment is approximately 10 μm (CWRM, 2015). Since the freshwater moves seaward on the surface and the saline seawater intrudes landward near the bottom, a classical gravitational circulation develops in the lower Changjiang Estuary (Shen et al., 1982; Liu et al., 2011; Song and Wang, 2013; Li et al., 2016). This estuarine circulation is one of the controlling mechanisms for sediment trapping, forming a remarkable turbidity maximum at the saltwater intrusion limit (Shen et al., 1993; Shi, 2010; Liu et al., 2011; Shen et al., 2020). In addition to estuarine circulation, tidal pumping, flocculation, and resuspension contribute to the formation and maintenance of turbidity maximum in the Changjiang Estuary (Su and Wang, 1986; Li and Zhang, 1998; Shi, 2004; He et al., 2008; Jiang et al., 2013; Y. Li et al., 2018; Li et al., 2021).

In order to accommodate city development, many projects have been constructed in the Changjiang Estuary (Figure 1-5). The most famous one is the Deep Waterway Project (DWP). With progressive sediment trapping, mouth bars develop in the ETM zone, resulting in limited water depth of the estuary. In order to allow larger ships access to inland ports, the DWP (with deepening and narrowing) has been conducted in the North Passage (Figure 1-5). The DWP was launched in 1998 and developed the water depth in three phases: (1) to 8.5 m in 2002, (2) to 10 m in 2005 and (3) to 12.5 m in 2010. In addition, the training works include two 50-km-long dams parallel to the channel and 19 groins perpendicular to the channel. After these

constructions, the navigational channel has a width of 350-400 m, maintained at a depth of 12.5 m by regular dredging.

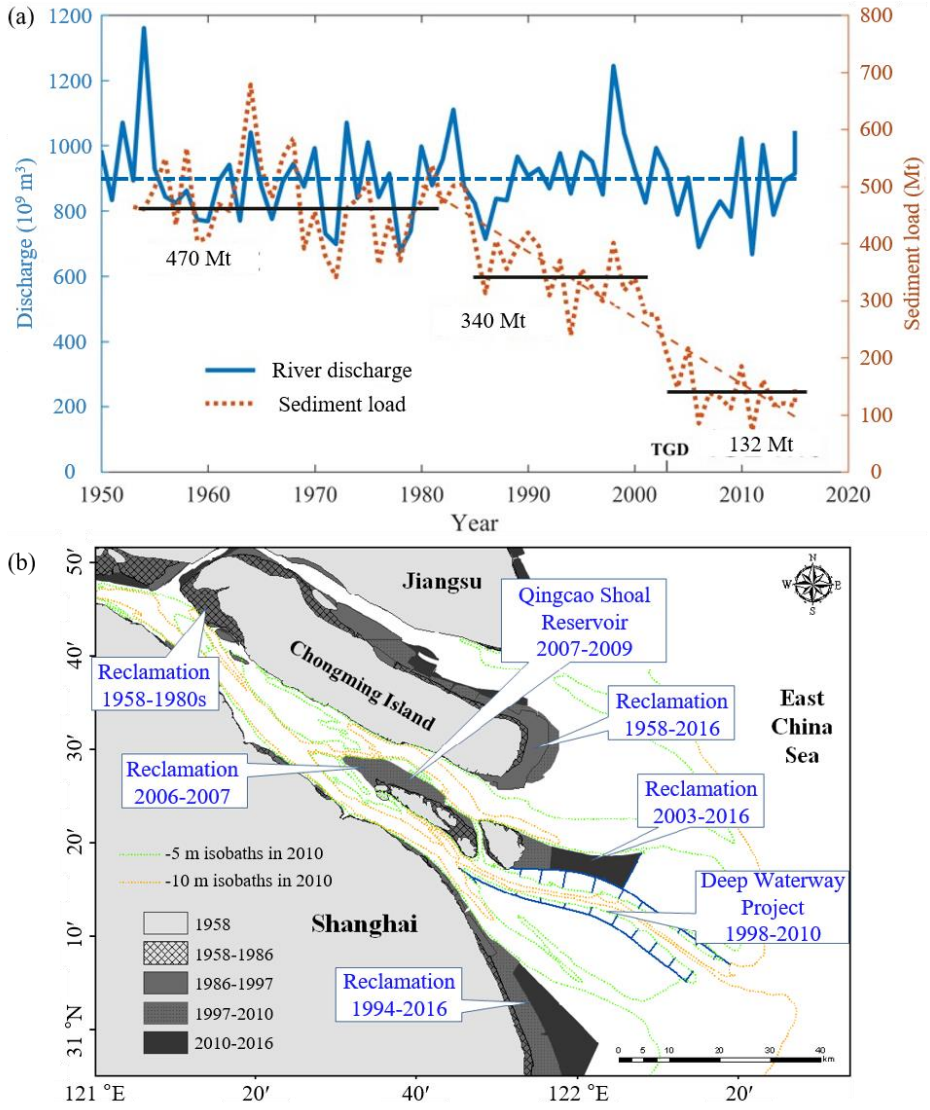


*Figure 1-5: (a) Annual river discharge and suspended sediment load measured at Datong (the most downstream gauging station) between 1950 and 2016. (b) The change of the shorelines and main large hydraulic constructions in the Changjiang Estuary.*

The excavation of mouth bars enhances the saltwater intrusion and stratification, leading to an extended turbidity maximum zone that migrates upstream (Zhu et al., 2006; Wang et al., 2010; Jiang et al., 2013; Song and Wang, 2013; Li et al., 2020b). The turbidity maximum is relatively well-mixed over the water column in the dry season, whereas it is more concentrated near the bottom in the wet season (Wu et al., 2012; L. Li et al., 2018; Hua et al., 2020; Lin et al., 2020). Although the sediment load has declined recently, the surface sediment concentration maintains at a level of 0.2-0.5 kg/m$^3$ while near-bed concentration increases up to 80 kg/m$^3$ (Xu, 2009; Liu et al., 2011; Jiang et al., 2013; Wan and Zhao, 2017; Ge et al., 2018; Lin et al., 2021). Such high sediment concentrations influence water density and stratification (L. Li et al., 2018; Lin et al., 2021; Zhu et al., 2021b) and cause drag reduction and tidal amplification (Winterwerp et al., 2009; Lin et al., 2021; Zhu et al., 2021a), altering the sediment transport mechanisms (e.g., circulation and tidal pumping). Particularly after the DWP, sediment-induced stratification becomes important and comparable to that induced by salinity due to the sediment trapping and increasing sediment concentrations in the estuary (Song et al., 2013; L. Li et al., 2018; Li et al., 2019; Lin et al., 2021). Nevertheless, a comprehensive picture of how estuarine hydrodynamics and sediment dynamics change in response to the DWP and declined fluvial sediment supply was not available. A better understanding of such a picture benefits the prediction of the ETM evolution and estuary management.

## 1.4. Aim and objectives

The motivation for studying hydrodynamics and sediment dynamics in estuaries is two-fold. Firstly, these dynamics are crucial processes affecting the natural and economic values of estuaries. Secondly, with anthropogenic-driven environmental changes globally, hydrodynamics and sediment dynamics are changing in many estuaries, leading to potential changes in these values. The critical issue in managing estuaries is maintaining and protecting their ecological functioning while producing economic benefits (Wolanski et al., 2019). The Changjiang Estuary is an example, with declined fluvial sediment supply and large-scale human interventions (e.g., the Deep Waterway Project).

This thesis aims to identify and quantify the sediment transport processes in the Changjiang Estuary to predict the development of the system with the influence of human interventions. Several approaches can be taken to reach this aim, including field measurements and numerical modelling (Zhou et al., 2021; Zhu et al., 2021b). In this thesis, we focus on the analysis of field data. As a general approach, this requires (i) improvement of the tools to analyse the data, (ii) analysis of the "natural" system, and (iii) analysis of the impact of human interventions.

Accurate sediment concentrations and flow velocities are the basis for this study. The methods for measuring sediment concentrations include water sampling and (optical and acoustic) sensors. Water sampling is a traditional, reliable and widely used method to measure sediment concentrations. However, this classic method is labour-intensive, and its temporal and spatial resolutions are generally limited. Moreover, accurate near-bed sampling (<0.5 m) is challenging. This region, however, is of high importance for sediment dynamics due to the high sediment concentrations. Therefore, to obtain high-resolution sediment concentration profiles, especially in the bottom boundary layer, more advanced technologies and sensors (optical or acoustic) have been developed in the last decades.

Nevertheless, the accurate measurement of sediment concentrations in highly turbid environments is still a problem due to the optical or acoustic signal saturation and attenuation (Lin et al., 2020). The saturation returns a limited measurement range (<10 g/L), while the attenuation raises an ambiguity problem that a low optical or acoustic output could mean a low or a high sediment concentration. Thereby, a reliable, accurate and efficient method is required to resolve these problems to access accurate measurements of high sediment concentrations.

Three objectives are defined:

1) Tool development: develop a method for measuring high sediment concentrations;
2) Mechanism analysis: identify and quantify the mechanisms responsible for the transport of fine sediment;
3) Human interferences: determine how the engineering works modified the transport processes.

## 1.5. Thesis organisation

This thesis consists of five chapters (Figure 1-6), and the organisation is as follows:
**Chapter 2** solves the ambiguity problem of optic and acoustic sensors in sediment concentration measurements and obtains reliable suspended sediment concentrations using an integrated optic and acoustic approach.
**Chapter 3** explores the changes in suspended sediment concentration profiles in response to the DWP (i.e., deepening and narrowing) and declined fluvial sediment supply in the North Passage of the Changjiang Estuary. This chapter also gives insights into how the hyper-turbid state develops in the water column.
**Chapter 4** reveals the mechanisms underlying the enhanced estuarine circulation and quantifies the changes in density stratification and sediment transport due to

the DWP. The roles of estuarine circulation and tidal pumping in the ETM evolution are clarified in this chapter.
Finally, **Chapter 5** summarises the overall conclusions of the thesis and provides an outlook on applications and future research.



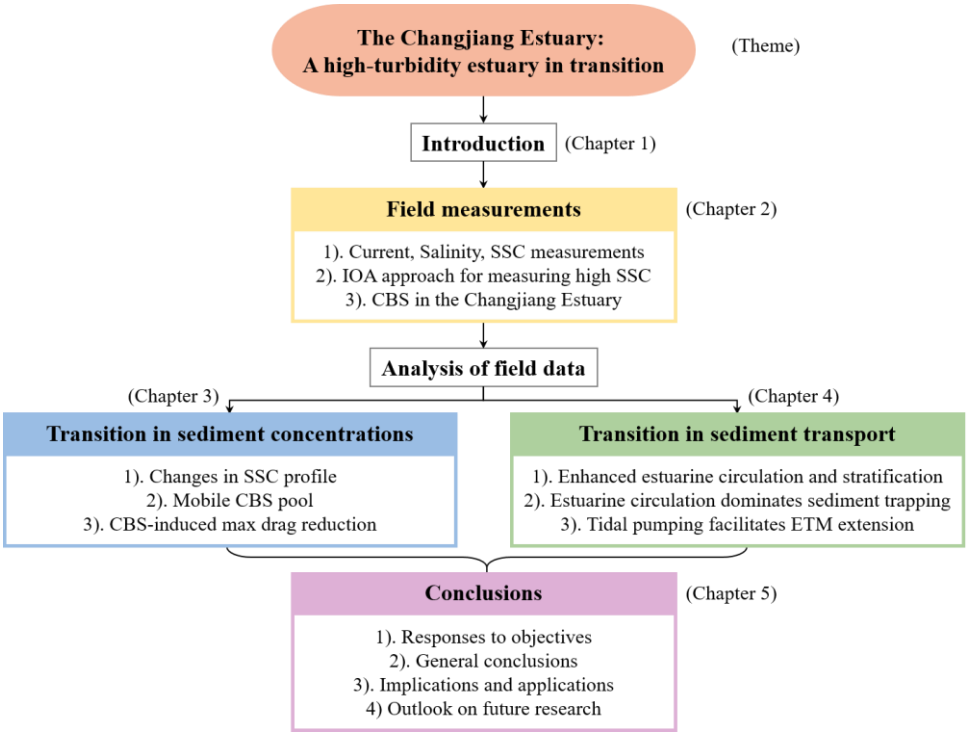


*Figure 1-6: An overview of the content and structure of this thesis. SSC: suspended sediment concentration. IOA approach: integrated optical and acoustic approach. CBS: concentrated benthic suspensions.*

# **2.** A Novel Approach for Measuring High Suspended Sediment Concentrations†


† Parts of this chapter have been published in: Lin, J., He, Q., Guo, L., van Prooijen, B.C., Wang, Z.B., 2020. An integrated optic and acoustic (IOA) approach for measuring suspended sediment concentration in highly turbid environments. Marine Geology 421, 106062. https://doi.org/10.1016/j.margeo.2019.106062

*Accurate measurement of suspended sediment concentration (SSC) in highly turbid environments has been a problem due to optical or acoustic signal saturation and attenuation. The saturation returns a limited measurement range, and the attenuation raises an ambiguity problem: a low optical or acoustic output could mean a low or a high SSC. In this chapter, an integrated optic and acoustic (IOA) approach is proposed (i) to overcome the ambiguity problem, (ii) to increase the measurement range to high SSC values, and (iii) to obtain high-resolution SSC profiles. The IOA approach is a combination of the Argus Suspension Meter (ASM), the Optical Backscatter Sensor (OBS) and the Acoustic Doppler Velocimeter (ADV). The ASM-derived SSC is preferred in this approach because of its lowest relative error, followed by OBS and ADV. The ASM can produce high-resolution (1 cm interval) SSC profiles when it is not saturated (usually SSC <9 g/L). When the ASM is saturated, the SSC is recovered by the OBS. Since the ambiguity problem is solved, the OBS and ADV measurement ranges can be extended to 300 g/L. However, the best way to use an ADV is to have a rough estimation and assist in the OBS conversion because its estimates contain significant uncertainty. To further mitigate the impact of sediment particle size on SSC retrieval, we suggest using in-situ sediment samples for sensor calibration. The IOA approach was tested in the Changjiang Estuary, a highly turbid system. The comparison between the estimates from the IOA approach and water sampling demonstrates the reliability of the IOA approach, which gives estimates with relative errors of 17–34%. The observed SSCs were up to 63 g/L. The field data show that high SSCs were confined in the benthic layer (within 2 m above the bed) in the wet season, whereas the suspension was well mixed throughout the water column in the dry season.*

# 2.1. Introduction

Suspended sediment concentration (SSC) is a critical parameter for understanding the transport of sediment and contaminants (Manning et al., 2010; Liang et al., 2013; Huettel et al., 2014; Burchard et al., 2018). In addition, SSC limits the light availability and affects the primary production in lakes, rivers, estuaries and coastal waters (Yoshiyama and Sharp, 2006; van Kessel et al., 2011). Note that SSC can vary orders of magnitude over a small distance or a short period (Burchard et al., 2018; Ge et al., 2018). Accurate SSC measurements with a high spatial and temporal resolution, therefore, have significant implications for the management of ecology, biogeochemistry, and geomorphology. However, measuring high-resolution SSC in a simple, robust and efficient way is not straightforward, particularly in highly turbid environments.



*Table 2-1: Measurement techniques of suspended sediment concentration*

| Technology | Operating principle | Advantages | Disadvantages |
|---|---|---|---|
| Water sampling | Water-sediment sample is taken and later analysed | Reliable<br>Informative (SSC, salinity, PSD*) | Flow-intrusive,<br>Labour-intensive<br>Low frequency<br>Poor spatial resolution<br>Near-bed data missing |
| Optical | Light backscatter through a water-sediment sample is measured and translated to SSC with calibration | High accuracy,<br>Good spatial resolution<br>High frequency | Flow-intrusive<br>Particle-size dependent<br>Limited range<br>Uncertainties in high SSC |
| Acoustic | Echo strength from sample determines SSC based on calibration | Nonintrusive,<br>Good spatial resolution,<br>High frequency synchronous SSC and velocity | Low accuracy<br>Limited range<br>Uncertainties in high SSC |

* *SSC and PSD denote suspended sediment concentration and particle size distribution, respectively.*

Water sampling (e.g., suction/pumping) is a traditional, reliable and widely used method to measure SSC. The SSC from the water sample is generally regarded as a reference for sensor calibration (Kineke and Sternberg, 1992; Fugate and Friedrichs, 2002; Gray and Gartner, 2010; Wang et al., 2013; Baeye and Fettweis, 2015; Druine et al., 2018). The SSC given by this method contains a relative error of ~20% from sampling and later analysis (McHenry et al., 1967). Point-integrating samplers can obtain SSC profiles of nearly the entire water column. However, water sampling is labour-intensive, which implies that temporal and spatial resolutions are generally limited. Near-bed sampling (< 0.5 m) is challenging, although this region is highly interested in understanding sediment exchange processes.

To obtain a high-resolution SSC profile, especially in the bottom boundary layer, more advanced technologies and sensors (optical or acoustic) have been developed in the last decades (Table 2-1; see also Wren et al., 2000; Thorne and Hanes, 2002; Rai and Kumar, 2015; Rymszewicz et al., 2017).

Optical sensors measure SSC by the strength of back- or side-scattered light, e.g., Optical Backscatter Sensor (OBS) (Campbell Scientific, 2018), Argus Suspension Meter (ASM) (Argus, 2014), YSI (YSI Incorporated, 2012), Fiber Optic In-stream Transmissometer (FIT) (Campbell et al., 2005) and HHU-LIOS (Shao and Maa, 2017). They can measure SSC at a high frequency (1-25 Hz) (Campbell Scientific, 2018), but their measurements are generally restricted to a single point in a fixed deployment. Stacked optical sensors (e.g., ASM) were later developed, providing SSC profiles with a vertical resolution of 1 cm (Vijverberg et al., 2011; Ge et al., 2018). Although multiple or moving optical sensors increase the spatial resolution of SSC measurements, they still require an intrusion in the flow, which may disturb the flow and the distribution of suspended sediment. Particle-size dependency is another drawback of the optical sensor. The reading of the same sensor may increase by ten times for the same SSC with a smaller particle size (Ludwig and Hanes, 1990; Campbell Scientific, 2018). Therefore, continuous calibration against in-situ SSC from water sampling is needed (Maa et al., 1992; Nauw et al., 2014). Additionally, the optical output has an upper limit because of the signal saturation (e.g., ASM) or attenuation (e.g., OBS). Within a low SSC (< 9 g/L), the optical output increases nearly linearly with increasing SSC (Figure 2-1, see also Downing, 2006; Shao and Maa, 2017). Beyond the threshold, however, the ASM output maintains its maximum, and the OBS output decreases with increasing SSC (Figure 2-1). As a result, the ASM has a limited measurement range, and the OBS has an ambiguity problem in conversion. A low OBS output could mean a low or high SSC, challenging to differentiate. Recently, a laser infrared optical sensor was developed by Hohai University (Nanjing, China, HHU-LIOS) with a measurement range of 0-30 g/L (Shao and Maa, 2017). This extension of the SSC range is a significant improvement, but

it is still insufficient for highly turbid environments, e.g., the Changjiang (Yangtze) Estuary (Wan et al., 2014) and the Ems Estuary (Winterwerp et al., 2017). Therefore, a combination of HHU-LIOS and OBS was suggested by Shao and Maa (2017). However, their method only gives SSC at a single point but not a profile.

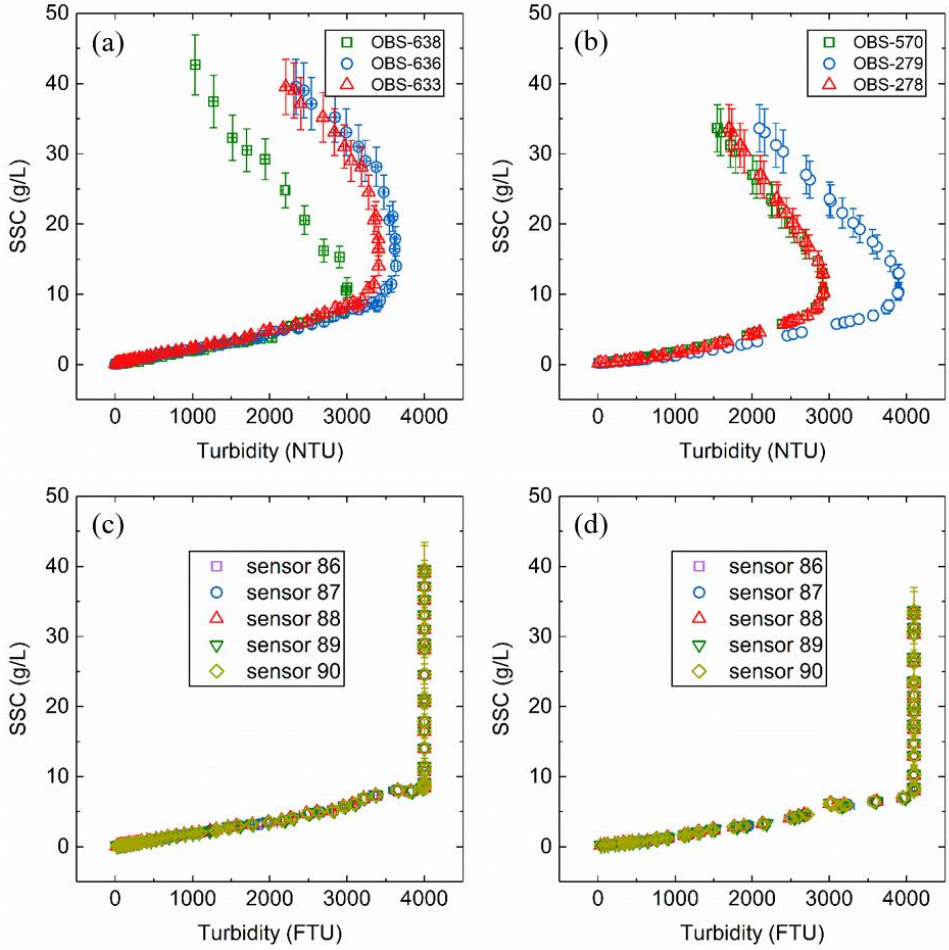


*Figure 2-1: Calibrations of OBS (turbidity in NTU) (a, b) and ASM (turbidity in FTU) (c, d) against SSC (in g/L) with bottom sediment collected in July 2014 (left panel) and January 2016 (right panel), respectively. Regression results are shown in Table 2-2.*

Acoustic sensors are utilised for measuring SSC profiles non-intrusively, e.g., Acoustic Doppler Profiler (ADP) (Thorne and Hanes, 2002; Ha et al., 2011; Baeye and Fettweis, 2015) and Acoustic Doppler Velocimeter (ADV) (Ha et al., 2009; Salehi and Strom, 2011; Shao and Maa, 2017). In addition to SSC, acoustic sensors also

measure flow velocity synchronously. ADP (Moura et al., 2011; Sahin et al., 2013; Fettweis and Baeye, 2015) and ADCP (Guerrero et al., 2011; Anastasiou et al., 2015; Baeye and Fettweis, 2015), for example, concurrently obtain velocity and SSC profiles over several meters. High-frequency acoustic signals (~10 Hz) can be used to estimate turbulent water and sediment flux, e.g., ADV (Fugate and Friedrichs, 2002; Scheu et al., 2015; Yang et al., 2016). Optical sensors cannot obtain synchronised high-frequency velocity measurements at the same location, although they provide high-frequency SSC estimates (C. Guo et al., 2018). Moreover, converting acoustic outputs into SSC has an ambiguity problem and contains significant uncertainties. First, the acoustic output increases exponentially with increasing and low SSC (<1-2 g/L), so a minor misalignment in acoustic outputs may introduce a significant error in its estimates. For instance, 1 dB misalignment in ADV output can cause an error of ~1 g/L in the estimated SSC (Merckelbach and Ridderinkhof, 2006; Shao and Maa, 2017). Second, similar to optical sensors, the acoustic signal attenuates quickly in high SSC (>1-10 g/L) (Figure 2-2, see also Ha et al., 2009; Shao and Maa, 2017), which causes ambiguity in SSC retrieval.

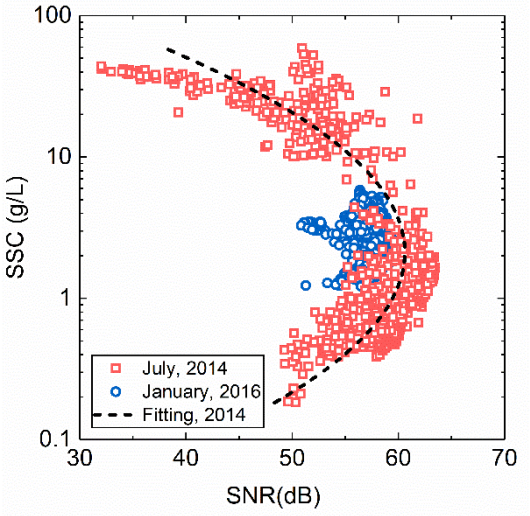


*Figure 2-2: Calibration of ADV (SNR in dB) against the SSC (in g/L) given by ASM and OBS. Regression results are shown in Table 2-2.*

This chapter aims to solve the ambiguity problem that a low OBS and ADV reading could mean a low or a high SSC and access a broader measurement range. We propose an integrated optical and acoustic (IOA) approach to identify the true SSC and obtain high-resolution SSC profiles by combining OBS, ASM and ADV. This chapter is organised in the following way. Section 2.2 describes the calibration of sensors. Upon careful calibrations, we propose algorithms for each sensor to convert

their outputs into SSC in Section 2.3. These algorithms are compared with the SSCs from the water samples obtained in the Changjiang Estuary. An optimised algorithm is then suggested in Section 2.4. The accuracy and advantages of the proposed IOA approach are discussed in Section 2.5. Section 2.5 also discusses the observed seasonal SSC profiles and intra-tidal bottom SSC variation in the Changjiang Estuary. It is concluded in Section 2.6 that the IOA approach is reliable, providing a wide measurement range of up to 300 g/L and high-resolution SSC profiles when the ASM is not saturated. The application of the IOA approach is beneficial for quantifying sediment transport in the bottom boundary layer or highly turbid environments.



## 2.2. Sensor calibrations

The OBS (turbidity in NTU) and the ASM (turbidity in FTU) were calibrated in a cylindrical container (0.4 m in diameter and 0.5 m in height) with continuous and steady stirring at the bottom. First, the container was filled with water collected from the Changjiang Estuary. Then, we gradually poured the slurry (an amalgam of bottom sediment collected every 2 hours within a campaign) into the container to determine different SSC levels. The OBS and one of the ASM sensors ($88^{th}$ sensor) were mounted 15 cm above the bottom with an outlet at the same height for water sampling. We took a water sample at each SSC level after the turbidity readings stabilised for 30 seconds. Subsequently, the water sample was filtered through a pre-weighed filter (0.45 μm), and the filter was dried at 40 °C for 48 h to determine the SSC. The averaged turbidity during the sampling was then calibrated against the SSC of water samples (Figure 2-1).

The calibration of the ADV (signal-to-noise ratio, SNR in dB) was carried out with the in-situ SSC derived by the ASM and the OBS. The sampling rate of the ADV was 8 Hz, and the burst interval was 10 min. In each burst, the ADV measured velocities continuously for 90 seconds. The SNRs from three receiving transducers were averaged to obtain the representative mean value. The burst-averaged SNR was then calibrated against the in-situ SSC (Figure 2-2).

The calibration results indicate that the response of each sensor (i.e., OBS, ASM and ADV) to increasing SSC is different. The ASM turbidity ($T_{ASM}$) increases linearly with SSC below ~9 g/L (Figure 2-1c and d). Beyond this limit, however, $T_{ASM}$ maintains at the maximum (i.e., saturated). All ASM sensors behave the same (Figure 2-1c and d).

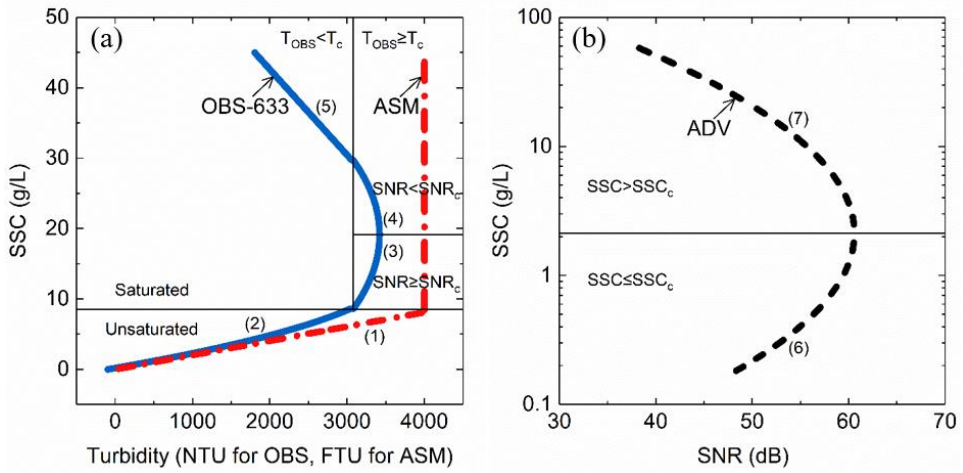


*Figure 2-3: Examples of calibration curves (ASM, OBS-633 and ADV employed in July 2014) illustrate the conversion protocols of the IOA approach. $T_C$ denotes the critical OBS turbidity (reading, i.e., $T_C$ =3050 NTU, corresponding to SSC ~ 9 g/L) once ASM saturates (with a reading around 4000 FTU), and $SNR_C$ (~ 61 dB) indicates the critical SNR corresponding to the max OBS turbidity (reading, i.e., 3400 NTU, corresponding to SSC = 20 g/L when using OBS). $SSC_C$ indicates the critical SSC (i.e., $SSC_C$ = 2 g/L) where the ADV returns the max SNR. The numbers in parenthesis, e.g., (4), are the shorthand of Calibration Relation (CR) shown in Table 2-2 and Figure 2-4.*

The OBS turbidity ($T_{OBS}$) shows three responses (Figure 2-1a and b). At low SSCs, when $T_{ASM}$ is unsaturated, $T_{OBS}$ increase almost linearly. A critical OBS turbidity ($T_C$) can be determined once $T_{ASM}$ saturates (Figure 2-3a). Within a range of moderate SSC, when $T_{ASM}$ saturates and $T_{OBS} \geq T_C$, $T_{OBS}$ remains roughly the same and begins to decrease after reaching the maximum (max $T_{OBS}$). A parabolic function fits in this range. To relate the turbidity to SSC more directly, we divide the curve into two sections (Figure 2-3a, curves 3 and 4). $T_{OBS}$ decreases linearly in high SSCs when $T_{ASM}$ saturates and $T_{OBS} < T_C$. Four representative curves are identified to match the transition from one range to the next as continuous as possible (Figure 2-3a). Table 2-2 summarises the equations of each calibration curve and their correlation coefficients.

*Table 2-2.1: C-R relationship for calibrated sensors. C denotes suspended sediment concentration in g/L, and R represents the readings of OBS (turbidity in NTU), ASM (turbidity in FTU) and ADV (SNR in dB).*

| Time | Instrument | Conditions | C-R relationship | Samples | $R^2$ |
|---|---|---|---|---|---|
| 201407 | ASM | Unsaturated | $C=2.0\times10^{-3}R$ | 42 | 0.99 |
| | | Unsaturated | $C=3.5\times10^{-7}R^2+1.6\times10^{-3}R+0.2$ | 42 | 0.99 |
| | OBS-633 | Saturated, $T_{obs}\geq T_c$, $SNR\geq SNR_c$ | $C=19.2-\frac{\sqrt{41734.0-12.2R}}{6.1}$ | 13 | 0.92 |
| | | Saturated, $T_{obs}\geq T_c$, $SNR<SNR_c$ | $C=19.2+\frac{\sqrt{41734.0-12.2R}}{6.1}$ | | |
| | | Saturated, $T_{obs}<T_c$ | $C=-1.2\times10^{-2}R+66.0$ | 7 | 0.97 |
| | OBS-636 | Unsaturated | $C=3.0\times10^{-7}R^2+1.5\times10^{-3}R+0.2$ | 42 | 0.99 |
| | | Saturated, $T_{obs}\geq T_c$, $SNR\geq SNR_c$ | $C=18.7-\frac{\sqrt{42531.8-11.7R}}{5.9}$ | 13 | 0.93 |
| | | Saturated, $T_{obs}\geq T_c$, $SNR<SNR_c$ | $C=18.7+\frac{\sqrt{42531.8-11.7R}}{5.9}$ | | |
| | | Saturated, $T_{obs}<T_c$ | $C=-1.1\times10^{-2}R+65.9$ | 7 | 0.97 |
| | OBS-638 | Unsaturated | $C=3.9\times10^{-7}R^2+1.4\times10^{-3}R+0.1$ | 34 | 0.99 |
| | | Saturated, $T_{obs}\geq T_c$, $SNR\geq SNR_c$ | $C=10.2-\frac{\sqrt{104937.2-35.0R}}{17.5}$ | 4 | 0.98 |
| | | Saturated, $T_{obs}\geq T_c$, $SNR<SNR_c$ | $C=10.2+\frac{\sqrt{104937.2-35.0R}}{17.5}$ | | |
| | | Saturated, $T_{obs}<T_c$ | $C=-1.6\times10^{-2}R+59.2$ | 10 | 0.97 |
| | ADV | $SSC\leq SSC_c$ | $\lg C=0.3-\frac{\sqrt{2623.2-43.3R}}{21.7}$ | 685 | 0.70 |
| | | $SSC>SSC_c$ | $\lg C=0.3+\frac{\sqrt{2623.2-43.3R}}{21.7}$ | | |

*Table 2-2.2: C-R relationship for calibrated sensors. C denotes suspended sediment concentration in g/L, and R represents the readings of OBS (turbidity in NTU), ASM (turbidity in FTU) and ADV (SNR in dB).*

| Time | Instrument | Conditions | C-R relationship | Samples | $R^2$ |
|---|---|---|---|---|---|
| 201601 | ASM | Unsaturated | $C=1.8\times10^{-3}R$ | 43 | 0.99 |
| | OBS-278 | Unsaturated | $C=6.9\times10^{-7}R^2+6.5\times10^{-4}R+0.2$ | 43 | 0.99 |
| | | Saturated, $T_{obs}\geq T_c$, $SNR\geq SNR_c$ | $C=11.5-\frac{\sqrt{80551.5-27.5R}}{13.7}$ | 9 | 0.99 |
| | | Saturated, $T_{obs}\geq T_c$, $SNR<SNR_c$ | $C=11.5+\frac{\sqrt{80551.5-27.5R}}{13.7}$ | | |
| | | Saturated, $T_{obs}<T_c$ | $C=-1.6\times10^{-2}R+61.1$ | 14 | 0.99 |
| | OBS-279 | Unsaturated | $C=3.2\times10^{-7}R^2+8.2\times10^{-4}R+0.2$ | 43 | 0.99 |
| | | Saturated, $T_{obs}\geq T_c$, $SNR\geq SNR_c$ | $C=11.6-\frac{\sqrt{176062.0-45.0R}}{22.5}$ | 9 | 0.99 |
| | | Saturated, $T_{obs}\geq T_c$, $SNR<SNR_c$ | $C=11.6+\frac{\sqrt{176062.0-45.0R}}{22.5}$ | | |
| | | Saturated, $T_{obs}<T_c$ | $C=-1.1\times10^{-2}R+57.0$ | 14 | 0.99 |
| | OBS-570 | Unsaturated | $C=6.0\times10^{-7}R^2+9.1\times10^{-4}R+0.2$ | 43 | 0.99 |
| | | Saturated, $T_{obs}\geq T_c$, $SNR\geq SNR_c$ | $C=11.4-\frac{\sqrt{81988.4-28.0R}}{14.0}$ | 9 | 0.99 |
| | | Saturated, $T_{obs}\geq T_c$, $SNR<SNR_c$ | $C=11.4+\frac{\sqrt{81988.4-28.0R}}{14.0}$ | | |
| | | Saturated, $T_{obs}<T_c$ | $C=-1.5\times10^{-2}R+56.1$ | 14 | 0.99 |

The SNR from ADV also has three responses to different SSC levels (Figure 2-3b), i.e., increasing, constant and decreasing regions. For convenience, a parabolic fitting with the SSC on a logarithmic scale is applied in this study, which returns a high coefficient of determination (Table 2-2). The max SNR occurs in a critical SSC (~2 g/L) (Figure 2-2, see also Ha et al., 2009; Shao and Maa, 2017). The SNR decreases monotonically with SSC when the ASM is saturated.

## 2.3. Conversion algorithms



Based on the different responses of ASM, OBS and ADV, several algorithms are developed to convert their outputs into SSC (Figure 2-4). To explain the conversion processes, we take the OBS-633, ASM and ADV as examples (Figure 2-3).

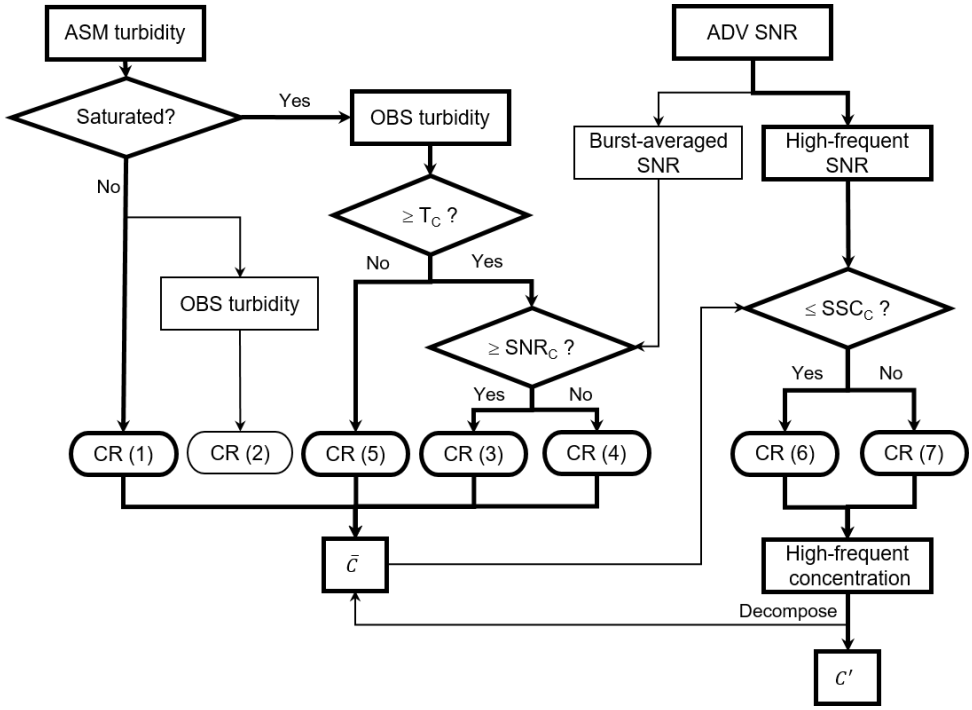


*Figure 2-4: Algorithms for ASM, OBS and ADV to estimate reliable SSC. CR denotes the calibration relationship between suspended sediment concentrations and readings of sensors (i.e., turbidity and SNR) given in Table 2-2. Highlighted flowcharts show the optimal protocol according to the performance of each sensor.*

The conversion of ASM outputs is relatively simple. Firstly, it needs to identify whether the ASM is saturated or not. The ASM provides estimates only when it is

not saturated. Once the ASM saturates, no valid estimate is given. Fortunately, the OBS or the ADV can recover the missing high SSC.

The accurate conversion of OBS outputs requires a combined usage of the ASM and the ADV. The critical OBS turbidity ($T_C$) and SNR ($SNR_C$) need to be determined before the conversion (Figure 2-3). A second-order polynomial is applied when $T_{ASM}$ is not saturated (Figure 2-3a, curve 2). For saturated $T_{ASM}$ and $T_{OBS} < T_C$, the estimate is given by a negative and linear relationship (Figure 2-3a, curve 5). For saturated $T_{ASM}$ and $T_{OBS} \geq T_C$, the estimate is taken as the smaller solution to the parabolic equation when $SNR \geq SNR_C$ (Figure 2-3a, curve 3) and the larger solution when $SNR < SNR_C$ (Figure 2-3a, curve 4).



The SSCs derived from the ASM and the OBS serve the conversion of the ADV. Upon the determination of critical SSC ($SSC_C$), the estimate from the ADV is taken as the smaller solution to the parabolic equation when $SSC \leq SSC_C$, (Figure 2-3b, curve 6) and the larger solution when $SSC > SSC_C$ (Figure 2-3b, curve 7).

## 2.4. Application and evaluation

To test and evaluate the proposed IOA approach and algorithms, we conducted field campaigns in the Changjiang Estuary in July 2014 (wet season) and January 2016 (dry season). The mean river discharges were 44,350 $m^3/s$ in the wet season and 21,200 $m^3/s$ in the dry season. An optimised algorithm is suggested upon the calibrations between the SSC given by the optical and acoustic sensors and water sampling. Furthermore, the advantages of the IOA approach are highlighted by comparing SSC profiles with and without such an algorithm.

### 2.4.1. Field campaigns in the Changjiang Estuary

The Changjiang (Yangtze) Estuary is an excellent example of highly turbid systems, particularly in its estuarine turbidity maximum (ETM), where the SSC is >10 g/L near the bed (He et al., 2001; Shi et al., 2006; Wan et al., 2014). Two campaigns were conducted in the North Passage (Figure 2-5). Both tripod- and ship-borne systems with multiple sensors were employed for each campaign. Table 2-3 summarises the operated instruments and their sampling schemes.

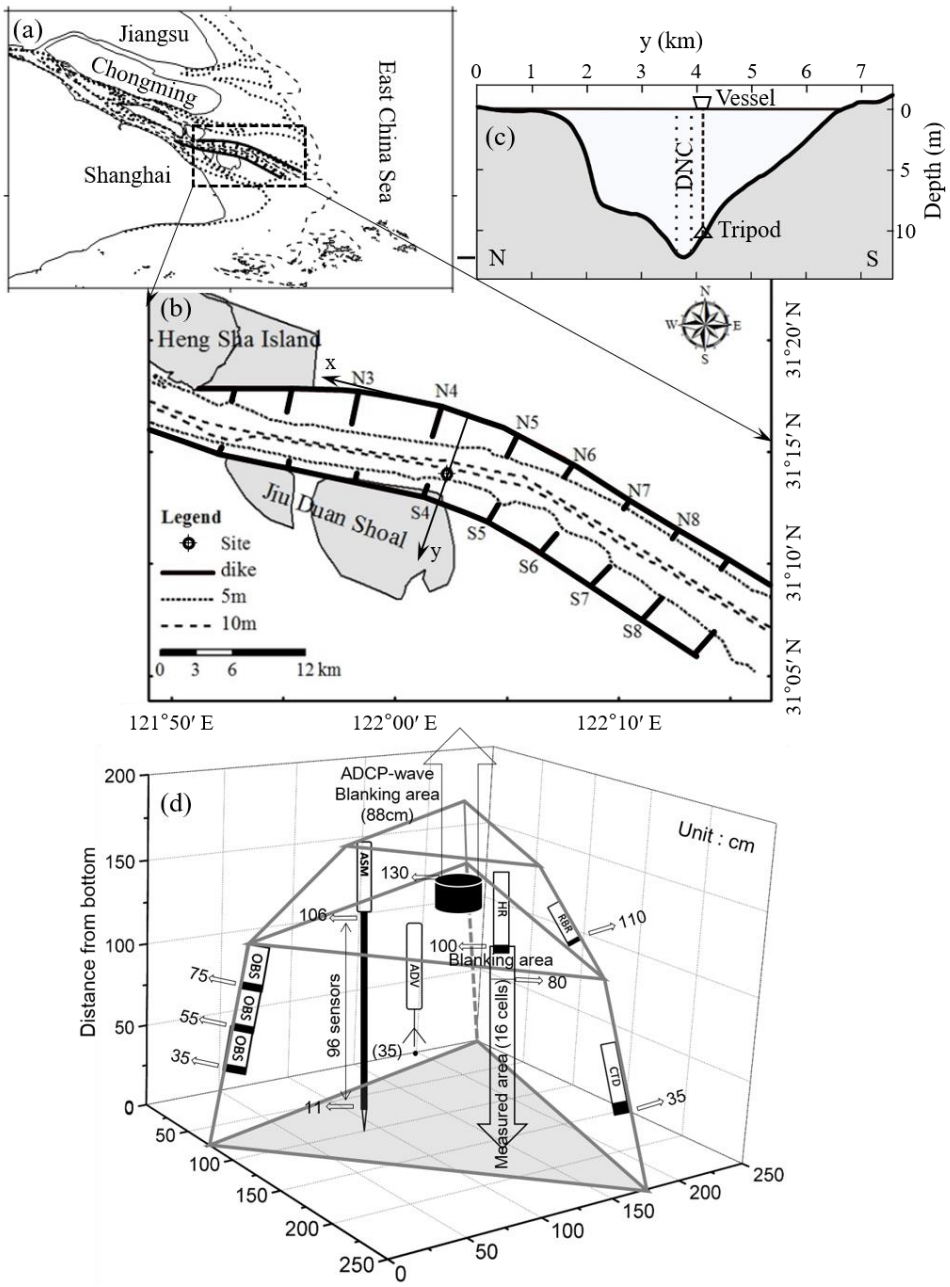


*Figure 2-5: The Changjiang Estuary (a), the Deepwater Navigational Channel (DNC) at the North Passage (b), the positions of the DNC and the moored tripod and shipboard observation systems in an estuarine cross-section (c), and the schematic of bottom-mounted tripod system with multiple sensors (d). The numbers in (d) represent the distance of the sensor above the seabed.*

*Table 2-3: Shipboard and tripod instruments and their sampling schemes*

| Carrier | Instruments | Height above bed (m) | Sampling interval (min) | Sampling duration (sec) | Sampling frequency (Hz) | Survey parameters | Profile resolution (m) |
|---|---|---|---|---|---|---|---|
| Vessel | ADCP | > 1.5 | continuously | continuously | 0.1 | upper velocity | 0.5 |
| | OBS | > 1.0 | 60 | 30 | 1 | SSC, salinity, temperature | 0.1 |
| | LISST | * | 60 | 30 | 1 | FSD | - |
| | Water sampler | * | 60 | 30 | - | SSC, salinity, PPSD | - |
| Tripod | ACP | < 0.8 | 5 | 60 | 1 | near-bed velocity | 0.05 |
| | ADCP-wave | > 2.0 | 5 | 60 | 1 | upper velocity, wave | 0.5 |
| | RBR | 1.1 | 5 | 60 | 1 | wave | - |
| | ADV | 0.35 | 10 | 90 | 8 | near-bed velocity, SSC | - |
| | ASM | 0.11-1.06 | 5 | 60 | 1 | SSC | 0.01 |
| | OBS | 0.35, 0.55, 1.06 | 5 | 60 | 1 | SSC, salinity, temperature | - |

** data or samples collected at six relative depth layers, i.e., 0.05H (near surface), 0.2H, 0.4H, 0.6H, 0.8H, and 0.95H (near-bed), where H is the total water depth. FSD and PPSD denote the flocculate and primary particle size distribution, respectively.*

A sketch of the bottom-mounted tripod system is given in Figure 2-5d. An ASM measured turbidity profiles from 0.11 to 1.06 m above the bed (mab here-after). OBSs simultaneously measured turbidity, salinity, and temperature at 0.35, 0.55 and 1.06 mab. A downward-looking ADV recorded high-frequency 3D velocities and SNR at 0.35 mab. The sensors in the ADV were also used to monitor the heading, pitch and roll states of the tripod.

Ship-borne observations included turbidity, salinity and velocity profiles, and water sampling. The OBS hourly measured turbidity and salinity profiles by moving from the water surface to the bed (~0.5 mab). The OBS stayed for 30 seconds at each of six depth layers, i.e., 0.05 (near-surface), 0.2, 0.4, 0.6, 0.8, and 0.95 (near-bed) of the water depth. A water sample of 1.2 L was concurrently collected at each layer. These water samples were used for laboratory analysis of SSC, salinity and primary particle size distribution. A Coulter Counter analyser measured the particle size after removing organic material and destroying flocs by sonification. The LISST-100C hourly recorded the in-situ floc size distribution and volume concentration at each layer. Bottom sediment was collected every 2 hours for the calibration of tripod-borne sensors.



In order to avoid interference between tripod- and ship-borne sensors, the tripod was deployed about 200 m upstream of the vessel. This distance is negligible compared with the distance between the two groins (~5 km). However, it is not allowed to deploy an instrument tripod or mooring vessel in the Deepwater Navigational Channel (DNC) for safety reasons. Therefore, tripod- and ship-borne measurements were conducted on the south flank of the channel, ~200 m away from the DNC (Figure 2-5c). Due to the significant differences in cross-channel hydrodynamics and topography (Song et al., 2013; Wan et al., 2014; Ge et al., 2015), the tripod and the vessel should keep the same distance from the DNC. Then we can assume that the tripod- and ship-borne measurements represent the same site, although they are actually in different locations.

The temporal and spatial variations of water temperature were minor within a campaign, e.g., 24.7-27.0 °C in July 2014 and 3.5-6.1 °C in January 2016. Hence the impact of temperature on the sensors was negligible. However, the water temperature difference between the two campaigns was significant, so we calibrated the sensors at a temperature similar to the on-site water temperature.

### 2.4.2. SSC from in-situ water samples

To evaluate the performance of each sensor, we take the SSC from in-situ water sampling as the reference. The water depth (H) ranged from 9 to 13 m (Figures 2-

6a and 7a), so near-bed SSC (at 0.95H) represented the SSC at 0.45-0.65 mab, which can be used for the evaluation of tripod sensors. The SSC from water samples can only be verified by comparing samples taken close to each other simultaneously. Unfortunately, such samples were not available in our study. Note that the SSC may be incorrect due to sampling and analysis errors. However, we do not have direct indications.

The SSC ranged 0.4-39.8 g/L in July 2014 (Figure 2-6d) and 1.4-5.1 g/L in January 2016 (Figure 2-7d). High SSC values and a wide SSC range in July 2014 are preferred to evaluate the performance of the IOA approach. Concerning intra-tidal variation (Figures 2-6d and 7d), the SSC increased after low water slack (LWS). The SSC peaked around the max flood and decreased slightly after that. After high water slack (HWS), the SSC increased rapidly again, reaching another peak during the early ebb. Subsequently, the SSC dropped and reached the minimum at LWS. A similar intra-tidal variation pattern was observed in January 2016, except for higher SSC in the wet season and postponed peaks during the late flood of the dry season.

The SSC from the water sample was higher than 10 g/L at 15:00-17:00 on July 14, 2014 (Figure 2-6d). During this period, the ASM was saturated, and both OBS and ADV outputs decreased significantly. It suggests that observed high SSCs were consistent, and they caused optical and acoustic attenuation in the field. The SSC, however, decreased suddenly to ~1 g/L at 2:00-5:00 on July 15, when the ASM was saturated. Meanwhile, the bottom turbidity was >3000 NTU, supported by the tripod- and ship-borne OBSs, indicating an SSC > 10 g/L. There are chances that the SSC from water sampling is underestimated during this period. This underestimation could result from the sampling not being close enough to the bed and/or laboratory analysis errors. Therefore, the underestimated SSC (only one sample) was excluded from the evaluation.

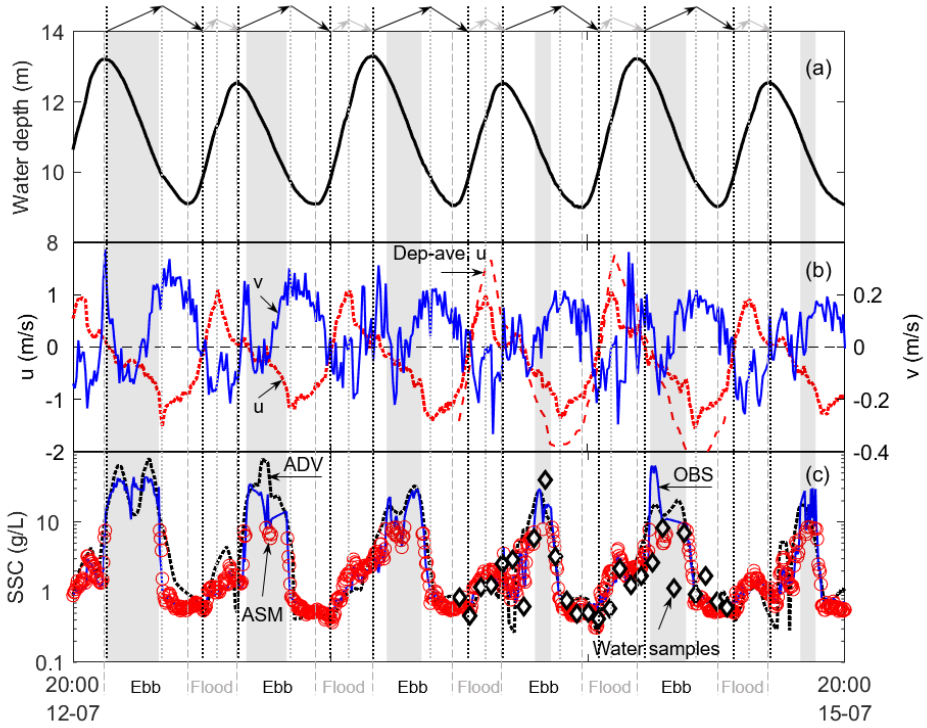


*Figure 2-6: Time series of July (wet season) 2014 in the North Passage, Changjiang Estuary. (a) water depth measured by the CTD, (b) along- (u, red dot) and cross- (v, blue solid) channel velocity measured by the ADV at 0.35 meter above bed (mab) and depth-averaged u (red dash); (c) SSCs from the filtration of water samples collected at the bottom layer (i.e., 0.95H, diamond), and ASM (circle), OBS (solid line) and ADV (dot line) at 0.35 mab. Note that the estimates given by the ASM are missing when it is saturated. Positive u indicates the flood direction, and positive v represents the cross-channel velocity from the north to the south. Since the survey site is located on the channel's south flank, the positive v indicates the channel-to-shoal flow. The period for flood (grey) and ebb (black) are marked at the bottom. The tidal current acceleration phases are marked on top by arrows with a positive slope, and arrows with a negative slope mark the deceleration phases. The shadow area indicates the periods when SSC > 10 g/L. The tidal current phase between near-bed and depth-averaged velocity is roughly the same.*

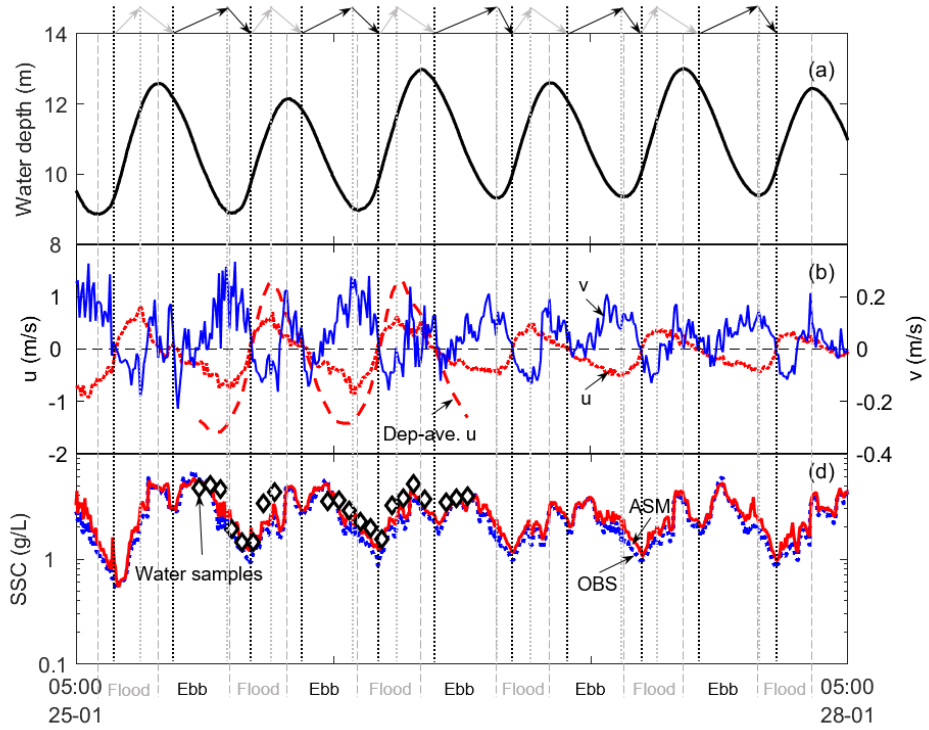


*Figure 2-7: Time series of January (dry season) 2016 in the North Passage, Changjiang Estuary. (a) water depth measured by the CTD, (b) along- (u, red dot) and cross- (v, blue solid) channel velocity measured by the ADV at 0.35 meter above bed (mab) and depth-averaged u (red dash); (c) SSCs from the filtration of water samples collected at the bottom layer (i.e., 0.95H, diamond), and ASM (solid line) and OBS (dot line) at 0.35 mab. Positive u indicates the flood direction, and positive v represents the cross-channel velocity from the north to the south. Since the survey site is located on the channel's south flank, the positive v indicates the channel-to-shoal flow. The period for flood (grey) and ebb (black) are marked at the bottom. The tidal current acceleration phases are marked on top by arrows with a positive slope, and arrows with a negative slope mark the deceleration phases. The tidal current phase between near-bed and depth-averaged velocity is roughly the same.*

### 2.4.3. SSCs from OBS, ASM and ADV

The $T_{ASM}$ saturated (with a reading around 4000 FTU) during the early ebb, suggesting a high SSC > ~9 g/L in July 2014. Meanwhile, a significant reduction in $T_{OBS}$ and SNR occurred. Such responses of $T_{ASM}$, $T_{OBS}$ and SNR to high SSCs can be reproduced in the laboratory experiments (Figures 2-1 and 2-2). It indicates that the response of each sensor is stable and reliable in the lab and the field.

Figures 2-6d (July 2014) and 7d (January 2016) show ASM-, OBS- and ADV-derived SSC at 0.35 mab. All SSCs given by sensors follow similar intra-tidal variations as the water sampling results. However, the OBS and ADV give higher SSCs (> 60 g/L), while the ASM only provides reliable estimates of <9 g/L.

The ADV also provides estimates of turbulent sediment flux ($\overline{w'c'}$). The observed $\overline{w'c'}$ had a tidally averaged magnitude of $10^{-4}$ kg/m$^2$/s and reasonable intra-tidal variation, similar to the theoretical calculations ($\frac{\upsilon_t}{\sigma_t}\frac{\partial c}{\partial z}$) (Figure 2-8). $\upsilon_t$ is the eddy viscosity given by

$$\upsilon_t = \left(\overline{u'w'}\frac{\partial \bar{u}}{\partial z} + \overline{v'w'}\frac{\partial \bar{v}}{\partial z}\right)\left[\left(\frac{\partial \bar{u}}{\partial z}\right)^2 + \left(\frac{\partial \bar{v}}{\partial z}\right)^2\right]^{-1}. \quad (2.1)$$

where $\sigma_t$ is the turbulent Prandtl–Schmidt number, relating eddy viscosity ($\upsilon_t$) to eddy diffusivity ($K_t$), as $K_t = \upsilon_t/\sigma_t$. A common assumption is that $\sigma_t$ = 0.7. In highly turbid environments (e.g., the Changjiang Estuary), however, $\sigma_t$ = 2.0 gives the optimal modelling of currents and SSCs (Winterwerp et al., 2009). Direct comparison between the calculations ($\frac{\upsilon_t}{\sigma_t}\frac{\partial c}{\partial z}$) and in-situ measurements ($\overline{w'c'}$), verifies that $\sigma_t$ = 2.0 gives a better estimate than $\sigma_t$ = 0.7 (Figure 2-8).

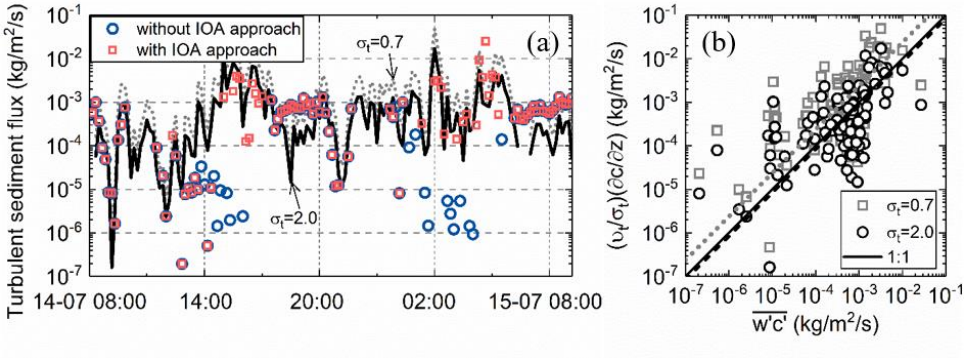


*Figure 2-8: Comparison between ADV-derived turbulent sediment flux ($\overline{w'c'}$) and the theoretical calculations ($\frac{\upsilon_t}{\sigma_t}\frac{\partial c}{\partial z}$) with two classic values of turbulent Prandtl–Schmidt number, i.e., $\sigma_t$ = 0.7 and $\sigma_t$ = 2.0. (a) ADV-derived $\overline{w'c'}$ with and without the proposed algorithm are also presented.*

### 2.4.4. The optimal algorithm in the IOA approach

Averaged relative errors evaluate the performance of each sensor, as

$$Relative\ error = \frac{\overline{|C_{calculated} - C_{observed}|}}{\overline{C_{observed}}} \times 100\% \quad (2.2)$$

where $C_{calculated}$ is the SSC estimated by sensors; $C_{observed}$ denotes the SSC from the filtration of water samples (Druine et al., 2018).

Table 2-4 summarises the relative error and measurement range of each sensor. ASM-derived SSC contains the lowest relative error (~25%), although it has a limited measurement range (< 9 g/L). The ASM also provides high-resolution SSC profiles when it is not saturated. Our proposed algorithms successfully extend the measurement range of OBS to ~60 g/L, and OBS-derived SSC has a relative error of about 30%. Although the ADV has the most extended measurement range (~360 g/L), its estimates contain the most significant uncertainty (relative error > 80%), so the best it can be used is to have a rough estimation and assist in the conversion of OBS. We suggest an optimised algorithm for the IOA approach based on sensor performances (Figure 2-4). The ASM-derived SSC is preferred as long as the ASM is unsaturated. Under ASM-saturated conditions, the OBS can recover the missing high SSC. The ADV can provide a rough estimation of the trend and reduce the uncertainty in the OBS conversion.

*Table 2-4: Measurement ranges (g/L) of ASM, OBS and ADV with their relative errors (%). Missing values are represented by the symbol NA (Not Available).*

| Time | Instrument | Range (g/L) | Relative error (%) |
|---|---|---|---|
| 201407 | ASM | 0.0-8.0 | 33.6 |
| | OBS-633 | 0.2-66.0 | 32.2 |
| | OBS-636 | 0.2-65.9 | NA |
| | OBS-638 | 0.1-59.2 | NA |
| | ADV | 0.1-457.3 | 88.6 |
| 201601 | ASM | 0.0-7.4 | 17.6 |
| | OBS-278 | 0.2-61.1 | 28.2 |
| | OBS-279 | 0.2-57.0 | NA |
| | OBS-570 | 0.2-56.1 | NA |

### 2.4.5. Performance of the IOA approach

Figure 2-9 shows estimated SSC profiles, highlighting the advantages of the IOA approach. The conventional method (i.e., without the IOA approach) provides estimates only by OBSs at three layers (i.e., 0.35, 0.55 and 1.06 mab). In this case, the high-SSC-induced attenuation cannot be identified. Furthermore, only the results below the saturation point are reliable (e.g., curve 2 in Figure 2-3), which may underestimate high SSCs.

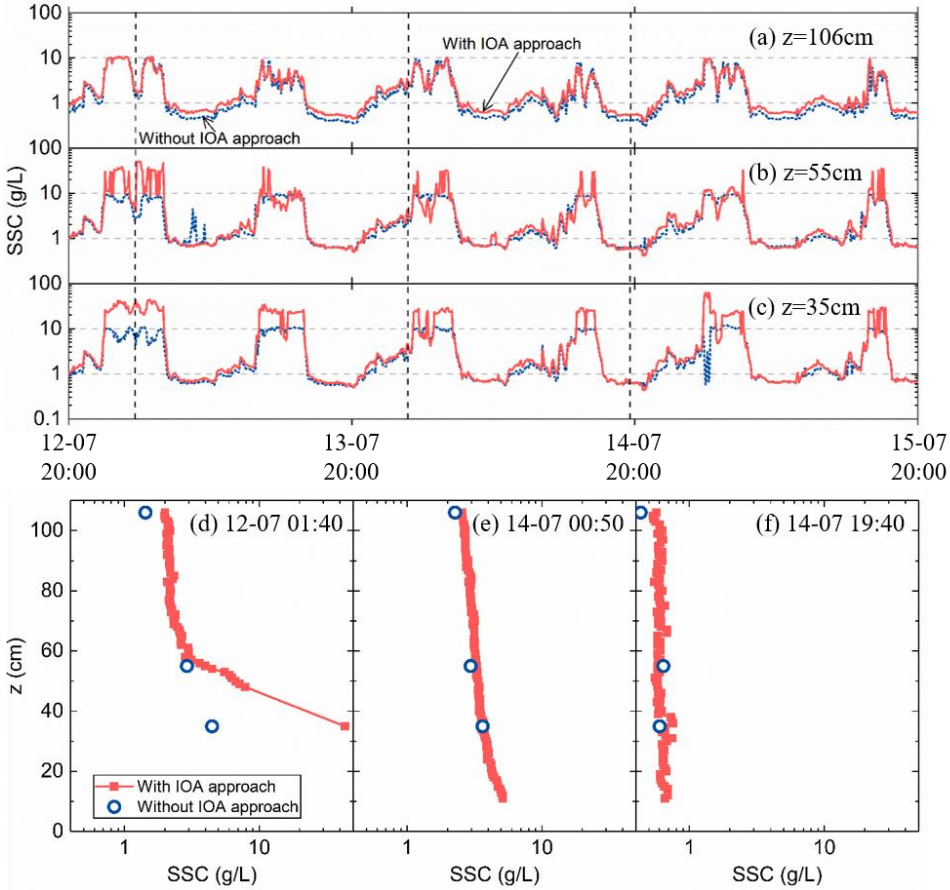


*Figure 2-9: Time series of SSC from three tripod-mounted OBSs with (black solid) and without (grey dot) the IOA approach at 106 cm (a), 55 cm (b) and 35 cm (c) above the bed and three representative SSC profiles within high (d), mid (e) and low (f) SSC. The ASM readings within 50 cm above the bed are saturated (d) and thus removed. The OBS recovered the SSC at 35 cm above the bed. A straight line between the SSCs from ASM at 35 and 50 cm is suggested as the possible SSC profile.*

At low SSCs (<10 g/L), the two methods (with and without the IOA approach) give similar SSC estimates (Figure 2-9a). However, significant differences appear near the bed (Figure 2-9b and c). The SSC can be significantly underestimated, and it was generally smaller than 10 g/L without the IOA approach when it was actually up to 63 g/L.

The ASM confirms the OBS results and provides high-resolution SSC profiles (Figure 2-9d, e and f). Ninety-six estimates are given in a profile with a vertical resolution

of 1 cm. However, without the IOA approach, only three estimates are given by the OBSs. The IOA approach provides a more reasonable and reliable SSC profile when the near-bed high SSC appears. At 01:40 am, July 12 (Figure 2-9d), the proposed IOA approach estimated an SSC of ~40 g/L at 0.35 mab, while an SSC of ~4 g/L was obtained without the IOA approach. The ASM results show a sudden increase in SSC at 0.55 mab, suggesting the reliability of SSC profiles given by the IOA approach.



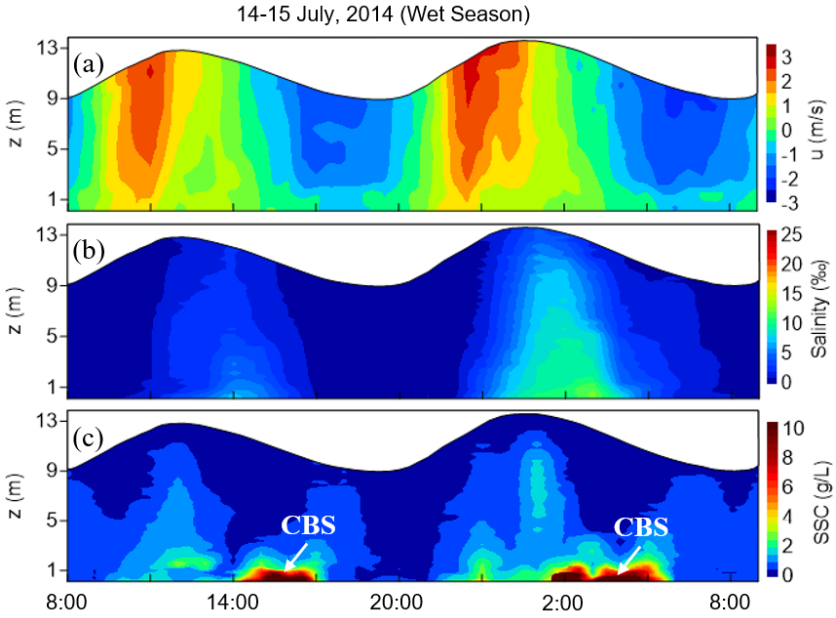


*Figure 2-10: Time-depth variability of (a) along-channel velocity (u), (b) salinity and (c) SSC during 14-15 July 2014. Positive u indicates the flood direction. CBS denotes the concentrated benthic suspension (SSC > 10 g/L).*

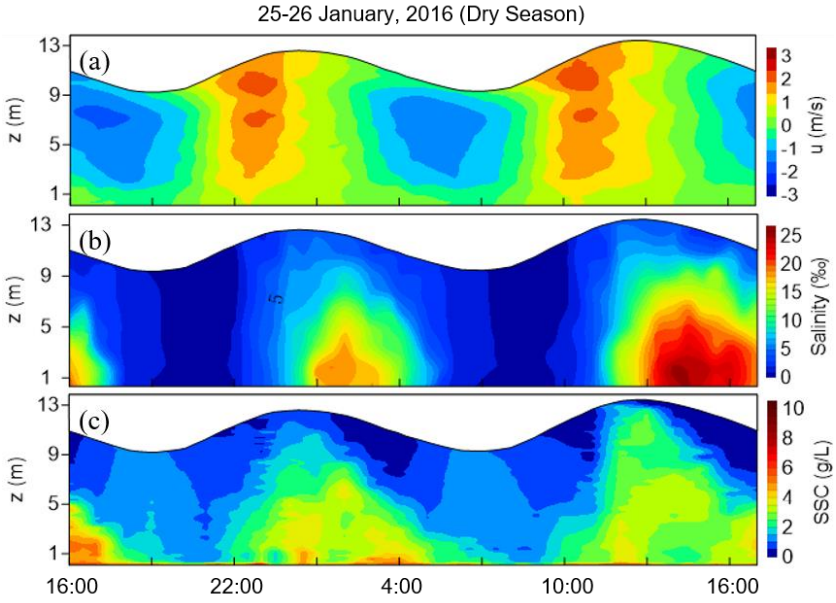


*Figure 2-11: Time-depth variability of (a) along-channel velocity (u), (b) salinity and (c) SSC during 25-26 January 2016. Positive u indicates the flood direction.*

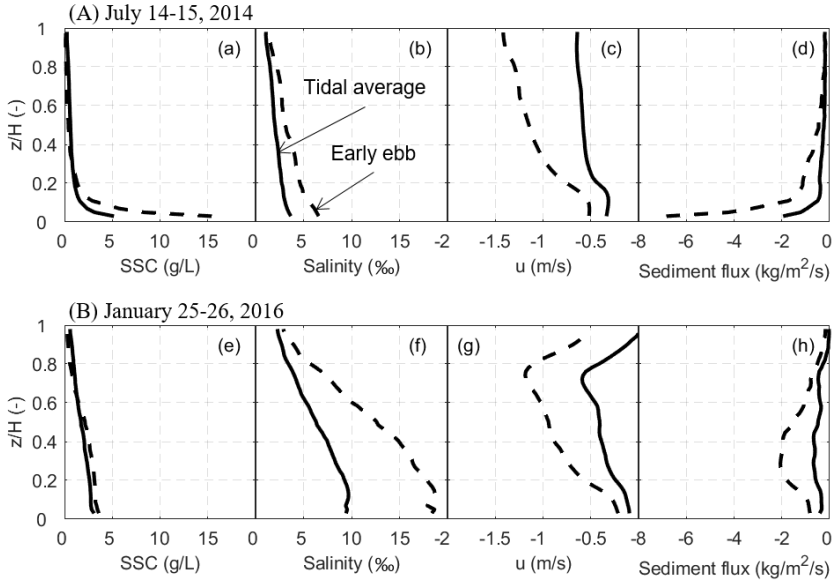


*Figure 2-12: Profiles of (a) (e) SSC, (b) (f) salinity, (c) (g) along-channel velocity (u) and (d) (h) along-channel sediment flux averaged over tidal cycles (solid line) and early ebb (dash line) of spring tide in July, 2014 (upper panels) and January, 2016 (lower panels). Negative u and flux indicate the direction from land to sea.*

The IOA approach with the optimised algorithm allows high temporal and vertical resolutions of SSC variabilities. Particularly on the early ebb in July 2014, the concentrated benthic suspension (CBS) was successfully captured and measured. The observed CBS persisted for 3-4 hours, with a thickness of ~1 m (Figure 2-10c). In the wet season (Figure 2-12a), the SSC profile was L-shaped with a higher near-bed SSC (up to 63 g/L). In addition, a significant SSC gradient was observed in the lowest 0.2H. However, the SSC profile was more uniform in the dry season (Figure 2-12e). The SSC showed the highest value just above the bed and decreased almost linearly to the surface.



## 2.5. Discussion

### 2.5.1. Sources of uncertainties

Although with improvement, the sensors and the obtained SSCs are somehow embedded with uncertainties and bias. The OBS and ASM turbidities, for example, have an uncertainty of ±10% (Argus, 2014; Campbell Scientific, 2018). Since a linear regression is applied for the ASM calibration, this uncertainty will cause a relative error of 10% in ASM-derived SSCs. Regarding the OBS, this uncertainty could lead to a relative error of 10% in the linearly increasing and decreasing region (i.e., curves 2 and 5 in Figure 2-3a) but up to 90% around the turning point (i.e., curves 3 and 4 in Figure 2-3a). Furthermore, since the SNR is calibrated against the SSC on a logarithmic scale, the relative error caused by the SNR uncertainty increases with increasing SSC. For example, near the turning point (SSC = 2 g/L), an SNR uncertainty of ±1% (Nortek, 2005) causes a relative error of 30%. However, the relative errors in Table 2-4 are higher than those caused by the uncertainty of raw signals, which indicates additional sources for the given relative errors.

In this study, the sensors were evaluated by water samples in the bottom layer (0.95H, i.e., ~0.45-0.65 mab), while the sensors were deployed at 0.35 mab. This height difference may enlarge the estimated relative error, particularly when a large near-bed SSC gradient presents (e.g., July 2014). Besides, the ADV was calibrated by the OBS- or ASM-derived SSCs. Therefore, the uncertainty and bias of ADV-derived SSCs may accumulate from those of the OBS or ASM. In other words, the relative error of the ADV-derived SSC is also overestimated.

Since the grain size and composition of suspended sediment can affect the responses of optical and acoustic sensors (Conner and De Visser, 1992; Gibbs and Wolanski, 1992; Green and Boon, 1993; Merten et al., 2014; Su et al., 2016; Druine et al., 2018), tidal variations of grain size or sediment composition could also introduce errors to SSC estimates. In the Changjiang Estuary, the size and density of

flocculates continuously change in response to the complex advection, resuspension, deposition and flocculation processes (Guo et al., 2017). During the campaign in July 2014, the median grain size of primary particles ($D_{P50}$) ranged 4-20 μm, with an average of ~10 μm. Primary sediment particles were larger in January 2016 (Table 2-5). In addition, the clay, silt and sand content varied with time and depth (Figure 2-13 and Table 2-5). In July 2014, for example, both floc size (15-90 μm) and density (80-800 kg/m$^3$) had a broad range. Such notable variations in grain size and floc density could be one of the sources of relative errors in SSC estimates.



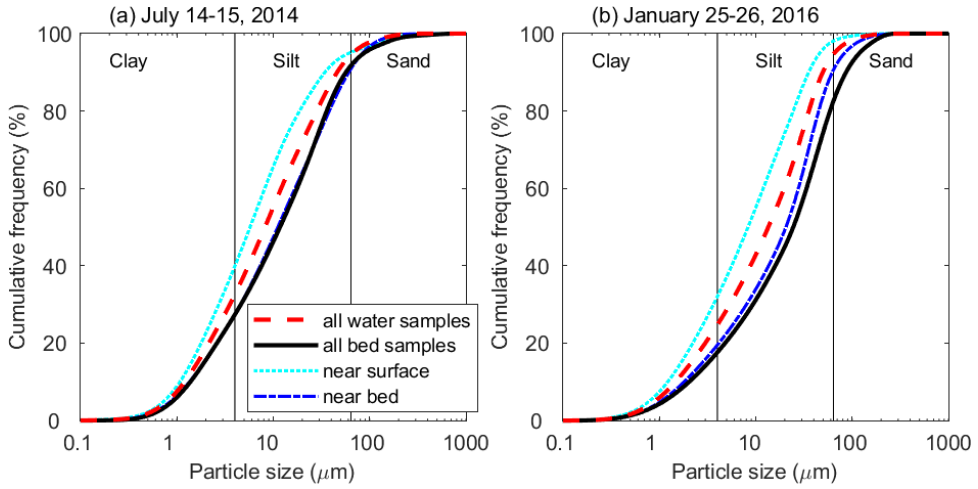


*Figure 2-13: The cumulative frequency distribution of the sediment samples collected near the water surface (dot), near the bed (dash-dot), and at the seabed surface (solid) in July 2014 (a) and January 2016 (b). The dashed line represents the average of all water samples.*

In sensor calibrations, we reduce the effects of particle size by using the mixture of bottom sediment collected every 2 hours during the campaign. This mixture represents the tidally averaged condition of suspended sediment in the bottom layer (Figure 2-13). The calibration thus returns a representative curve for a tide-averaged condition. The proposed IOA approach gives SSC estimates with 17–34% relative errors upon these calibrations. These errors are acceptable for in-situ SSC measurements and the quantification of sediment transport.

*Table 2-5: Tidally averaged median grain sizes of primary particles ($D_{P50}$) and flocculates ($D_{F50}$), dry density of flocculates ($\rho = \bar{c}/V_c$, where $\bar{c}$ is the sediment concentration of water samples, and $V_c$ is the volume concentration measured by LISST) and composition of suspended sediment in different layers with their standard deviations. Data are not available in the bottom layer as LISST does not work correctly in high turbidity. Missing values are represented by the symbol NA (Not Available).*

| Time [yymm] | Position | $D_{P50}$ (std.) [µm] | $D_{F50}$ (std.) [µm] | ρ (std.) [kg/m$^3$] | $P_{clay}$ (std.) [%] | $P_{silt}$ (std.) [%] | $P_{sand}$ (std.) [%] |
|---|---|---|---|---|---|---|---|
| 1407 | 0.05H | 6.0(±1.4) | 26.3(±8.8) | 310(±84) | 39(±6) | 56(±8) | 5(±6) |
| | 0.2H | 7.3(±2.1) | 24.7(±7.4) | 311(±91) | 35(±6) | 61(±7) | 4(±4) |
| | 0.4H | 8.9(±3.3) | 25.7(±10.7) | 304(±130) | 32(±6) | 64(±4) | 4(±4) |
| | 0.6H | 10.4(±4.0) | 27.5(±16.3) | 275(±82) | 30(±5) | 65(±3) | 5(±5) |
| | 0.8H | 11.6(±4.2) | 33.9(±19.5) | 238(±78) | 28(±5) | 66(±2) | 6(±5) |
| | 0.95H | 13.5(±6.0) | 33.3(±6.3) | 246(±42) | 27(±6) | 63 (±3) | 10(±7) |
| | Bed | 12.1(±2.7) | NA | NA | 27(±3) | 64(±5) | 9(±3) |
| | All samples | 9.8(±4.5) | 27.6(±12.8) | 288(±97) | 32(±7) | 62(±6) | 6(±5) |
| 1601 | 0.05H | 9.4(±4.0) | 23.7(±5.4) | 502(±339) | 31(±7) | 66(±6) | 2(±2) |
| | 0.2H | 12.6(±5.8) | NA | NA | 27(±6) | 69(±4) | 4(±3) |
| | 0.4H | 14.6(±5.2) | NA | NA | 25(±5) | 71(±3) | 4(±3) |
| | 0.6H | 16.2(±5.0) | NA | NA | 22(±4) | 72(±2) | 6(±4) |
| | 0.8H | 18.6(±5.4) | NA | NA | 21(±4) | 71(±3) | 8(±4) |
| | 0.95H | 21.1(±5.9) | NA | NA | 19(±4) | 71(±3) | 10(±5) |
| | Bed | 26.7(±11.6) | NA | NA | 17(±5) | 65(±5) | 18(±10) |
| | All samples | 16.2(±7.6) | NA | NA | 24(±7) | 70(±4) | 6(±6) |

### 2.5.2. Advantages and disadvantages of the IOA approach

Based on the IOA approach, both OBS and ADV access a broader measurement range of SSC (Table 2-4), as the ambiguity problem in conversion is solved. Upon the calibration in high SSCs, the OBS can provide estimates of >300 g/L (Kineke and Sternberg, 1992). Although the ADV also has an extended measurement range (>300 g/L), the best way it can be used is to give a rough estimation and assist in OBS conversion because of the significant uncertainty in its estimates. With the IOA approach, we successfully captured and measured the CBS (SSC > 10 g/L) in the Changjiang Estuary.



The IOA approach also provides high-resolution SSC profiles by the ASM. In this study, the ASM was deployed on a tripod and measured the SSC profiles in the bottom boundary layer. These profiles have a higher resolution (0.01 m) than those measured by acoustic sensors (0.25-1.0 m), e.g., ADCP (Anastasiou et al., 2015; Baeye and Fettweis, 2015) and ADP (Fettweis and Baeye, 2015). However, the ASM can only produce valid high-resolution SSC profiles when it is not saturated. Once the ASM sensor is saturated, the estimate given by ASM is missing. The OBS can recover this missing value.

The IOA approach also provides direct and reliable measurements of turbulent sediment flux ($\overline{w'c'}$) by the ADV. Unlike optical sensors, the ADV provides estimates of turbulent velocity ($w'$) and SSC ($c'$) directly at the same position. Figure 2-8 shows the ADV-derived $\overline{w'c'}$ with and without the IOA approach and the theoretical calculations with $\sigma_t$ = 0.7 and 2.0. Without the IOA approach, the $\overline{w'c'}$ is significantly underestimated (Figure 2-8a). The $\overline{w'c'}$ with the IOA approach, however, maintains close to the theoretical calculation with $\sigma_t$ = 2.0, which is consistent with the observations by Cellino and Graf (1999) and modelling results by Winterwerp et al. (2009) in highly turbid water.

The IOA approach and the optimised algorithm, however, are not perfect. First, the sensor responses to SSC are not entirely the same between the field and laboratory experiments. The OBS, for example, had a small amount (<1%) of outputs during the field campaign that exceeded the maximum turbidity (~3400 NTU) obtained in the in-lab calibration experiment. Part of the SSC given by the IOA approach is therefore missing. Maa et al. (1992) suggested that clay mineralogy and salinity can affect the OBS response to SSCs. In our study, the sediment samples used in the calibration were collected from the bed surface at the survey site. Their clay mineralogy thus did not change too much compared with the near-bed suspensions (Figure 2-13). The salinity, however, ranged from 0-12‰ during the field measurement in July 2014, whereas the mixture of water samples returned a

representative mean salinity of 5‰ in the in-lab calibration. Therefore, the salinity of ambient water is likely the main reason for the difference between the in-lab and in-filed response of an OBS, and in-situ calibration is recommended. Second, the effects of particle size are not considered in the proposed algorithm. Careful calibrations with the particle size correction (Green and Boon, 1993; Su et al., 2016) are suggested in future applications to improve the accuracy.

### 2.5.3. Seasonal SSC profiles



The two studying periods (wet and dry seasons) show different vertical SSC profiles (Figure 2-12a and e). Near-bed SSC is higher in the wet season than in the dry season. Such a seasonality may correlate with the locations of salinity wedge and ETM, estuarine stratification, floc size and settling velocity.

In the dry season, both the salinity wedge (Figures 2-11b and 2-12f) and ETM (Wan, 2015; Figure 7-12) locate further upstream, and thus the lower half of the water column may have a more uniform SSC profile because of the thick salinity wedge and better mixing capability, especially in the lowest 0.2H (Figure 2-12e). However, the wedge moves downstream in the wet season, and only its head can reach the survey station (Figures 2-10b and 2-12b). Therefore, the observed wedge is relatively thin, and the near-bed mixing is weak. As a result, the vertical SSC gradient is high near the bed. Furthermore, the thickness of the wedge is more than 2 m, so a high SSC gradient was observed at the experimental site. In other words, the near-bed SSC in the channel could be higher than that observed at the survey station.

In addition to wedge and ETM movement, increased freshwater discharge may enhance strain-induced stratification (Simpson et al., 1990) and estuarine circulation (Wan, 2015). Enhanced stratification benefits sediment trapping near the bottom (Geyer, 1993), while the circulation accumulates sediment in the convergent zone (i.e., ETM). Overall, the SSC and its gradient are high near the bottom in the wet season. Although stronger residual currents (Figure 2-12c and g) occur in the wet season, depth-integrated sediment flux (Figure 2.12d and h) is similar. Because of the increasing sediment supply from the upstream (L. Guo et al., 2018), sediment accumulation accelerates in the wet season, reaching a higher SSC.

In addition, the seasonality of SSC profiles may result from the changes in floc size and settling velocity. Both floc size and settling velocity are enlarged in the wet season, and thus the suspension is more concentrated in the near-bed layer because of the low turbulent shear (Wu et al., 2012) and high chlorophyll concentration (Fettweis and Baeye, 2015; Deng et al., 2019); and vice versa in the dry season.

However, the quantification of the above processes requires detailed flocs, turbulence, and ETM data.

### 2.5.4. Intra-tidal SSC variation

Based on in-situ and laboratory measurements, Maa and Kim (2002) and Ha and Maa (2009) found that erosion only occurs when the tidal current is in acceleration phases, which may explain the intra-tidal SSC variations during our observations. Besides, the survey site is located on the land side of the tidally-averaged ETM (Wan, 2015; see Figure 7-12), and thus horizontal advection may contribute to the changes in local SSCs.



During the flood periods in the wet season, the SSC increases at a reasonable pace whenever the current accelerates (Figure 2-6d). This slight increase may be attributed to the re-dispersion of new deposits from previous slack tides and landward ETM movements. Conversely, the SSC decreases when flows start decelerating. The cut-off of sediment supply from the bed and the deposition during the late flood are responsible for this decrease. The SSC jumps (or increases quickly) during ebb periods right after tidal currents accelerate. Then, it suddenly decreases and recovers in 1-2 hours during this phase. There is a significant shoal-to-channel flow (Figure 2-6b) for the decreasing SSC and vice versa for the increase. It suggests that lateral flows control the rapidly increasing or decreasing SSC during these periods. The SSC drops when flows start decelerating. The withdrawal ETM (i.e., seaward movement) may predominate the rapid decrease, while the constant SSC may result from limited sediment supply from the seabed.

In the dry season (Figure 2-7d), the changes in SSC during the accelerating flood and the decelerating ebb have a similar pattern to those in the wet season. However, when flood currents change to deceleration phases, the SSC first increases and then decreases gradually. A slight increase occurs during the accelerating ebb, followed by a slight decrease. Such variations during these two phases cannot be explained only by asymmetric erosion/deposition. Longitudinal ETM movement may predominate these changes. Because of the low freshwater discharge, the salinity wedge and the ETM can intrude further upstream. The ETM may even pass the observation station, increasing local SSCs during the decelerating flood. The decrease during the accelerating ebb may result from the withdrawal of ETM.

The difference between these two survey periods is probably caused by the different locations and distribution of ETM. The ETM appears as a concentrated undercurrent in the wet season and a low concentration sediment cloud in the dry season (Wu et al., 2012). A significant horizontal SSC gradient thus occurs in the wet season,

especially in the cross-channel direction. In the branched Changjiang Estuary, the cross-channel current is caused by the barotropic force induced by the cross-shoal flow (Zhu et al., 2018). Although the cross-channel current is roughly the same during these two seasons (Figures 2-6b and 2-7b), it provides a much stronger advective transport of SSC in the wet season because of enlarged SSC gradients. Such a cross-channel transport of SSC is even stronger than that from the erosion of bottom sediment. At the ETM, both along- and cross-channel advection contribute significantly to local SSC changes; thus, the asymmetric erosion/deposition is not as clear as Maa and Kim (2002) observed. More discussion/studies on the dominant process that controls intra-tidal SSC variation are needed, including detailed data on longitudinal and lateral distributions of the ETM and flow velocities.



## 2.6. Conclusions

This work suggests combining OBS, ASM, and ADV to detect large SSC accurately. We successfully solve the ambiguity problem and get a broader measurement range and high-resolution SSC profiles. The ASM-derived SSC is preferred because it has the lowest relative error (~25%). The ASM also provides high-resolution (1 cm) SSC profiles when it is not saturated (SSC < 9 g/L). Once the ASM is saturated, the OBS can be used. Both OBS and ADV can extend their measurement range up to 300 g/L. Although the ADV has a broader SSC range, the best it can be used is to have a rough estimation and assist in converting OBS outputs. We suggest using in-situ water samples or mixed bottom sediment for sensor calibrations to reduce particle size effects. Alternatively, one can take particle size correction into account in the calibration to access a higher accuracy.

The application of the IOA approach successfully captured and measured the concentrated benthic suspensions (SSC > 10 g/L) in the Changjiang Estuary. This method is reliable and gives estimates with 17–34% relative errors. The SSC profiles in the Changjiang Estuary show a notable seasonal variation. Suspended sediment accumulates in the benthic layer in the wet season, forming an L-shaped profile, whereas a uniform and linear profile in the dry season.

# 3. The Roles of Concentrated Benthic Suspensions and Drag Reduction‡


‡ Parts of this chapter have been published in: Lin, J., van Prooijen, B.C., Guo, L., Zhu, C., He, Q., Wang, Z.B., 2021. Regime shifts in the Changjiang (Yangtze River) Estuary: The role of concentrated benthic suspensions. Mar. Geol. 433, 106403. https://doi.org/10.1016/j.margeo.2020.106403

*Channel deepening often triggers a positive feedback mechanism between tidal deformation, sediment import and drag reduction, which leads to the regime shift in estuaries from low-turbid to hyper-turbid states. This chapter hypothesises a transition in suspended sediment concentration profiles (SSC) by including a positive feedback loop of vertical mixing and settling. Such a hypothesis is validated by the historical observations in the North Passage of the Changjiang (Yangtze River) Estuary, with decreasing SSC in mid-lower layers and increasing SSC near the bed after the deepening. A mobile pool of concentrated benthic suspensions (CBS) develops in the North Passage, with a tidally averaged length of ~20 km and a mean thickness of ~4 m. The width of the CBS pool is limited (<1 km) as the CBS is concentrated in the Deepwater Navigational Channel. The movements of the CBS pool, combined with the tidal asymmetry (e.g., slack-water asymmetry and lateral flow asymmetry), result in sediment trapping in the middle reaches and on the south flank of the channel. The observations by a bottom tripod system show the response of friction/drag coefficient to sediment concentration: (1) nearly linear decrease in low SSC (<10 kg/m$^3$); (2) constant and minimum coefficient (with a drag reduction up to 60%) in the presence of CBS (10-80 kg/m$^3$). An empirical relationship was derived that can be used to predict friction coefficient and the magnitude of drag reduction for sediment transport studies, particularly for modelling the regime shift in estuaries.*

# 3.1. Introduction

In estuaries, the region where suspended sediment concentrations (SSC) are higher than in adjacent waters is called the estuarine turbidity maximum (ETM). ETMs are of great importance for the natural and socio-economic value of estuaries, as they affect light availability (Yoshiyama and Sharp, 2006; Cloern et al., 2014), oxygen levels (Uncles et al., 1998; Talke et al., 2009a) and dredging for navigational channels (Liu et al., 2011).

In order to control flooding and accommodate larger ships, many estuaries are heavily engineered, such as deepening by dredging and narrowing by land reclamations. After the engineering works, Winterwerp et al. (2013) observed a regime shift in SSC from low- to hyper-turbid states in the Ems Estuary (Netherlands, Germany) and Loire Estuary (France). They attributed this transition to deepening (dredging) and hypothesised a positive feedback loop for the regime shift in estuaries (Winterwerp and Wang, 2013). According to their hypothesis, channel deepening results in tidal amplification or, more generally, tidal deformation (van Maren et al., 2015). As a result, fine sediment import increases, leading to a higher SSC. The higher SSC causes turbulence damping and drag reduction, enhancing tidal deformation. A feedback loop is formed.



A crucial step in the analysis of Winterwerp et al. (2013) is the impact of suspended sediment on the effective hydraulic drag, upon which the response of estuaries to narrowing and deepening becomes amplified. By lowering the drag, various (idealised or complex) models reproduced the upstream shift in the ETM position and the transition to high SSC after the channel deepening (Chernetsky et al., 2010; de Jonge et al., 2014; van Maren et al., 2015). These results, however, were based on recalibration. The model thus did not resolve the reduced roughness itself, and the transition was not dynamically modelled.

Theoretical expressions for the drag coefficient are a function of the (flux) Richardson number (Wang, 2002; Winterwerp et al., 2009). The semi-analytical approach by Winterwerp et al. (2009) was used to analyse the tidal response to river engineering works (Winterwerp and Wang, 2013). Their analyses present a snowball effect between tidal amplification, sediment import and drag reduction. Dijkstra et al. (2019) went one step further and dynamically modelled the transition in SSC by including a reduced drag coefficient in their model. Their results highlight the role of drag reduction in the sediment import capacity of the system and hence the regime shift, supporting the feedback loop proposed by Winterwerp and Wang (2013). In order to reproduce the increase in SSC, Dijkstra et al. (2019) assumed that sediment is efficiently resuspended from the bed. The efficient resuspension was achieved in

their model by choosing a high value for the erosion parameter, including hindered settling and excluding the effect of drag reduction on erosion. However, the validity of such an assumption has not been confirmed by observations. Available field observation to verify the theoretical expressions for drag reduction is scarce.

Studies on the regime shift in estuaries mainly focus on large-scale along-estuary (longitudinal) processes (e.g., tidal deformation and sediment import). Small-scale vertical processes, however, received little attention. The imported sediment may first accumulate near the bed, forming concentrated benthic suspensions (CBS). CBS is defined as a near-bed high-concentration suspension of fine sediment. From a physical perspective, the CBS exhibits notable turbulence damping and hindered settling but remains Newtonian. (Winterwerp, 2002; Bruens et al., 2012). Large vertical SSC gradients exist within a CBS, leading to turbulence damping through buoyancy effects and hence drag reduction (Winterwerp, 2001; Becker et al., 2018). In suspensions with fine sediment (e.g., Severn Estuary and Changjiang Estuary), hindered settling becomes important when SSC is higher than ~10 kg/m$^3$ (Manning et al., 2010; Wan et al., 2015). Rheologic experiments show that a fine sediment suspension behaves as a Newtonian fluid for concentrations of <80 kg/m$^3$ (Wang et al., 1998; Thompson et al., 2006). Therefore, near-bed suspensions of fine sediment with a concentration of 10-80 kg/m$^3$ are considered as CBS in this study.

A positive feedback loop between vertical mixing and settling was assumed to form CBS in estuaries (Winterwerp, 2002; Xu, 2009; Ge et al., 2018). Density stratification, generally initiated by salinity, inhibits vertical mixing through buoyancy destruction (i.e., turbulence damping). Suspended sediment is therefore confined in the bottom layer (Geyer, 1993), leading to decreasing SSC in the upper water columns. Accumulated sediment produces a strong SSC gradient, which strengthens stratification and causes further sediment trapping near the bed (Winterwerp, 2001). With increasing SSC, hindered settling becomes important and provides a favourable situation for near-bed high SSC (Dijkstra et al., 2018). Once a CBS forms, such a positive feedback loop favours the stability of CBS. This feedback loop, combined with the one proposed by Winterwerp and Wang (2013) for the regime shift in estuarine SSC, may result in the transition in vertical profiles of SSC. Since sediment accumulates in the bottom layer, SSC near the bottom may increase earlier than near the surface. In other words, the hyper-turbid state develops from the bed to the water surface during the transition. Although a CBS was frequently found after channel deepening (Wang, 2010; Becker et al., 2018; Lin et al., 2020), no study to date shows the transition in vertical SSC profiles.

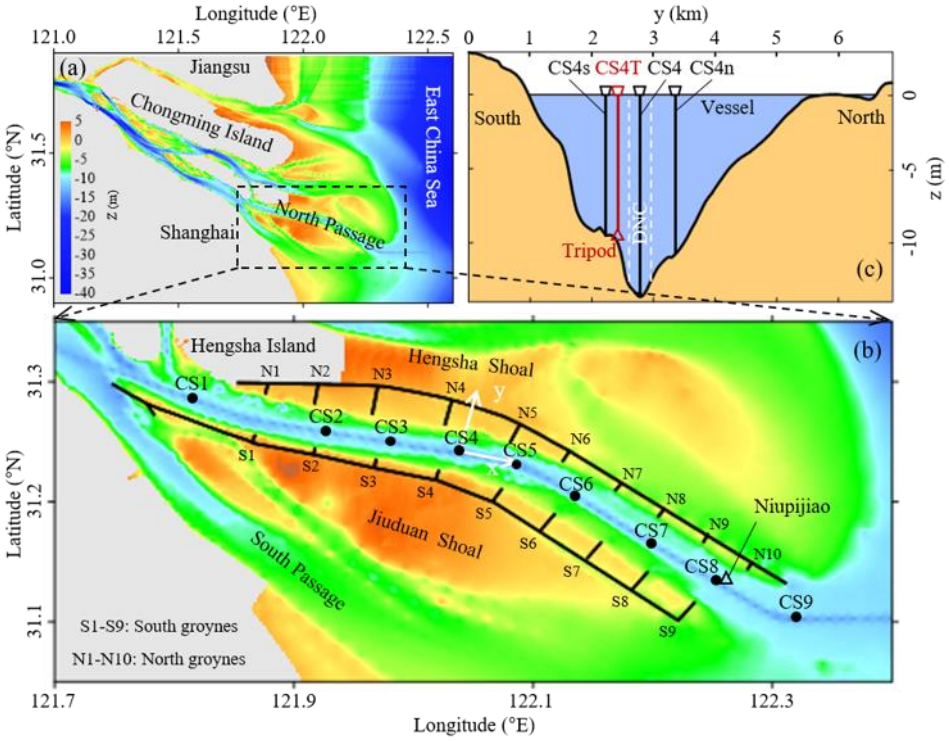


*Figure 3-1: (a) Bathymetry of the Changjiang Estuary. The elevation (z) is relative to the theoretical depth datum. The dashed box indicates the study area, enlarged in panel b. (b) The Deepwater Navigational Channel (DNC), dykes and groins along the North Passage. The dots represent the ship-borne stations deployed in August 2012. The triangle indicates the tide gauging station located in Niupijiao. The x and y coordinates denote the along- and cross-channel direction. (c) A cross-channel transect at CS4. The black lines represent three ship-borne stations deployed in 2012, and the red line denotes the station in 2014, including ship- and tripod-borne observations.*

In this study, we focus on the North Passage of the Changjiang (Yangtze River) Estuary (Figure 3-1), where a Deepwater Navigational Channel was constructed to meet the demand for cargo. The construction was launched in 1998, and the waterway depth was planned in three phases: (1) to 8.5 m in 2002, (2) to 10 m in 2005 and (3) to 12.5 m in 2010 (Liu et al., 2011). After dredging operations, the ETM shifted 10-15 km upstream and became a long turbidity zone between CS2 and CS8 (Jiang et al., 2013). Moreover, the maximum SSC near the bed increased from several to tens of kg/m$^3$ (Jiang et al., 2013; Wan and Zhao, 2017; Lin et al., 2020), although the sediment supply from the Changjiang River declined by 70% (Guo et al., 2019). However, the changes in SSC profiles remain unclear.

This study aims to check whether a transition in SSC profiles occurred in the North Passage and to quantify the drag reduction caused by suspended sediment. This is done by analysing historical SSC observations and near-bed measurements by a tripod system. An introduction to the Changjiang Estuary is given in Section 3.2. Section 3.3 presents the data and methods used in this study. The results are shown in Section 3.4, discussing the change in SSC profiles, mobile CBS pool, drag reduction and tidal asymmetry. The implications of the results to the regime shift and sediment transport in estuaries are discussed in Section 3.5. Finally, the conclusions are summarised in Section 3.6.

## 3.2. Study area



The Changjiang River is one of the largest rivers in terms of river discharge and sediment load. The Datong gauging station, ~640 km upstream from the river mouth, is the tidal wave limit. Here, daily river discharge and sediment load are measured. The annual suspended sediment load at Datong declined from 470 million tons (1953-1985) to 140 million tons (2003-2015) due to soil conservation strategies and dam construction, while the mean river discharge is relatively stable (28,200 $m^3/s$) (Guo et al., 2019). Both freshwater discharge and sediment load show seasonal variation. The discharge is approximately 40,000 $m^3/s$ in the wet season (May-October) and ~10,000 $m^3/s$ in the dry season (November-April) (CWRM, 2015). More than 70% of sediment load is delivered to the estuary in the wet season.

The Changjiang Estuary is partially stratified with moderate tidal forcing. The mean and maximum tidal ranges are approximately 2.7 and 5.0 m, respectively, according to data from the tide gauging located at Niupijiao (Guo et al., 2015). Local mixing and stratification are controlled by tidal currents, saltwater intrusion and freshwater discharge. Stronger stratification occurs in wet seasons and during neap tides (Pu et al., 2015).

The North Passage of the Changjiang Estuary was deepened and dyked, forming a Deepwater Navigational Channel with a width of 350 m and a depth of 12.5 m (referred to the Theoretical Depth Datum). The construction includes two jetties (each 50 km) and 19 groins. After the construction, the saltwater intrusion is enhanced in the upper reaches and reduced in the lower reaches of the North Passage (Zhu et al., 2006). Before the construction, flows could spill over the shallow shoals at high waters, leading to significant lateral (cross-shoal) flows (Song and Wang, 2013; Zhu et al., 2018). After the work, the jetties partially block lateral flows and inhibit the water and sediment exchanges between the channel and shoals.

# 3.3. Data and methods

## 3.3.1. Historical bathymetry and SSC

Bathymetric data in 1986 and 1997 were digitised from marine charts with an accuracy of ±0.2 m. Echo sounders measured the data from 2002 to 2016 with an accuracy of ±0.1 m. We refer to Zhu et al. (2019) for more details on the bathymetric data used in this study. All bathymetric data were converted to be negative downward relative to the theoretical lowest tidal level.

In-situ SSC measurements from 1988 to 2015 were used to investigate the regime shift in the North Passage. All data were obtained near station CS4s (Figure 3-1) during the spring tide of wet seasons, provided by SKLEC and Yangtze Estuary Waterway Administration Bureau. Table 3-1 summarises the conditions during the observations. For each campaign, water samples were hourly collected in six relative-depth layers, i.e., $z/H$ = 0.05 (near the bed), 0.2, 0.4, 0.6, 0.8 and 0.95 (near the surface), where $H$ is the water depth, and $z$ denotes the height above the bed. Each water sample was filtered through a pre-weighed filter (0.45 μm), and the filter was dried at 40 °C for 48 h and reweighed to determine the SSC.



*Table 3-1: Conditions of the in-situ measurements of suspended sediment concentrations in the North Passage*

| Time | Location | Depth (m) | Tidal range (m) | Discharge * ($m^3/s$) |
|---|---|---|---|---|
| 30-31 Jul. 1988 | N31°15.0′, E122°0.5′ | 7.0 | 4.4 | 27900-43200 |
| 29-30 Jun. 1999 | N31°11.5′, E122°8.4′ | 9.0 | 3.6 | 38200-51500 |
| 19-20 Aug. 2005 | N31°14.2′, E122°1.5′ | 10.2 | 4.2 | 36400-49800 |
| 20-21 Aug. 2009 | N31°14.2′, E122°1.5′ | 11.7 | 4.1 | 38600-44800 |
| 17-18 Aug. 2012 | N31°14.2′, E122°1.5′ | 11.9 | 4.5 | 50700-57900 |
| 14-15 Jul. 2014 | N31°13.9′, E122°2.3′ | 12.1 | 4.1 | 34600-47100 |
| 14-15 Aug. 2015 | N31°13.9′, E122°2.3′ | 11.6 | 4.0 | 31000-49800 |

* Discharge measured at the Datong gauging station for 30 days (15 days before and after each observation).

## 3.3.2. Survey and instruments

In order to study the CBS effects on the regime shift in SSC, two series of measurements were used in this study. Both were observed in the North Passage of

the Changjiang Estuary. The Changjiang Estuary Waterway Administration Bureauin performed one in August 2012. Parts of these measurements have been published by Wan (2015). SKLEC conducted the other campaign in July 2014. Table 3-2 summarises the instruments employed and their configurations during the fieldwork. All data were collected during the spring tide of wet seasons under calm conditions (no storms). The wind speed was <6 m/s, and the significant wave height was <0.2 m. The discharges measured at Datong were ~57,000 $m^3/s$ and ~44,350 $m^3/s$ during the observation in 2012 and 2014, respectively.

In August 2012, velocity, salinity and SSC profiles were simultaneously measured in an along-channel transect with nine stations (CS1, CS2, CS3, CS4, CS5, CS6, CS7, CS8 and CS9; Figure 3-1b). The spacings between stations from upstream to downstream are 10.7, 4.1, 4.9, 5.5, 6.8, 6.6, 6.5 and 7.2 km, respectively. Meanwhile, profiles were collected in a cross-channel section with three stations (CS4s, CS4 and CS4n from south to north) (Figure 3-1c). The spacing between stations is ~500 m. Flow velocity and direction were obtained by rotor current meter (RCM), and SSC and salinity were derived from water samples. These data were collected every 30 min in the six relative-depth layers. This observation lasted for 13 hours, covering a tidal cycle during spring tides.



To access high-resolution profiles of velocity, salinity and SSC near the bed, we deployed a tripod system in July 2014. The tripod system was located at CS4T, ~200 m away from the Deepwater Navigational Channel (Figure 3-1c). A downward-looking Acoustic Doppler Current Profilers (ADCP-down, 1.0 MHz high-resolution profiler, Nortek AS, Norway) obtained velocities from 0.1 to 0.8 m above the bed (mab here-after) with a resolution of 0.05 m. An upward-looking ADCP (ADCP-up, 600-kHz, Teledyne RD Instruments) was placed at 1.2 mab to measure the velocity profiles in the upper water column with a cell size of 0.5 m. A downward-looking Acoustic Doppler Velocimeter (ADV, Nortek Vector) measured velocities at 0.35 mab with a sampling frequency of 8 Hz. The ADV worked continuously for 90 seconds every 10 min. The sensors in the ADV were also used to monitor the heading, pitch and roll state of the tripod. An Argus Surface Meter-IV (ASM) measured turbidity profiles from 0.11 to 1.06 mab at a resolution of 1 cm. Optical Backscattering Sensors (OBS, D&A Instruments CO, type: 3A, USA) were placed at 0.35, 0.55 and 1.06 mab to measure turbidity, salinity and temperature near the bed, respectively. Ship-borne measurements include profiles of velocity, salinity and turbidity measured by ADCP and OBS.

Water samples were hourly collected in the six relative-depth layers to calibrate the OBSs and ASM. Upon careful sensor calibration, the ASM- and OBS-derived SSC contain a mean relative error of 25% and 30%, respectively (Lin et al., 2020).

*Table 3-2: Shipboard and tripod instruments and their sampling configurations*

| Time | Carrier | Instrument deployed | Height above the bed (m) | Sampling interval (min) | Sampling configuration | Survey parameter |
|---|---|---|---|---|---|---|
| 201208 | Vessel | RCM | * | 30 | 1 Hz × 30 s | Velocity |
| | | Sampler | * | 30 | - | Salinity, SSC |
| 201407 | Vessel | ADCP | H-0.5 | 10 | 0.5 Hz, cell size: 0.5 m | Velocity profiles |
| | | OBS | * | 60 | 1 Hz × 30 s | Salinity, temperature, and SSC |
| | | LISST | * | 60 | 1 Hz × 30 s | Floc size distribution |
| 201407 | Tripod | ADCP-down | 1.0 | 5 | 1 Hz × 60 s, cell size: 0.05 m | Velocity profiles |
| | | ADCP-up | 1.2 | 5 | 0.5 Hz × 60 s, cell size: 0.5 m | upper velocity, wave |
| | | ADV | 0.35 | 10 | 8 Hz × 90 s | near-bed velocity |
| | | RBR | 1.1 | 5 | 4 Hz × 60 s | Wave conditions |
| | | CTD | 0.35 | 5 | 1 Hz × 60 s | Salinity, temperature, and depth |
| | | ASM | 0.11-1.06 | 5 | 1 Hz × 60 s, cell size: 0.01 m | SSC profiles |
| | | OBS | 0.35, 0.55, 1.06 | 5 | 1 Hz × 60 s | Salinity, temperature, and SSC |

The symbol * denotes that the instrument was moved from the water surface to the bed, collecting data in six relative-depth layers, i.e., $z/H$ = 0.05 (near the bed), 0.2, 0.4, 0.6, 0.8 and 0.95 (near the surface), where $H$ is the water depth, and $z$ denotes the height above the bed.

### 3.3.3. Friction velocity and drag coefficient

This study aims to quantify the drag reduction, i.e., the reduction in bed shear stress induced by suspended sediment. The shear stress ($\tau$) in a suspension is defined by

$$\tau = -\rho\overline{u'w'} \tag{3.1}$$

with $\rho$ as the density of the suspension, flow velocity fluctuations $u'$ and $w'$ in streamwise and vertical directions. The drag coefficient relates the bed shear stress to the mean flow (Wang et al., 1998; Thompson et al., 2006; Burchard et al., 2011; Zhu et al., 2016):

$$\tau = \rho_b u_*^2 = C_{D(z)}\rho_{(z)}u_z^2 = \frac{f}{8}\rho_d u_d^2 \tag{3.2}$$

where $\rho_b$ is the fluid density near the bed, and $u_*$ is the shear/friction velocity; $C_{D(z)}$, $\rho_{(z)}$, and $u_z$ are the drag coefficient, fluid density, and mean velocity at the height of $z$ above the bed, respectively; $f$ is the friction coefficient, and $\rho_d$ and $u_d$ are depth-averaged density and depth-averaged mean velocity, respectively. The mean is considered over a sufficient time to average out the turbulent fluctuations and keep the tidal variation. Rewriting gives the definitions of the drag coefficient and friction coefficient:

$$C_{D(z)} = \left(\frac{u_*}{u_z}\right)^2 \tag{3.3}$$

or

$$\frac{f}{8} = \left(\frac{u_*}{u_d}\right)^2 \tag{3.4}$$

where the density differences are neglected: $\rho_b \approx \rho_{(z)} \approx \rho_d$. With SSC < 80 kg/m$^3$, neglecting the difference in density leads to a slight bias of <5% in the estimates of $C_{D(z)}$ or $f$. The friction coefficient ($f$) relates to the Chézy bed friction coefficient ($C$ in m$^{1/2}$/s), Manning coefficient ($n$) and water depth $H$ as $\frac{8}{f} = \frac{C^2}{g} = \frac{H^{\frac{1}{3}}}{gn^2}$ (Chow, 1959).

Therefore, quantifying the drag and friction coefficient requires the quantification of mean flow velocities and the determination of the shear velocity. The near-bed velocity ($u_z$) and depth-averaged mean velocity ($u_d$) were directly measured by ADV and ADCP. The shear velocity ($u_*$) could be obtained via Equations 3.1 and 3.2 and is referred to as the covariant method:

$$u_* = \sqrt{-\overline{u'w'}} \tag{3.5}$$

However, this method is sensitive to sensor misalignment with the local streamlines (Stapleton and Huntley, 1995; Wolf, 1999; Kim et al., 2000) and density stratification (Friedrichs and Wright, 1997). A method that is less sensitive to the sensor

misalignment is the TKE method (Soulsby, 1983; Stapleton and Huntley, 1995; Kim et al., 2000), defined by

$$\tau = \rho_b u_*^2 = C_1 \rho_b TKE \tag{3.6}$$

with

$$TKE = \frac{1}{2}\left(\overline{u'^2} + \overline{v'^2} + \overline{w'^2}\right) \tag{3.7}$$

where $u'$, $v'$ and $w'$ are streamwise, transverse and vertical velocity fluctuations, respectively; the overbars indicate time-averaging over each burst period. $C_1$ is a proportionality constant. This constant ranges from 0.18 to 0.21, as derived in estuarine systems (Soulsby, 1983; Kim et al., 2000). Vertical density gradients could introduce deviations. As no specific literature is available for modifying this coefficient for flows with density gradients, we used an averaged value (~0.20) in this study. Note that the value of $C_1$ does not change the estimation of relative reduction in $C_{D(z)}$ and $f$ shown in Figure 3-8.



We furthermore note that the friction and drag coefficients now represent the relation between the mean flow and the turbulent fluctuations. Both methods have their disadvantages: the COV method suffers from sensor misalignment, and the TKE-method from the definition of $C_1$. By using the two methods, we obtained reliable and reasonable estimates of $u_*$. The analysis of turbulent velocity was systematically conducted by the three-stage-post-processing method (Chanson et al., 2008). Note that only ADV data with a high signal-to-noise ratio (>5 dB) and correlation (>70%) were used in this study.

### 3.3.4. Eddy viscosity and diffusivity

The effect of suspended sediment on turbulent mixing can be evaluated by calculating the eddy viscosity ($\nu_t$) and diffusivity ($k_t$). Eddy viscosity is a function of the internal stress and the vertical velocity gradient (Lu and Lueck, 1999):

$$\nu_t = -\frac{\overline{u'w'}\frac{\partial u}{\partial z} + \overline{v'w'}\frac{\partial v}{\partial z}}{\left(\frac{\partial u}{\partial z}\right)^2 + \left(\frac{\partial v}{\partial z}\right)^2} \tag{3.8}$$

Since the internal stress was obtained by the ADV, direct estimates of eddy viscosity by Equation 3.8 were only available at 0.35 mab. To access the eddy viscosity for the entire water column, we employed the model proposed by Munk and Anderson (1948):

$$\nu_t = \kappa u_* z \left(1 - \frac{z}{H}\right)(1 + 10Ri)^{-\frac{1}{2}} \tag{3.9}$$

where $H$ is the water depth; $Ri$ is the gradient Richardson number defined as

$$Ri = -\frac{g}{\rho}\frac{\frac{\partial \rho}{\partial z}}{\left(\frac{\partial u}{\partial z}\right)^2+\left(\frac{\partial v}{\partial z}\right)^2} \tag{3.10}$$

in which $\rho$ is the density of sediment-laden flow accounting for the effect of temperature, salinity and suspended sediment. This model was validated against the estimates from Equation 3.8 before in-depth analyses.

The turbulent Prandtl–Schmidt number ($Pr_t$) relates eddy viscosity ($\nu_t$) to eddy diffusivity ($k_t$), as $k_t = \nu_t/Pr_t$. Since the performance of the standard turbulence model is unsatisfactory in the simulation of sediment diffusion in stratified flow, researchers proposed various parameterisations between $Pr_t$ and $Ri$. Wan and Wang (2017) compared these models and recommended the one proposed by Karimpour and Venayagamoorthy (2014). This model provides reliable estimates by taking the effect of buoyancy and wall boundary into account.



$$Pr_t = \left(1-\frac{z}{H}\right)\frac{Ri}{R_f} + \left(1-\frac{z}{H}\right)Pr_{td0} + Pr_{t0} \tag{3.11}$$

where $Pr_{td0}$ is the difference between the neutral turbulent Prandtl–Schmidt number at the wall ($Pr_{tw0} \approx 1.1$) and the neutral turbulent Prandtl–Schmidt number for a homogeneous shear flow ($Pr_{t0} = 0.7$); $R_f$ is the flux Richardson number given by $R_f = 0.25[1-\exp(-7.5Ri)]$.

### 3.3.5. Erosion and deposition

The erosion from the bed to the CBS layer can be determined as follows (Mehta, 1988):

$$E_1 = \begin{cases} M\left(\frac{\tau_b}{\tau_{ce}}-1\right) & (\tau_b > \tau_{ce}) \\ 0 & (\tau_b \le \tau_{ce}) \end{cases} \tag{3.12}$$

where $M$ is the bulk erosion coefficient; $\tau_{ce}$ is the critical shear stress for erosion, with a typical value of 0.2 N/m$^2$ in the North Passage (Ge et al., 2015). For simplicity, it is assumed that $M$ and $\tau_{ce}$ are uniform over the depth of the sediment on the river bed (i.e., excluding consolidation). Making this assumption has no consequence on our conclusion.

The settling from the CBS to the lower layer can be calculated by

$$D_1 = \omega C_b \tag{3.13}$$

in which $C_b$ is the near-bed sediment concentration of the CBS; $\omega$ is the effective settling velocity, accounting for hindered settling by (Dankers and Winterwerp, 2007)

$$\omega = \omega_0 \frac{(1-\phi)^2(1-\phi_p)}{1+2.5\phi} \tag{3.14}$$

where $\phi_p = C/\rho_s$ is the volumetric concentration of primary particles; $\phi = C/C_{gel}$ the relative volumetric concentration. Since near-bed sediment in the North Passage is fine material with a median diameter of ~12 μm (Lin et al., 2020), the gelling concentration ($C_{gel}$) is set to be 80 kg/m$^3$ in this study, as observed by Dankers and Winterwerp (2007) in their settling experiments for fine sediment. A sensitivity analysis of the gelling concentration is shown in the Appendix (Figure 3-A1). When SSC reaches the gelling point, flocs start forming a space-filling network structure on the bed, and the effective settling velocity is zero. In the North Passage, the sediment density ($\rho_s$) is 2570 kg/m$^3$ (Guo et al., 2017). The settling velocity of flocs in almost clear water ($\omega_0$) has an average of 0.1 mm/s (Wan et al., 2015). Observations show that the bed level near CS4 increases ~5 cm after a 3.5-hour CBS event (Xu, 2009). To match this magnitude of bed level variation, $M$ is set to 0.001 kg/m$^2$/s in this study.



## 3.4. Results

### 3.4.1. Regime shift

The evolution in bathymetry is presented in Figure 3-2a, showing a profound deepening between 1997 and 2010. The water depth increased from ~6 m to ~12 m. After the Deepwater Navigational Channel Project (2010), the depth is maintained by frequent dredging.

The SSC profiles near station CS4 notably changed from 1988 to 2015 (Figure 3-2b). Tidally averaged sediment concentrations in the near-surface water column remained stable at a level of 0.2-0.3 kg/m$^3$ (0.95$H$) and 0.3-0.6 kg/m$^3$ (0.8$H$). In the mid-lower water column, concentrations decreased from 1.2 to 0.3 kg/m$^3$ (0.6$H$), from 1.7 to 0.4 kg/m$^3$ (0.4$H$) and from 2.1 to 0.9 kg/m$^3$ (0.2$H$). Observations of near-bed (0.95$H$) SSC, however, show a slight increase from 3.0 to 3.6 kg/m$^3$. Although this increase is small, the positive standard deviation significantly enlarged. Enlarged standard deviations in 2014 and 2015 indicate near-bed high concentrations (up to 40 kg/m$^3$) during the tidal cycle. It suggests that the estuary undergoes a regime shift in SSC profiles as expected, with decreasing SSC in the mid-lower water column and frequent high SSC in the bottom layer.

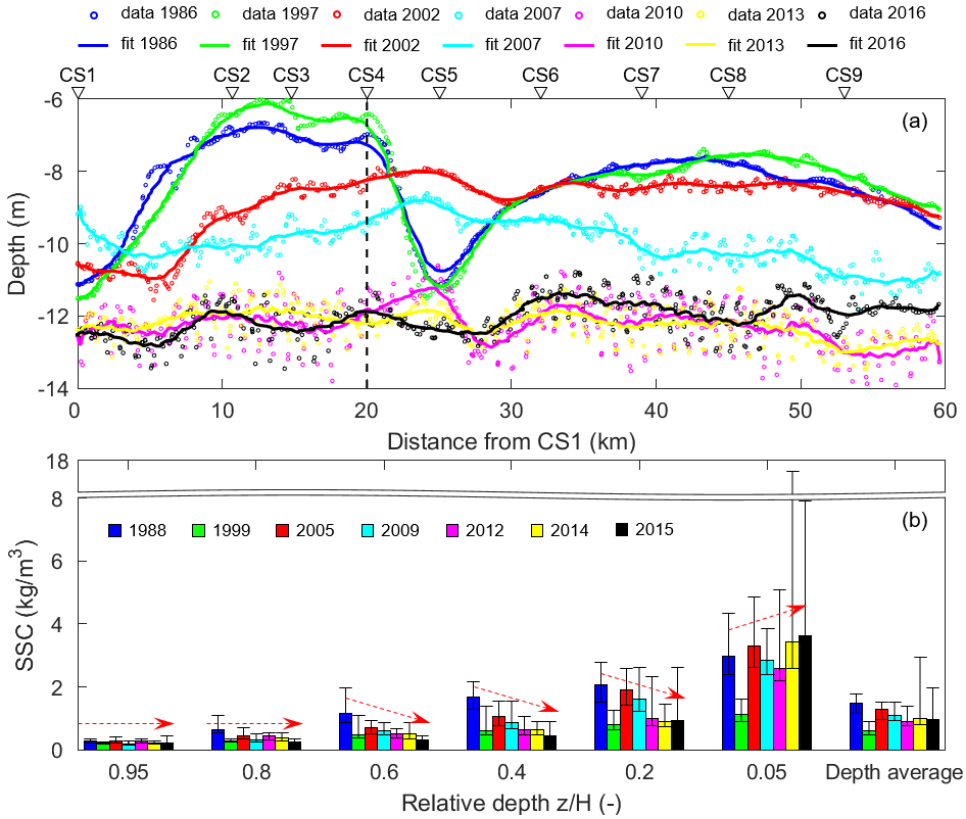


*Figure 3-2: (a) Measured channel depth from 1986 to 2016 with smooth fits. The dashed line indicates the site where historical suspended sediment concentrations (SSC) were collected. (b) Tidally averaged SSC in six relative-depth layers, i.e., z/H = 0.05 (near the bed), 0.2, 0.4, 0.6, 0.8 and 0.95 (near the surface), where H is the water depth, and z denotes the height above the bed. Error bars denote standard deviations, and red arrows show the trend in SSC.*

### 3.4.2. Mobile CBS pool

Observations in 2012 show a mobile CBS pool in the mid-lower reaches of the North Passage (Figure 3-3). At low-water slack, the CBS pool was in the lower reaches (between stations CS5 and CS8), with a length of ~20 km and a thickness of <3 m. The pool moved upstream during flood tides. At maximum flood, the pool covered the area between stations CS4 and CS6. The thickness increased and exceeded 6 m, while the length reduced to ~10 km. At high-water slack, the CBS pool reached CS3, with length and thickness similar to those at low-water slack. On the early ebb, the position of the CBS pool front was fixed (at station CS3), although along-channel flows had turned seaward. The tail of the pool, however, retreated directly from

high-water slack. As a result, the length of the CBS pool expanded and reached the maximum (~30 km) at the maximum ebb, covering stations from CS3 to CS8. The thickness was less than 3 m, with the maximum at station CS5 (~4 m). The CBS pool continued to retreat during the late ebb and back to its initial position at low-water slack. Over a tidal cycle during spring tides, the CBS pool had a mean length of ~20 km and a mean thickness of ~4 m. At station CS4, the CBS appeared from the maximum flood to the maximum ebb (Figure 3-4b).

Cross-channel SSC distributions are presented in Figures 3-3e-h and 3-4f, showing a limited width of the CBS pool (<1 km). The CBS pool mainly exists in the Deepwater Navigational Channel and could not reach the shallow shoals protected by the groins. The SSC was typically higher in the main channel (up to 68 kg/m$^3$) than in the flanks (<10 kg/m$^3$). Particularly when the CBS appeared, the SSC in the main channel was up to 50 kg/m$^3$, while those on both flanks were ~3.0 kg/m$^3$. Significant lateral SSC gradients were therefore produced. Such considerable gradients, combined with even small lateral flows (averaged 0.1 m/s), could contribute to the SSC variations on both flanks. From the late flood to the early ebb, southward lateral flows coincided with a sharp SSC increase on the south side and a reduction on the north side of the channel (Figure 3-4h). After that, the opposite was true until the maximum ebb. Lateral advection seems to play a vital role in local SSC variations. The CBS events on both sides of the channel may result from the cross-channel movements of the CBS pool.



Figure 3-5 shows the time series of velocity, salinity and SSC at station CS4T in 2014. Near-surface and near-bed water columns exhibited different intra-tidal variation patterns of SSC. Near the surface, the SSC reached the minimum at slack waters and the peak value at the maximum flood/ebb. It suggests that near-surface SSC was mainly controlled by resuspension and deposition. However, in the bottom layer, high SSC (up to 63 kg/m$^3$) appeared on the early ebb instead of at the maximum flood/ebb. The CBS was observed only in the lowest 1 m from high-water slack to the maximum ebb, with a lifetime of ~3.5 hours (Figure 3-5e). Note the low SSC in the upper water column before CBS events. There was insufficient sediment available for settling to support the near-bed high SSC. Therefore, the CBS at station CS4T was not the result of settling from the upper water column.

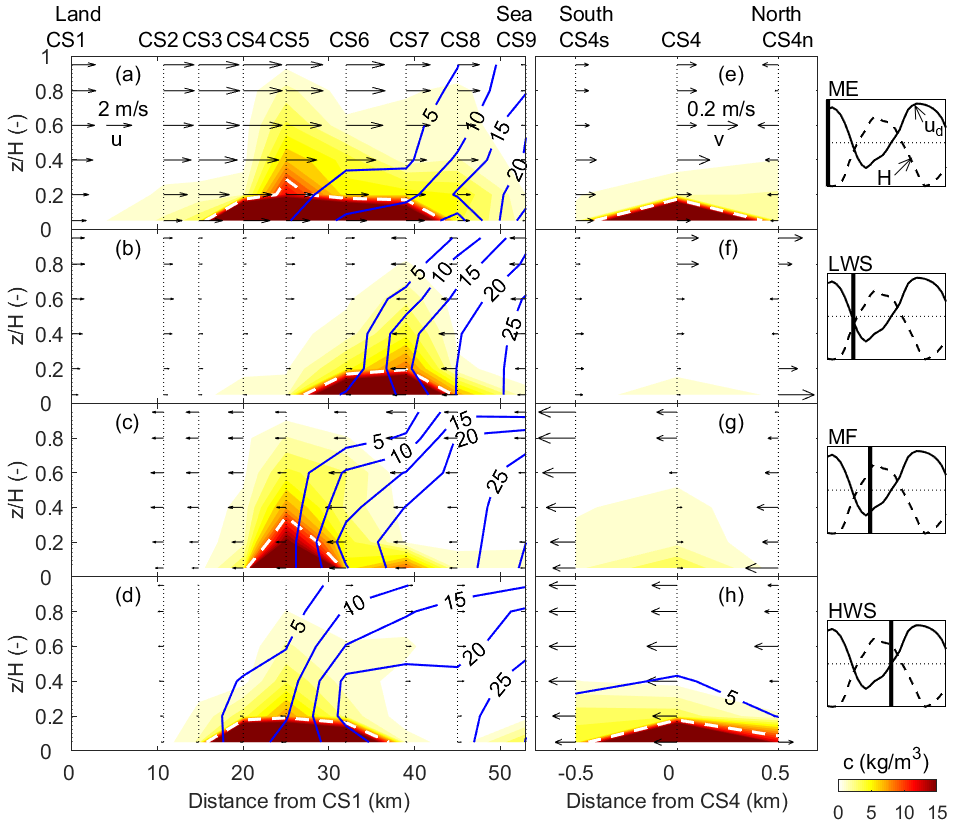


*Figure 3-3: Along-channel (left panels) and cross-channel (middle panels) distributions of velocity (arrows), salinity (contour lines) and suspended sediment concentration (SSC; filled contours) at the time of maximum ebb (ME), low-water slack (LWS), maximum flood (MF) and high-water slack (HWS) during a spring tide (05:00 to 18:00, 17 August 2012). The right panels show the depth-averaged velocity ($u_d$) and water depth (H) at station CS4. The white dashed lines denote the contour line of SSC of 10 kg/m$^3$, showing the top of the concentrated benthic suspension. An orthogonal coordinate according to channel direction is used for velocity decomposition. Positive along-channel velocities, u, at stations CS1, CS2, CS3, CS4, CS5, CS6, CS7, CS8 and CS9 indicate the directions of 115°, 101°, 101°, 101°, 113°, 125°, 125°, 125° and 90° from the north, respectively. At each station, positive cross-channel velocity, v, is perpendicular to u, pointing from the Jiuduan Shoal to the Hengsha Shoal (nearly northward).*

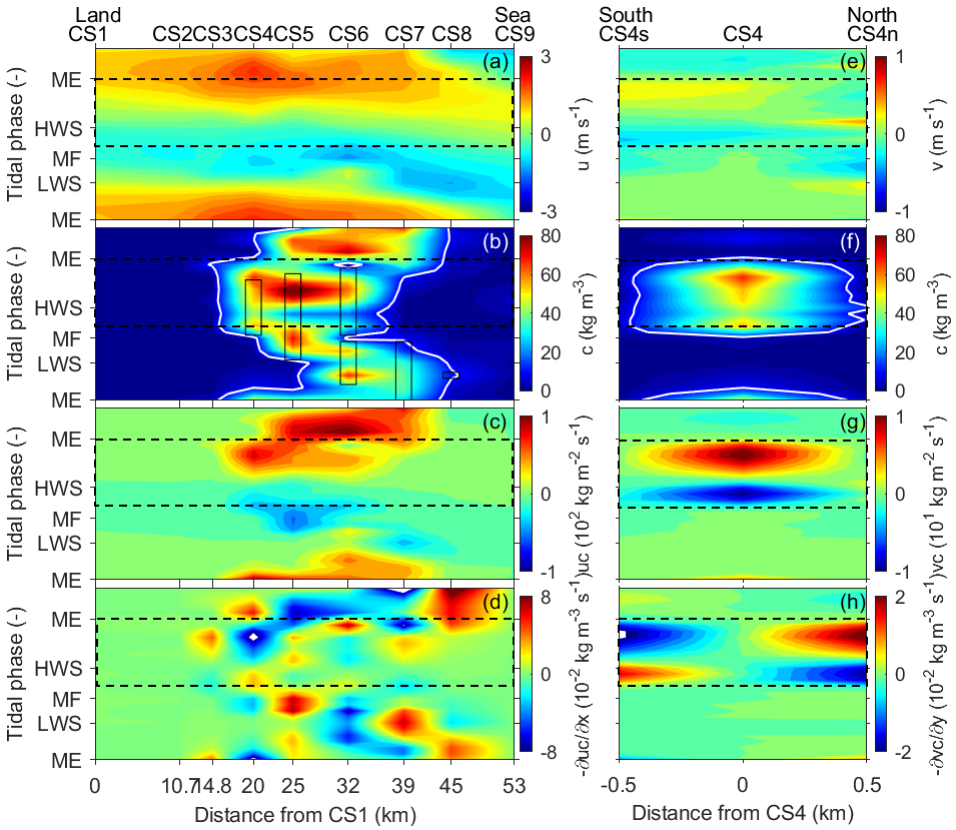


*Figure 3-4: Along-channel (left panels) and cross-channel (right panels) distributions of (a) (e) velocity, (b) (f) suspended sediment concentration (SSC), (c) (g) advective sediment flux and (d) (h) minus the gradient of advective flux in the bottom layer during the spring tide in 2012. Along-channel and cross-channel velocities are represented by u and v, respectively. The dashed boxes indicate the period when concentrated benthic suspensions (CBS) occurred at station CS4. The white lines in panels (b) and (f) show the contour line of SSC of 10 kg/m$^3$. The boxes in panel (b) indicate the period when the net deposition from the CBS to the bed occurred at each station.*

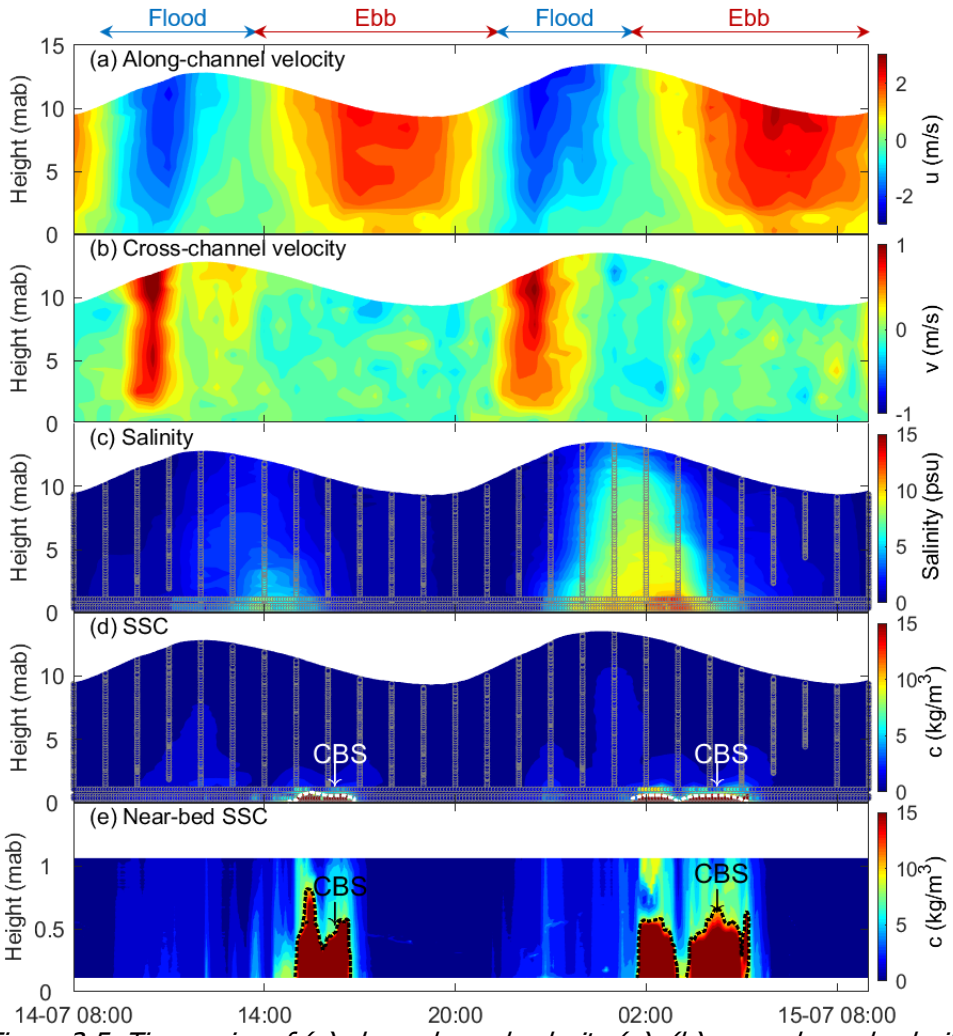


*Figure 3-5: Time series of (a) along-channel velocity (u), (b) cross-channel velocity (v), (c) salinity, (d) suspended sediment concentration (SSC) and (e) near-bed SSC at CS4T during spring tide. Coloured circles in panels (c) and (d) indicate the valid data collected by instruments. An orthogonal coordinate according to channel direction is used for velocity decomposition. Positive u and v denote the direction of 101° and 11° from the north, respectively. The dashed lines show the contour line of SSC of 10 kg/m$^3$, and the CBS represents concentrated benthic suspensions with SSC of 10-80 kg/m$^3$. The abbreviation 'mab' denotes meters above the bed.*

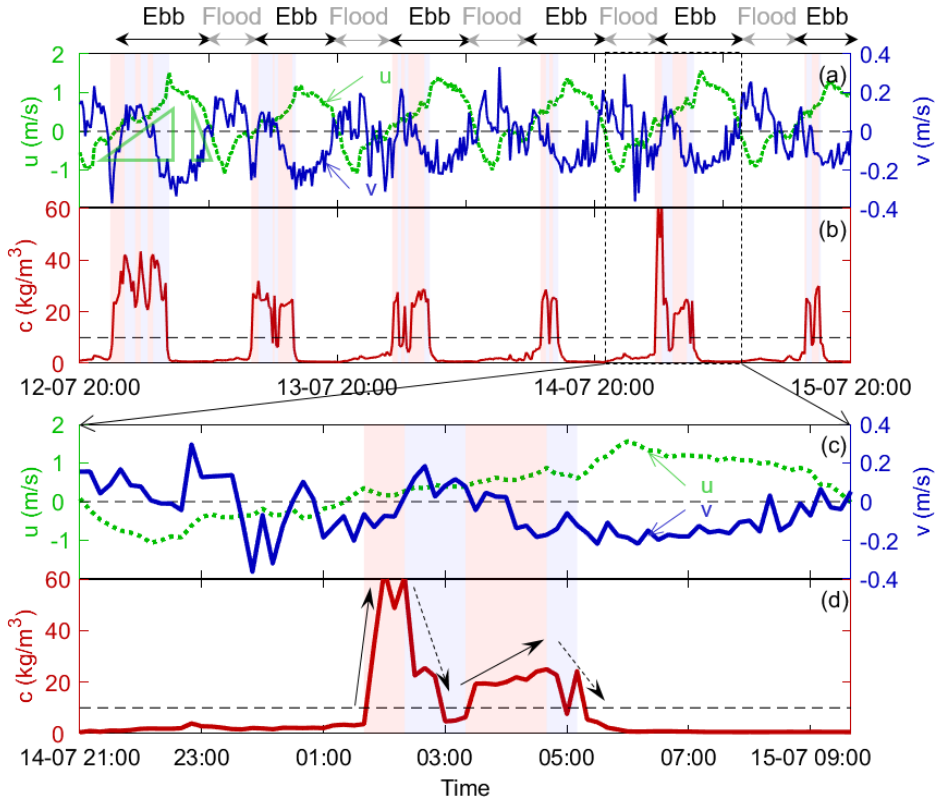


*Figure 3-6: Time series of (a) along-channel (u) and cross-channel (v) velocity and (b) suspended sediment concentration at 0.35 m above the bed. Panels (c) and (d) show the zoom-in series over a spring tidal cycle from 21:00, 14 July to 09:00, 15 July 2014. Positive u indicates the ebb direction (101°from the north), and positive v represents the nearly northward cross-channel flows (11° from the north). The triangles (slopes) in panel (a) indicate slack-water asymmetry. At high-water slack, a lower flow acceleration occurs than at low-water slack.*

Near-bed (0.35 mab) variations in SSC and currents are shown in Figure 3-6. During the CBS event from 1:40 am to 5:20 am on 15 July, the SSC rapidly increased to the maximum (63 kg/m$^3$) in the first 40 min and decreased for the next 60 min. After reaching the minimum (~5.0 kg/m$^3$), the SSC increased again (to 25 kg/m$^3$) and persisted for 80 min, followed by a 30-min reduction. A similar pattern of SSC variation was captured in other CBS events. There were southward lateral flows (from the main channel to the Jiuduan Shoal) during increasing SSC and northward flows during the reduction (Figure 3-6c and d). It suggests that local SSC variation at CS4T is mainly driven by cross-channel flows, as observed in 2012 (Figure 3-4h). Southward flows drive the movements of the CBS pool from the main channel

towards the Jiuduan Shoal, leading to the rapid SSC increase at station CS4T, while the return flows cause decreasing SSC. However, the SSC reduction at the end of the CBS event is an exception. This reduction could be attributed to the seaward movement of the CBS pool. During this period, the CBS pool was moving seaward. When the pool moved further downstream, it no longer covered station CS4T. As a result, the SSC at CS4T was relatively low during the late ebb.

### 3.4.3. Drag reduction

The drag reduction can be quantified based on turbulent velocities measured at CS4T in 2014. Before the quantification, we compared the estimates of friction velocity ($u_*$) given by the TKE and COV methods. The results show that these two methods give very similar estimates (Figure 3-7a), indicating that the sensor misalignment is limited and that the definition of the coefficient $C_1 = 0.20$, as defined for uniform channel flow, is also reasonable in this flow. A clear correlation between the near-bed velocities and the shear velocities is found. The correlation with the depth-averaged velocity is weaker, especially during the late flood and early ebb. The ratio between the squared friction velocity and the squared depth-averaged velocity results in the friction coefficient ($f$), and the ratio between the squared friction velocity and the squared near-bed (0.35 mab) velocity ($u_b$) provides the drag coefficient $C_{D(z=0.35)}$.

The friction coefficient and drag coefficient show a similar intra-tidal variation, with high values at slack waters and low values in the presence of CBS (Figure 3-7c). The high values during the ebb-flood transition may result from the shear stress induced by secondary flow at low flow velocities (Wu et al., 2011). In order to avoid the contamination of this nonlinear effect, the data at low flow velocity (<0.5 m/s) was removed in the analyses of drag reduction by suspended sediment.

During late ebb, when CBS and stratification were absent, $f$ and $C_{D(z=0.35)}$ had values of $3.1\times10^{-4}$ and $7.0\times10^{-4}$, respectively. In the presence of CBS, $f$ decreased to $0.9\times10^{-4}$ and $C_{D(z=0.35)}$ declined to $2.5\times10^{-4}$. It suggests that CBS causes a reduction of 60-80% in bed shear stress. The drag reduction reduces the erosion (or entrainment) from the consolidated bed (or fluid mud layer) with the assumed critical stress for erosion.

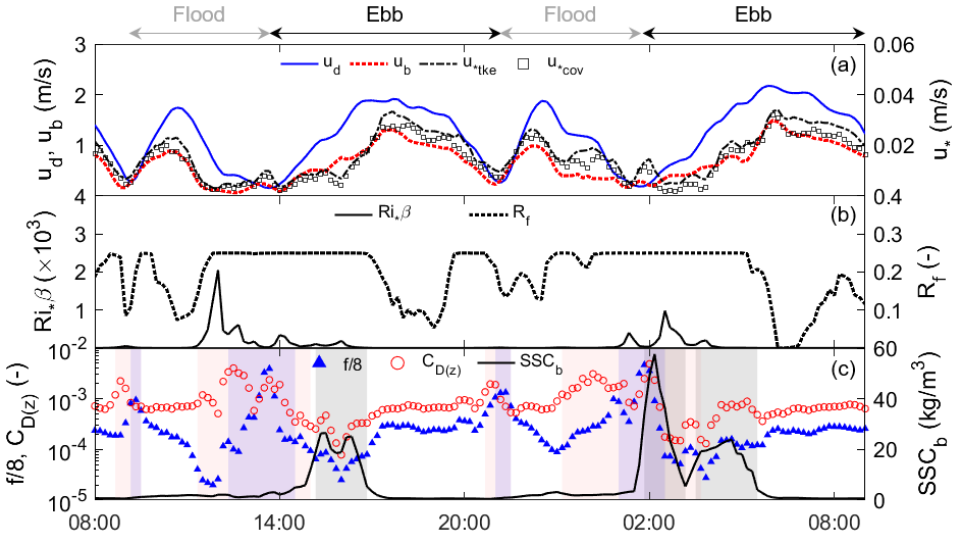


*Figure 3-7: Time series of (a) depth-averaged velocity ($u_d$), near-bed velocity ($u_b$) and friction velocity given by the TKE method ($u_{*tke}$) and COV method ($u_{*cov}$), (b) near-bed flux Richardson number ($R_f$) and the term $Ri_*\beta$ where $Ri_*$ is bulk Richardson number and $\beta$ is Rouse number, and (c) near-bed suspended sediment concentration ($SSC_b$), friction coefficient (f) and drag coefficient ($C_{D(z)}$). The red and blue shadings indicate periods when $u_b$ and $u_d$ are less than 0.5 m/s, respectively. The presence of concentrated benthic suspensions corresponds to grey shading.*

Both normalised friction coefficient ($f/f_0$) and drag coefficient ($C_{D(z)}/C_{D(z)0}$) show a sharp reduction with increasing SSC (Figure 3-8). Within SSC of 0.5-10 kg/m$^3$, the friction coefficient linearly decreases; in 10-40 kg/m$^3$, $f$ is relatively constant and minimum (Figure 3-8a). The reduction in drag coefficient appears to fall into three ranges: (1) 0.5-3, (2) 3-10 and (3) 10-30 kg/m$^3$ (Figure 3-8b). In the first range, the drag coefficient is constant, implying no significant effect of the sediment. An almost linearly decreasing $C_{D(z)}$ appears in range 2. In range 3, the drag coefficient is approximately constant. The maximum reduction in $f$ (~80%) and $C_{D(z)}$ (~60%) were both observed in the presence of CBS. These results suggest that the drag reduction is limited and does not reduce to (almost) zero. Thompson et al. (2006) suggest an increase in drag for very high concentrations. Such concentrations are, however, out of the scope of the Changjiang Estuary.

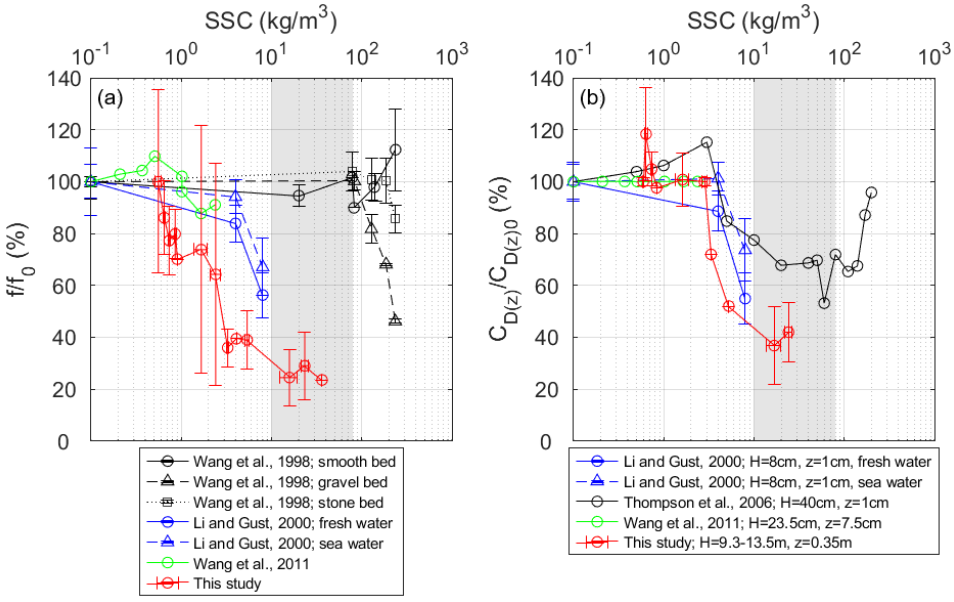


*Figure 3-8: Normalized (a) friction coefficient ($f/f_0$) and (b) drag coefficient ($C_{D(z)}/C_{D(z)0}$) versus suspended sediment concentration (SSC). The symbols $f_0$ and $C_{D(z)0}$ denote the friction coefficient and drag coefficient within the lowest SSC. Scatter points represent data from laboratory experiments reported in the literature and field observations (this study). The SSC range of concentrated benthic suspension corresponds to grey shading. Laboratory experiment data are available from Wang et al. (1998), Li and Gust (2000), Thompson et al. (2006) and Wang et al. (2011).*

### 3.4.4. Reduced eddy diffusivity

The eddy viscosity model proposed by Munk and Anderson (1948) was validated by field observations (Figure 3-9a). The correlation coefficient between observed and modelled eddy viscosity is high (>0.65), indicating that the model can simulate eddy diffusivity properly. Based on validated models, we obtained profiles of eddy diffusivity in the water column.

The time series of eddy diffusivity shows a profound reduction in the presence of CBS on the early ebb (Figure 3-9c). Although profiles of velocity and salinity were similar, eddy diffusivity was significantly lower with than without CBS, particularly near the bed (Figure 3-9d and e). Two mechanisms are responsible for this reduction. First, the drag reduction by CBS returns a lower friction velocity, and thus eddy viscosity reduces. Second, SSC gradients in CBS enhance near-bed stratification, reducing eddy diffusivity through buoyancy destruction (Figure 3-9b).

As a result, vertical sediment diffusion from CBS to the upper water column is suppressed, which provides favourable situations for sediment trapping near the bed. Accumulated sediment, in turn, enhances the stability of CBS. These results show indications of the positive feedback mechanisms controlling the formation and maintenance of CBS (Winterwerp, 2002; Ge et al., 2018).

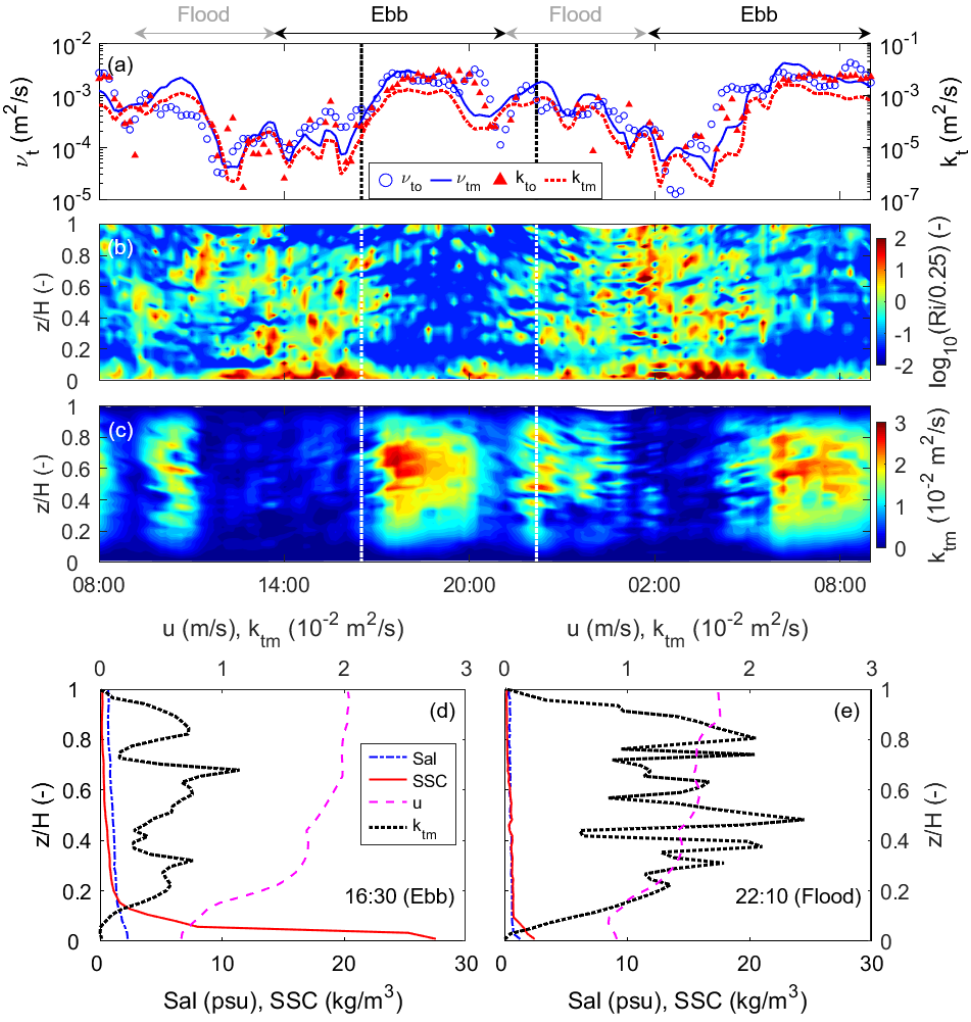


*Figure 3-9: Time series of (a) observed (scatters) and modelled (lines) near-bed (0.35 metre above the bed) eddy viscosity ($\nu_t$) and eddy diffusivity ($k_t$), (b) Richardson number and (c) modelled eddy diffusivity. Typical profiles of velocity, salinity, suspended sediment concentration and eddy diffusivity on the early ebb (d) and early flood (e) show a reduction in eddy diffusivity in the presence of concentrated benthic suspension.*

### 3.4.5. Tidal asymmetry

The North Passage is ebb-dominant. During the observation in 2012, the depth-averaged velocity of ebb tides was up to 1.8 m/s, while flood tides were <1.2 m/s, indicating the asymmetry in peak velocity. During ebb tides, the maximum velocity occurred near the water surface and exceeded 3.0 m/s. The duration of the ebb tide was 7.9 hours, longer than that of the flood tide (4.5 hours). These differences between flood and ebb tides decreased in the bottom layer.

At low-water slack, the flow acceleration is ~2 times higher than at high-water slack (Figure 3-10a), indicating slack-water asymmetry. For a given critical shear stress for erosion ($\tau_{ce}$) and friction coefficient ($f$), the lower acceleration implies a longer slack (when $\tau_b < \tau_{ce}$) after high water than after low water. Thus, sediment has more time to settle at high-water slack. It suggests that much more intensive deposition occurs at high-water slack than at low-water slack. This asymmetry, combined with the movements of the CBS pool (Section 3.4.2), sheds light on the sediment trapping and channel siltation in the North Passage.



The maximum cross-channel velocity ($v$) was southward and up to 0.4 m/s (Figure 3-2). In the bottom layer, the mean magnitude of southward $v$ (0.16 m/s) was slightly greater than that of the northward (0.12 m/s). Southward $v$ occurred for 60% of the time, with the remaining 40% northward. These results indicate the lateral flow asymmetry in velocity. Strong southward flows persisted from the late flood to the early ebb. As a result, the CBS pool tends to be on the south flank of the channel when reaching the upstream limit, particularly when the net deposition of sediment occurs from the CBS to the bed (Figure 3-10b). The asymmetries in slack waters and lateral flows were confirmed during the observation in 2014 (Figures 3-5 and 3-6).

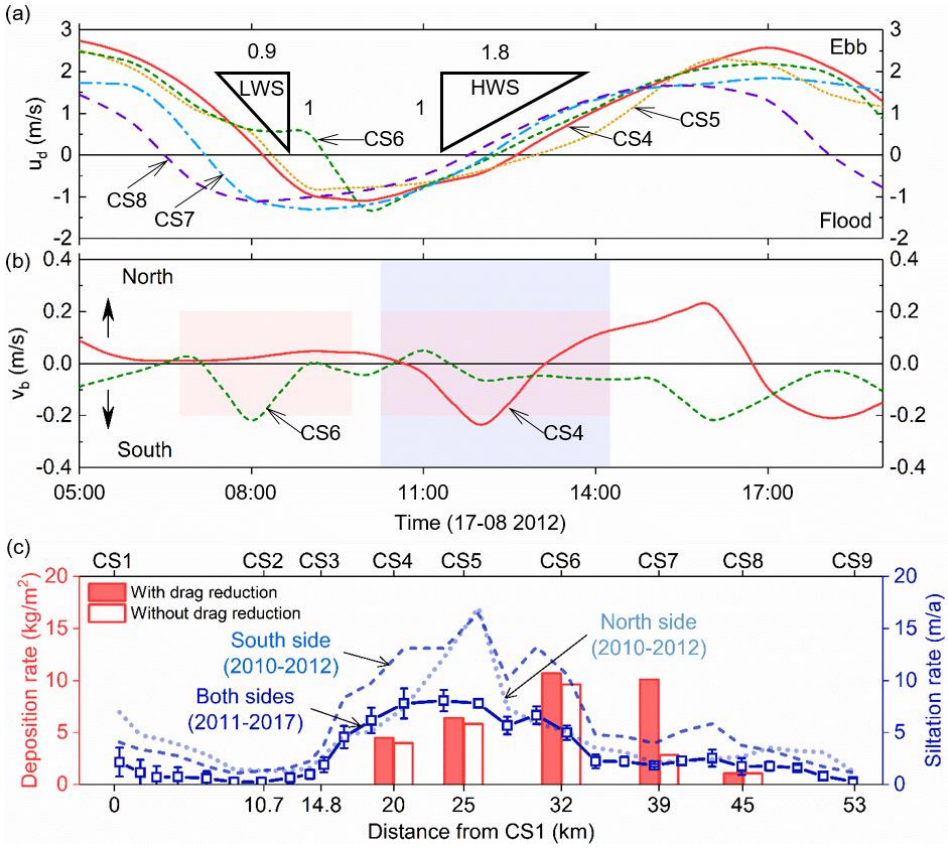


*Figure 3-10: (a) Time series of depth-averaged velocity ($u_d$) at stations CS4, CS5, CS6, CS7 and CS8. Positive $u_d$ indicates the ebb flow along the channel. The triangles (slopes) show a lower flow acceleration at high-water slack (HWS) than at low-water slack (LWS), i.e. slack-water asymmetry. (b) Time series of near-bed cross-channel velocity ($v_b$) at stations CS4 (solid line) and CS6 (dashed line). Positive $v_b$ indicates the northward lateral flows from the main channel toward the Hengsha Shoal (Figure 3-1). The red and blue shadings indicate the periods when the net deposition of sediment occurred from concentrated benthic suspensions (CBS) to the bed at CS6 and CS4, respectively. (c) Along-channel distribution of yearly siltation rate (lines) in the Deepwater Navigational Channel (data from Liu et al., 2019) and the estimated net deposition rate of sediment from CBS (bars) over the spring tide on 17 August 2012. The filled bars indicate the net deposition rate accounting for CBS-induced drag reduction, while the empty bars do not consider drag reduction. Note that the siltation rate is the rate of bed level change, whereas the net deposition is the increase of sediment mass on the seabed. They relate to each other through a dry density of 1200 kg/m$^3$ for dredged sediment (Zhu et al., 2019).*

## 3.5. Discussion

### 3.5.1. Field observations vs laboratory experiments

Our filed observations show the response of friction coefficient ($f$) and drag coefficient ($C_{D(z=0.35)}$) to SSC (Figure 3-8). Both $f$ and $C_{D(z=0.35)}$ are relatively constant and minimum within a SSC range of 10-40 kg/m$^3$ where the CBS occurs, showing a reduction of 60-80% in drag. Within low SSC, $f$ and $C_{D(z=0.35)}$ exist different responses. The drag coefficient for near-bed velocity ($C_{D(z=0.35)}$) appears constant within the SSC of 0-3 kg/m$^3$ and linearly decreases in the range of 3-10 kg/m$^3$; whereas $f$, a friction coefficient for depth-averaged velocity, shows a linear decrease in the range of 0-10 kg/m$^3$. This difference is due to the height above the bed of the characteristic velocity. In low-concentration sediment-laden flows, near-bed velocity and friction velocity change almost synchronously with SSC, while the velocity in the upper water column lags. Therefore, the near-bed drag coefficient keeps constant in a certain range of SSC, while $f$ immediately decreases with increasing SSC.



Our results can be considered in line with the response of the drag coefficient to SSC observed by Thompson et al. (2006) from laboratory experiments (Figure 3-8b). However, our measurements do not reach the high concentrations observed by Thompson et al. (2006). They observed a constant and minimum drag coefficient in the SSC range of 20-120 kg/m$^3$, with a reduction of up to 50%. Our field observations, however, suggest a more significant drag reduction. The underestimated drag reduction in the lab could be attributed to severe scale effects in small-scale facilities (Winterwerp et al., 2009). In these facilities, the water depth is limited; hence turbulence and mixing are suppressed by the free water surface in addition to sediment concentration. As a result, sediment-induced buoyancy destruction will not be easily observed, and drag reduction will be underestimated in such small facilities.

In addition, Thompson et al. (2006) observed an increase in drag at higher SSC (> 120 kg/m$^3$). No fluid mud was observed from our measurements, so the increase in drag at higher SSC could not be confirmed directly by our observations. However, our measurements confirm the maximum drag reduction in a particular range of SSC, although the magnitude of reduction is different between in-lab and in-field measurements. The maximum drag reduction is reached due to the increasing relative importance of viscous stress at high SSC (Thompson et al., 2006). Therefore, a substantial decrease in drag for concentrations higher than ~10 kg/m3 is not expected in the Changjiang Estuary.

### 3.5.2. Verification of theoretical expressions for drag reduction

The friction/drag coefficient is a function of the (flux) Richardson number (Wang, 2002; Winterwerp et al., 2009). Based on the log-linear velocity profile, Winterwerp et al. (2009) derived a simple relation for the friction coefficient (Chézy coefficient in their study) as

$$\left(\frac{8}{f}\right)^{\frac{1}{2}} = \frac{u_d}{u_*} = \frac{C_{\text{eff}}}{g^{\frac{1}{2}}} = \frac{C_0}{g^{\frac{1}{2}}} + K_1 H Ri_* \beta \tag{3.15}$$

where $C_{\text{eff}}$ denotes the effective Chézy coefficient, $C_0$ the Chézy coefficient for neutral conditions, and empirical coefficient $K_1$ [1/m]. The bulk Richardson number $Ri_*$ and the Rouse number $\beta$ are defined as

$$Ri_* = \frac{(\rho - \rho_w) g H}{\rho u_*^2} \text{ and } \beta = \frac{Pr_t \omega}{\kappa u_*} \tag{3.16}$$

where $\rho_w$ is the density of water determined by the equation of state. The dimensionless parameter $C_0/g^{\frac{1}{2}}$ is ~25 in the Changjiang Estuary (Winterwerp et al., 2009).

The bottom drag coefficient in a sediment-laden bottom boundary layer can be given by (Wang, 2002)

$$C_{D(z)} = \left[\frac{1 + AR_f}{\kappa} \ln \frac{z}{z_0}\right]^{-2} \tag{3.17}$$

in which $z_0$ is the bottom roughness set equal to 0.1 mm for the bed sediment in the North Passage with a median grain size of 12 μm (Cheng, 2015; Lin et al., 2020). The effect of stratification is taken into account by a stability function $(1+AR_f)$, where $A$ is an empirical constant and $A$ = 5.5 for a partially stratified estuary (Wang, 2002).

Our observations could be used to verify these theoretical expressions (Figure 3-11). The expression by Winterwerp et al. (2009) returns overestimated $f$ at low Richardson number (low SSC) and underestimated $f$ at high Richardson number (high SSC). The drag reduction is thus underestimated at low SSC and overestimated at high SSC. The underestimation may be attributed to the fact that this expression does not account for the drag reduction caused by flocculation (Wang et al., 1998), bedforms (Winterwerp et al., 2009) and thickening of the viscous sub-layer (Li and Gust, 2000). The overestimation, however, may result from increasing viscous resistance at high SSC (Wang et al., 1998; Thompson et al., 2006). Our data show a power function relationship between the friction coefficient and the Richardson and Rouse Numbers. An empirical expression is obtained by fitting, as

$$\left(\frac{8}{f}\right)^{\frac{1}{2}} = \frac{C_0}{g^{\frac{1}{2}}} + \frac{H}{\lambda}(Ri_*\beta)^{0.16} \tag{3.18}$$

with a correlation coefficient ($R^2$) of 0.46 ($N$ = 120). The length scale $\lambda = 0.28$ m is empirically determined. No direct physical explanation was found for this length scale. Note that this empirical formula only applies to concentrations less than 40 kg/m$^3$ and that viscous resistance needs to be considered at higher concentrations.

The empirical coefficient $K_1$ in Equation 3.15 is determined by numerical experiments with the 1DV POINT MODEL (Winterwerp et al., 2009). Note the substantial difference between their model results and our observations. Their 1DV model is for steady and uniform flows, where turbulence is generated locally. Simulations are carried with increasing values for $Ri_*\beta$, until turbulence collapses completely (just before the fluid mud forms). The results used to determine $K_1$ are obtained when the model reaches an equilibrium. The turbulence did not completely collapse during our observations, although the turbulent kinetic energy reduced substantially to almost zero. The remaining turbulence could result from lag effects, for example, by the reversing tidal currents in the Changjiang Estuary. Furthermore, the observed turbulence was affected by advection in addition to local generation. These differences resulted in remaining turbulence and high values for $Ri_*$ in the field, compared to the 1DV model where turbulence collapsed.

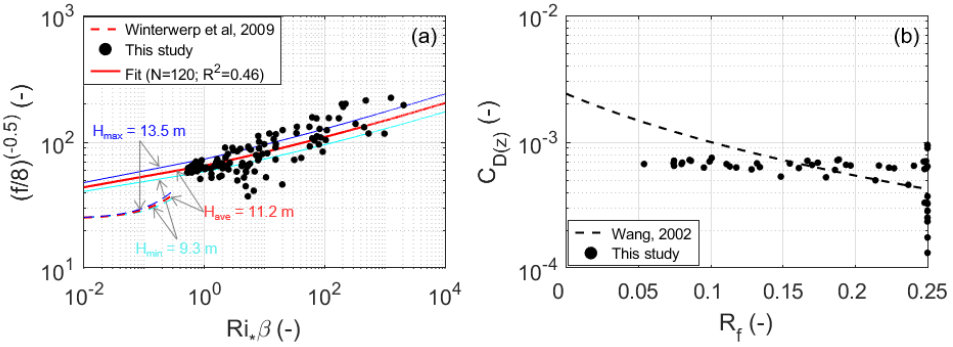


*Figure 3-11: (a) Comparison between observed and modelled friction coefficient (f). The horizontal axis is the term $Ri_*\beta$ where $Ri_*$ is the bulk Richardson number, and $\beta$ is the Rouse number. The friction coefficient is also a function of water depth. The minimum, maximum and averaged depth during the observation in the Changjiang Estuary are shown as $H_{min}$, $H_{max}$ and $H_{ave}$, respectively. The function of Winterwerp et al. (2009) is plotted only for $Ri_*\beta$ <0.3. (b) Comparison between observed and modelled drag coefficient ($C_{D(z)}$). The horizontal axis is the near-bed flux Richardson number ($R_f$).*

The expression by Wang (2002) assumes that $R_f$ asymptotes to a value of 0.25 around $Ri \approx 1$ (Mellor and Yamada, 1974; Wang, 2002; Karimpour and Venayagamoorthy, 2014). It means that the turbulence is entirely suppressed by the stratification when $Ri > 1$, returning the minimum bottom drag coefficient. Thus, this expression mainly estimates drag reduction when $Ri < 1$. Our observations, however, show that the drag coefficient is relatively stable at low Richardson numbers and that a notable drag reduction occurs at higher Richardson numbers ($Ri > 1$) with high SSC (Figure 3-11b). Therefore, Equation 3.17 underestimates the drag reduction at high sediment concentration, giving an overestimated drag coefficient.

### 3.5.3. Transition in SSC profiles

Both field observations (Figure 3-8) and laboratory experiments (Thompson et al., 2006) show that the maximum drag reduction occurs in the presence of CBS. This reduction (up to 60-80%) results from turbulence damping. Figure 3-12 shows a decrease in velocity fluctuations and TKE in the presence of CBS when compared to values without CBS. Eddy diffusivity, therefore, decreases because of (1) reduced friction velocity (i.e., reduced turbulence production from the bed) and (2) increased buoyancy destruction. As a result, sediment entrainment reduces significantly.



On the one hand, reduced entrainment from CBS to upper dilute suspensions decreases the SSC in the upper water column. On the other hand, reduced entrainment favours sediment trapping in CBS and lower fluid mud layers. With sediment accumulation, near-bed SSC increases and hindered settling becomes important. Hindered settling, in turn, supports high SSC by reducing settling from CBS to a lower fluid mud layer or the consolidated bed (Dijkstra et al., 2018).

The above analyses suggest a transition of SSC profiles for the regime shift. Our observations provide evidence for the positive feedback loop proposed by Winterwerp and Wang (2013). After the deepening, a mobile CBS pool develops in the North Passage, leading to a drag reduction of 60-80%. Reduced hydraulic drag strengthens tidal deformation, which may increase sediment import (Xing, 2016). Regarding vertical processes, the erosion of the bed is similar to that under low-turbid conditions, as the drag reduction by turbulence damping is counterbalanced by increasing viscosity in the presence of fluid mud. However, the entrainment of fluid mud and CBS significantly decreases due to the reduction in eddy viscosity by (1) reduced initial turbulence production from the bed and (2) increased buoyancy destruction. Besides, hindered settling supports the stability of CBS and fluid mud. As a result, CBS and fluid mud layers develop near the bed, whereas concentrations in the upper water column decrease. A more comprehensive feedback mechanism is sketched in Figure 3-13, depicting the transition in SSC profiles during the regime

shift to the hyper-turbid state. Such a transition was observed in the North Passage (Figure 3-2). Although the decrease in sediment supply from the Changjiang River could also decrease the SSC in the water column (Guo et al., 2019), the frequent high concentrations in the bottom layer confirm this transition in SSC profiles.

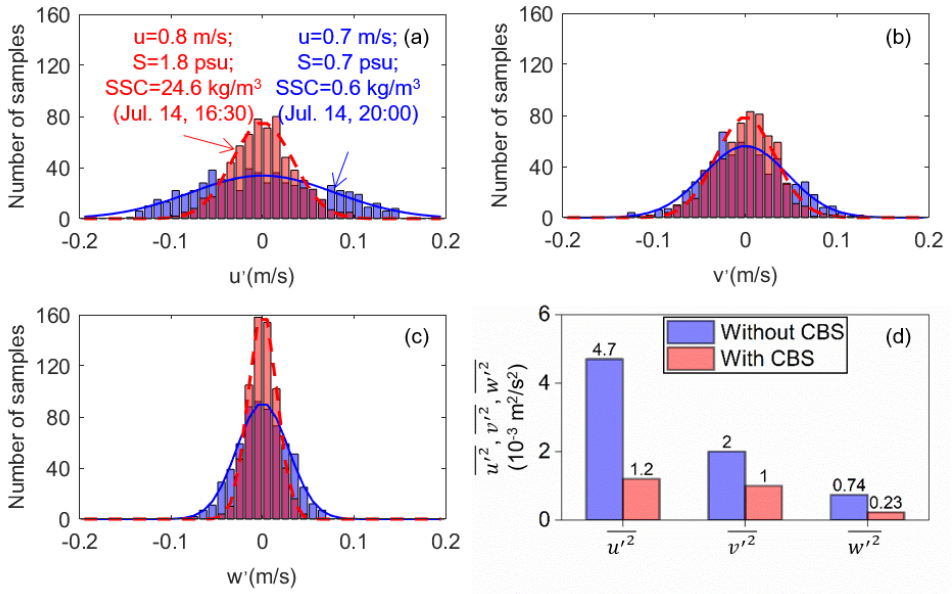


*Figure 3-12: Typical distributions of (a) streamwise (u′), (b) transverse (v′) and (c) vertical (w′) fluctuations of velocity and their Gaussian fits (curves) with (red) and without (blue) the presence of concentrated benthic suspension. (d) Comparison between the burst-averaged fluctuations under these two conditions. Data were collected at CS4T during the spring tide on 14 July 2014. PSU: practical salinity units.*

### 3.5.4. Implications for sediment transport

After the deepening, a mobile CBS pool exists in the North Passage. Its length and thickness vary with tidal phases (Figure 3-3). These variations imply the CBS development (i.e., formation and breakdown), controlled by the sediment availability from the upper water column and the lower mud layer or river bed. When tidal currents are strong, sediment resuspension and entrainment increase due to turbulent shear (Bruens et al., 2012). However, strong stratification (generally triggered by salinity) inhibits the sediment from mixing into the upper water column (Ge et al., 2018). As a result, suspended sediment accumulates near the bottom, leading to the formation of CBS and hence increasing the thickness of the CBS pool. Furthermore, the accumulated sediment produces substantial SSC gradients, enhancing stratification and near-bed sediment trapping (Winterwerp, 2001; Becker

et al., 2018). Such a positive feedback loop provides a favourable situation for the formation and maintenance of a CBS.

A longer CBS pool occurs at the maximum ebb than at the maximum flood (Figure 3-3a and c), which can be explained by stronger stratification during ebb than during flood tides (Pu et al., 2015). As the turbulent mixing exceeds the relatively weak stratification on flood tides, sediment can be mixed higher up into the water (Burchard et al., 2018), resulting in an increased thickness of the CBS pool. Once the amount of sediment transported upward is higher than that available from the bed or fluid mud layer, the CBS will break down. As a result, the CBS pool is the shortest (~10 km) and thickest (~6 m) at the maximum flood. However, stronger stratification at the maximum ebb inhibits vertical mixing and confines sediment in the bottom layer (Geyer, 1993), producing a CBS. Hence, the longest (~30 km) CBS pool appears, but its thickness is less than that at the maximum flood. The differences in the CBS pool between the maximum ebb and the maximum flood confirm the entrainment asymmetry observed by Becker et al. (2018).



Floc size and settling velocity enlarge at slack waters because of low turbulent shears (Guo et al., 2017). The settling flux of sediment thus increases, lowering the SSC in the upper water column and the thickness of CBS (Figure 3-3b and d). However, hindered settling allows for the maintenance of the CBS (Dijkstra et al., 2018). The typical settling velocity in the North Passage is ~0.1 mm/s (Wan et al., 2015). For the gelling concentration of 80 kg/m$^3$ and the mean SSC (28 kg/m$^3$) of the CBS, the effective settling velocity is ~80% lower and less than 0.02 mm/s. The settling from the CBS to the lower fluid mud or bed is thus inhibited, favouring the stability of the CBS.

Our observations show the along-channel and cross-channel movements of the CBS pool during the spring tide. The pool is between CS5 and CS8 at low-water slack and between CS3 and CS7 at high-water slack. During the flood tide, the excursion of the pool is ~10 km, which is consistent with that of saltwater intrusion. The CBS is mainly distributed in the Deepwater Navigational Channel, and the width of the CBS pool is generally less than 1 km. Driven by lateral flows, the CBS moves towards the northern shoals during flood tides and the southern shoals during ebb tides. However, the distance of cross-channel movement is limited due to the small amplitude of lateral flows. Thus, the CBS pool could not reach the shallow shoals protected by the groins. Ge et al. (2018) investigated the formation and breakdown of the CBS on the flanks of the channel by a one-dimensional vertical model. However, we argue that the CBS they observed may result from lateral movements of the CBS pool. High SSC driven by lateral flows from the channel was also observed by Li et al. (2019), although no CBS was detected in their study.

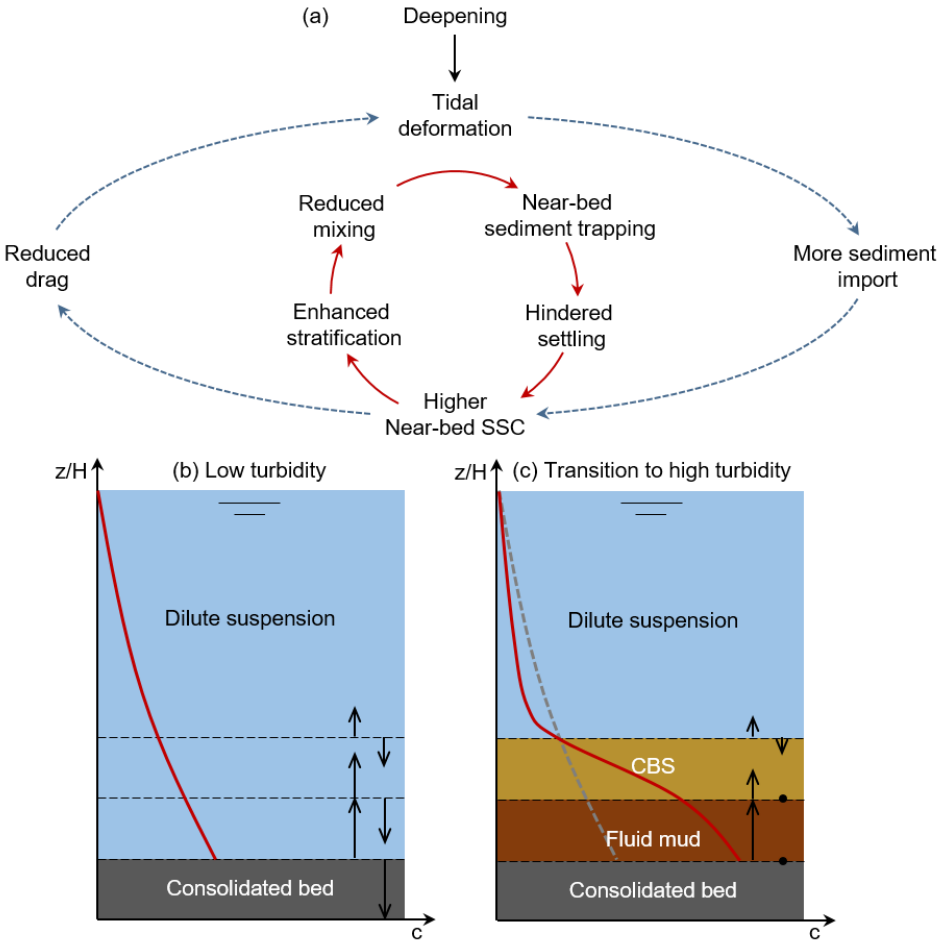


*Figure 3-13: (a) Sketch of the feedback processes underlies a regime shift from low-turbid to hyper-turbid conditions due to deepening. The feedback mechanism combines the positive feedback loop (dashed blue circle) by Winterwerp and Wang (2013) and van Maren et al. (2015) and a positive feedback loop of vertical processes (solid red circle). Schematic diagram showing the states of entrainment/erosion (upward arrows) and settling (downward arrows) before (b) and after (c) deepening, explaining the transition in profiles of suspended sediment concentration (SSC, red lines). The length of the arrows scales the magnitude of sediment flux. Under turbid conditions, the entrainment and settling reduce due to the turbulence damping and hindered settling. The erosion of the bed is similar to that under low-turbid conditions, as no drag reduction occurs in the presence of fluid mud. The SSC profile in panel (b) is duplicated in panel (c) by a grey dashed line. CBS: concentrated benthic suspensions.*

The movements of the CBS pool, together with tidal asymmetry (e.g., slack-water asymmetry and lateral flow asymmetry), shed light on the sediment trapping in the estuary. The slack-water asymmetry in the North Passage suggests a longer slack (when $\tau_b < \tau_{ce}$) after high water than after low water (Figure 3-10a). Much more sediment thus settles from the CBS to the bed during high-water slack (in the middle reaches) than during low-water slack (in the lower reaches). Such along-channel asymmetry in sediment deposition could be amplified when CBS-induced drag reduction is considered (Figure 3-10c). Note that the longer slack also favours the consolidation of deposited sediment, which increases the critical shear stress for resuspension and reduces sediment erosion during subsequent tidal acceleration. Hence, consolidation accelerates the sediment trapping in the middle reaches of the North Passage. Note that our calculations did not account for the dependence of settling velocity on salinity (Figure 3-10c). However, flocculation tests suggest that the salinity effect favours the sediment trapping in the middle reaches of North Passage, as the salinity there is within the most favourable range (8-13 psu) for flocculation (Wan et al., 2015).



The lateral flow asymmetry in the North Passage results from lateral density gradients and the curvature effect (Chen and de Swart, 2018; Zhu et al., 2018; Zhou et al., 2019). Due to the lateral flow asymmetry, the CBS pool tends to move to the south flank of the channel, especially when sediment settles from the CBS to the bed (Figure 3-10b). As a result, more intensive deposition occurs on the south flank than on the north flank of the channel, which may underlie the higher siltation rate on the south flank (Figure 3-10c).

In conclusion, the mobile CBS pool favours the sediment trapping in the middle reaches of the North Passage and on the south flank of the channel. This sediment transport pattern helps to understand how sediment accumulates in an ebb-dominant estuary, favouring the maintenance of ETM and mouth bars in estuaries.

## 3.6. Conclusions

In this chapter, based on field observations in the North Passage of the Changjiang Estuary, we investigated the behaviour of CBS and provided information about the possible underlying mechanisms for the regime shift to hyper-turbid conditions. Historical observations (1988-2015) show a transition in SSC profiles after deepening. The SSC decreased in mid-lower water columns and increased SSC in the bottom layer. This transition could be explained by a positive feedback loop between vertical mixing and settling and the feedback mechanisms hypothesised by Winterwerp and Wang (2013) (Figure 3-13). Our results provide indications for such a mechanism. The sediment accumulation in the estuary, generally driven by the

processes proposed by Winterwerp and Wang (2013), enhances density stratification, upon which fine sediments are trapped near the bed due to turbulence damping and hindered settling. Then a snowball effect is initiated, favouring the formation of CBS and fluid mud. It suggests that the regime shift from low-turbid to hyper-turbid state is a result of the thickening of the CBS and/or fluid mud layer. Such a transition in SSC profiles is expected to be observed in other estuaries undergoing the regime shift.

After the deepening, a mobile CBS pool develops in the North Passage. Its location, length and thickness vary with tidal currents. It is located in the lower reaches at low-water slack and in the middle reaches at high-water slack, with an excursion of ~10 km during the flood tide. Over a tidal cycle during spring tide, the pool has a mean length of ~20 km and a mean thickness of ~4 m. The CBS is mainly located in the Deepwater Navigational Channel. The CBS pool has a narrow width (<1 km). We argued that the CBS on the flanks of the channel results from the cross-channel movements of the CBS pool. The movements of the CBS pool, together with tidal asymmetry (e.g., slack-water asymmetry and lateral flow asymmetry), lead to sediment trapping in the middle reaches and on the south flank of the channel.



The observations by the bottom tripod show the response of the friction ($f$) and drag coefficient ($C_{D(z)}$) to sediment concentration. The results show that both $f$ and $C_{D(z)}$ are constant and minimum in the presence of CBS. The drag reduction is up to 60-80%, which is higher than that observed in laboratory experiments. An empirical relationship was derived by fitting that can be used to predict friction coefficient and the magnitude of drag reduction for sediment transport studies.

## 3.7. Appendix

When calculating the deposition of sediment from CBS, there is a wide range for the choice of gelling concentration ($C_{gel}$). We considered five values (with $C_{gel}$ = 60, 70, 80, 90 and 100 kg/m$^3$) and studied how this choice affected the final estimation of sediment settling from CBS. This sensitivity analysis shows that the gelling concentration significantly affects the net deposition of sediment from CBS (Figure 3-A1). When $C_{gel}$ increases by 10 kg/m$^3$, the settling flux decreases by ~20%. However, different choices of $C_{gel}$ do not change the asymmetry of sediment deposition, i.e., much more sediment tends to deposit in the middle reaches than in the lower reaches of the channel.

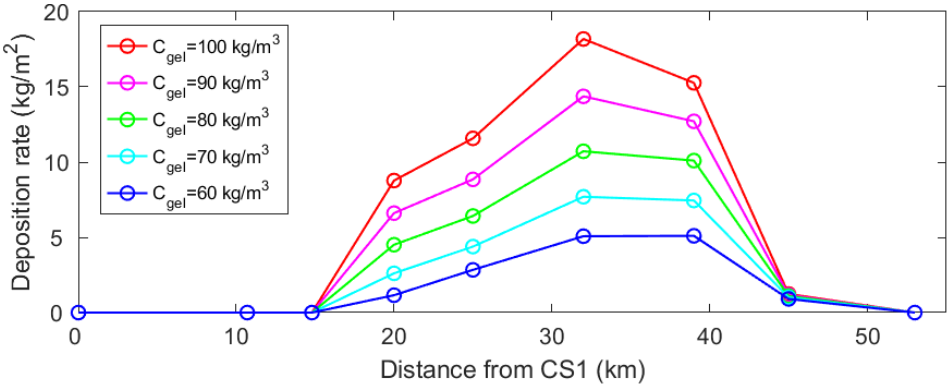


*Figure 3-A1: Along-channel distribution of estimated net deposition rate of sediment from CBS over a tidal cycle during spring tide, with different choices of gelling concentration ($C_{gel}$).*

# 4. Human-driven Changes in Circulation, Stratification and Sediment Transport

*Many estuaries worldwide have been deepened and narrowed to accommodate large vessels. These engineering lead to the changes in tidal range, flood risk, sediment transport and pollutant dispersal. In situ measurements are needed to identify and quantify these changes. Here, we provide along-estuary synchronous observations before and after the Deep Waterway Project (deepening and narrowing) in the North Passage of the Changjiang Estuary. The results indicate that both estuarine circulation and stratification were enhanced after the deepening and narrowing. Increased stratification triggers the positive feedback between stratification, turbulence damping and hindered settling, resulting in near-bed sediment accumulation and hence the formation of concentrated benthic suspensions. Near-bed concentrated suspensions, driven by increased inflows of estuarine circulation, produce a significant sediment import from the sea and sediment convergence at the saltwater intrusion limit. Therefore, along-estuary gradients of sediment concentrations increase. In addition, flow velocity gradients are profound after the works, with higher flow velocities in the middle reaches of the estuary than upstream and downstream. Hence, the dispersive flux (sediment concentration gradients) and spatial lag (velocity gradients) become important, leading to the tidal pumping that drives sediment from high-concentration (high-velocity) to low-concentration (low-velocity) regions. The ETM is thus extended. Overall, the sediment import/trapping is primarily controlled by estuarine circulation and enhanced by deepening and narrowing, leading to increasing sediment concentrations of the ETM. The tidal pumping is responsible for the upstream and downstream extension of the ETM.*

# 4.1. Introduction

Many estuaries worldwide have been modified for human needs, such as channel dredging, reclamation of intertidal flats, and construction of jetties and dikes. These interventions directly modify the morphology and change the tidal propagation, estuarine circulation, sediment transport, biogeochemical cycles and ecosystem functions. Channel deepening (dredging), for instance, increases storm surge (water level) by reducing effective friction in estuaries (Talke et al., 2014; Familkhalili and Talke, 2016; Ralston et al., 2019; Familkhalili et al., 2020). Increased water depths alter tidal phases and amplify tides (Cai et al., 2012; Winterwerp and Wang, 2013; Talke and Jay, 2020). Altered tidal forcing further changes estuarine mixing/stratification and sediment transport, modifying the estuarine turbidity maximum (ETM) (e.g., Talke et al. 2009b; Dijkstra et al., 2019; Grasso and Le Hir, 2019; Lin et al., 2021). The increase in turbidity and suspended sediment concentration (SSC) reduces light penetration and affects water quality and primary productivity (Talke et al., 2009a; Cloern et al., 2014; McSweeney et al., 2017). Modifying the estuary for a specific purpose can directly and/or indirectly affect other functions and processes in the estuary. Human interventions, therefore, need to be considered from different perspectives, requiring a thorough understanding of the estuarine dynamics.



Human interventions do not only lead to a linear effect chain. A feedback loop can be started where processes enhance each other. For example, a regime shift from low-turbid to hyper-turbid states was observed in European estuaries due to channel deepening (Winterwerp et al., 2013). Winterwerp and Wang (2013) attributed this transition to the positive feedback between tidal amplification, sediment import and drag reduction. Specifically, channel deepening increases water depth and reduces the friction impact on tides, leading to enhanced flood dominance and fine sediment import and hence higher SSC. A higher SSC causes turbulence damping and drag reduction, which benefits tidal amplification and deformation, forming a positive feedback loop. By deepening the channel and lowering the roughness (drag), several modelling studies qualitatively reproduced the upstream shift of ETM (Chernetsky et al., 2010; de Jonge et al., 2014) and the transition to hyper-turbid states (van Maren et al., 2015). Dijkstra et al. (2019) provided more evidence for the positive feedback loop with a model in which the drag reduction and increasing SSC are dynamically modelled. Both field observations and model simulations regarding the regime shift mainly focus on the tide-dominated estuaries, where the Canter-Cremers number $N$ ($N = QT/P$: Q is the river discharge, T is the tidal period, and P is the tidal prism) is small. The Ems Estuary, for example, has a mean discharge of ~120 $m^3/s$ and a tidal prism of $1 \times 10^9$ $m^3$, which suggests a Canter-Cremers number of 0.005 (de Jonge, 1992). In this estuary, tidal pumping is crucial in controlling the fine sediment import

(Winterwerp 2011; van Maren et al., 2015; Dijkstra et al., 2019). However, the evidence of the regime shift in SSC is scarce in estuaries with large river discharges, e.g., the Changjiang (Yangtze) River Estuary with a Canter-Cremers number of ~0.5 (Zhang et al., 2016).

With a mean discharge of 28,500 $m^3/s$, the sediment transport in the Changjiang Estuary is governed by barotropic and baroclinic transport processes. Both tidal pumping and estuarine circulation play a vital role in forming an ETM in this large estuary (Shi, 2004; Jiang et al., 2013; Song and Wang, 2013). The Changjiang Estuary has been modified severely by dredging, diking, and reclamations (Zhao et al., 2018; Zhu et al., 2019). For example, the Deep Waterway Project (DWP) has been completed to accommodate larger vessels in the North Passage. As a result, the mean water depth of the main channel increased from ~6.5 m (1997) to ~12.5 m (2010). The navigation channel has a width of 350-400 m, maintained at a depth of 12.5 m by dredging. Model results showed that estuarine circulation is enhanced due to the DWP (Wang et al., 2010; Song and Wang, 2013). Significant siltation occurred around the saltwater intrusion limit because of the enhanced estuarine circulation (Liu et al., 2011; Li et al., 2016; Liu et al., 2019). However, it is still unclear how the DWP affects the ETM movement and extension. Modelling results by Song and Wang (2013) suggest that increased specific discharge (discharge per unit width) forces the ETM downstream. However, Jiang et al. (2013) observed an upstream shift and extension of ETM after the DWP. Recently, Lin et al. (2021) identified a transition in SSC profiles, increasing SSC near the bed and decreasing SSC in the upper water column. Typical near-bed SSC in the ETM increased from 0.2-2.5 $kg/m^3$ (1999) to 0.4-20 $kg/m^3$ (2012), although the fluvial sediment supply declined (Guo et al., 2019; Lin et al., 2021).

Enhanced stratification (a significant vertical density gradient) was found in deepened estuaries, e.g., Seine Estuary (Grasso and Le Hir, 2019) and Hudson Estuary (Ralston and Geyer, 2019). These studies mainly account for salinity stratification as their SSC is relatively low (< 0.2 $kg/m^3$). In the Changjiang Estuary, however, sediment stratification is significant, with near-bed SSC up to 80 $kg/m^3$ and surface SSC of ~0.5 $kg/m^3$ (Wan and Zhao, 2017; L. Li et al., 2018; Lin et al., 2020). The enhancement of stratification may trigger the positive feedback between stratification, turbulence damping and hindered settling. Density stratification suppresses vertical turbulent mixing, benefiting near-bed sediment accumulation and hindered settling (Winterwerp, 2002; Ge et al., 2018; Lin et al., 2021). Hence, high SSC develops near the bed. Such a high SSC, combined with increased landward currents of estuarine circulation, may produce significant upstream sediment transport near the bottom. In addition, stratification may exhibit intra-tidal asymmetries. For example, strain-induced periodic stratification develops during ebb

tides and is destroyed during flood tides (Simpson et al., 1990). This periodic (asymmetric) stratification, linked to turbulence, results in asymmetries in eddy diffusivity and settling velocity (Scully and Friedrichs, 2007; Lin et al., 2021). High SSC can be mixed up higher in the water column during flood tides, leading to landward tidal pumping (Scully and Friedrichs, 2007; Burchard et al., 2018). This tidal pumping may be responsible for the upstream extension of ETM after the channel deepening or may even generate an ETM in the freshwater zone (Jiang et al., 2013; Burchard et al., 2018). To date, the impact of stratification on sediment transport (by estuarine circulation and tidal pumping) in response to channel deepening is understood conceptually. More direct evidence is required from field observations or modelling for quantification. Nevertheless, the relative contributions of tidal pumping and estuarine circulation in controlling sediment import and ETM evolution remain unclear.

Previous studies mainly focused on the importance of channel depth in estuarine circulation and stratification (see review by MacCready and Geyer, 2010). Recently, Ralston and Geyer (2019) argued that narrowing controls the estuarine circulation in the Hudson Estuary, where the estuarine circulation had no significant changes after deepening and limited narrowing. Therefore, further observations or model results are necessary to improve our understanding of the impacts of deepening and narrowing on estuarine circulation and sediment dynamics. This chapter aims to identify the response of estuarine circulation, stratification and sediment transport to channel deepening and narrowing and reveal the interaction between stratification and sediment transport. These aims are achieved by analysing the data set collected before and after the DWP in the North Passage. The following section introduces the Changjiang Estuary and the DWP. The data and methods used in this study are described in Section 4.3. Section 4.4 presents the changes in topography, estuarine circulation, stratification, and sediment transport mechanisms. The role of narrowing (estuary width) in estuarine circulation and the effects of stratification on sediment transport are discussed in Section 4.5. Finally, Section 4.6 summarises the conclusions of this study.



## 4.2. The Deep Waterway Project

The Changjiang (Yangtze) River is the largest river in Asia in terms of water and sediment discharges. Long-term (1950-2010) observations at the Datong Hydrological Gauging Station (~640 km upstream from the river mouth) show that the annual discharge is up to $9 \times 10^{11}$ $m^3$ (CWRM, 2015). Recently, the sediment load decreased from $4.7 \times 10^8$ tons (1953-1985) to $1.3 \times 10^8$ tons (2003-2015) due to the soil conservation strategies and dam constructions in the river basin (Guo et al., 2019). Meanwhile, the water discharge reduced profoundly in the wet season

and slightly increased in the dry season, although its yearly mean value was relatively stable (L. Guo et al., 2018).

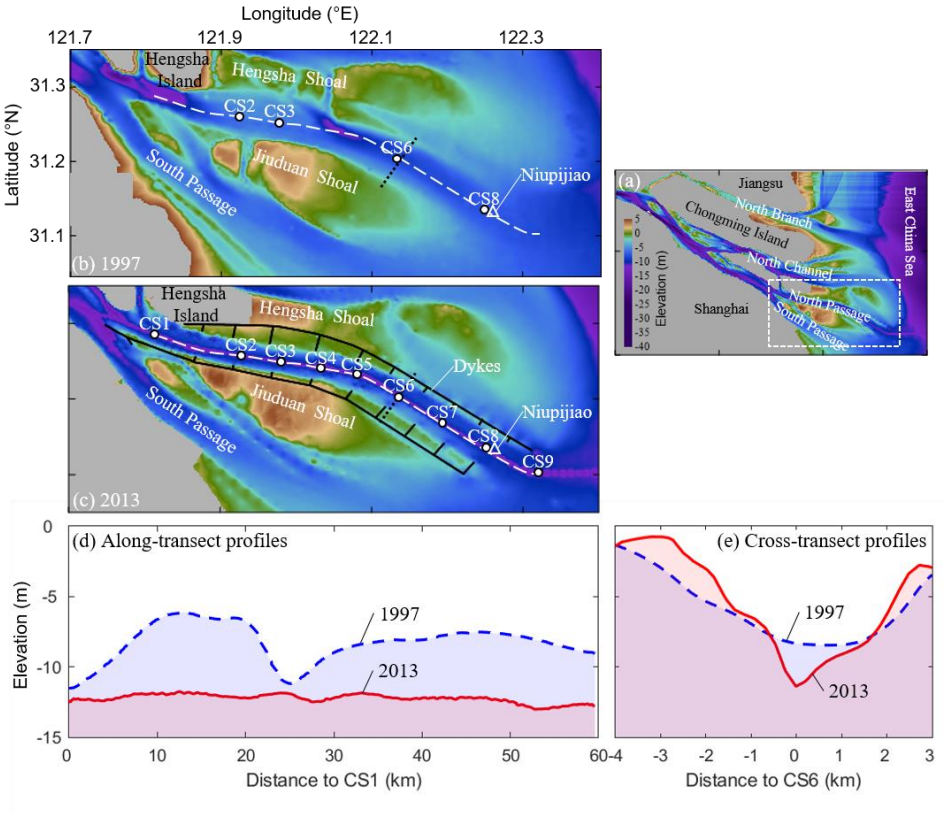


*Figure 4-1: (a) Map of the Changjiang Estuary and the bathymetry of the North Passage in (b) 1997 and (c) 2013. The Elevation is relative to the Theoretical Depth Datum. Black lines show the Deepwater Navigational Channel (DNC), and white dots represent observation stations (Wan, 2015). The colour indicates the depth relative to the mean lower low water. The triangle denotes the tide gauging station at Niupijiao. Along-transect (white dashed lines) and cross-transect (black dotted lines) profiles are shown in panels (d) and (e), respectively. Positive x is defined seaward along the channel and positive y across the channel to the northeast.*

The modern Changjiang Estuary is a large depositional system with significant river and tidal forcing. A large amount of riverine sediment is supplied into the Changjiang Estuary, forming one of the most remarkable ETMs and multi-channel estuarine systems. There are four outlets (i.e., North Branch, North Channel, North Passage, and South Passage) to the East China Sea (Figure 4-1a). The Changjiang Estuary

has a meso-tidal regime, with a mean tidal range of 2.7 m and a maximum tidal range of 5.0 m at the Niupijiao Tide Gauging Station (Guo et al., 2015). Under combined river and tidal forcing, the Changjiang Estuary is partially stratified most of the time. It can be highly stratified in the wet season with a discharge of up to 60,000 $m^3/s$ and well mixed during spring tides in the dry season with a low discharge of ~10,000 $m^3/s$ (Pu et al., 2015).

To improve the cargo capacity and provide access to inland ports for larger vessels, the North Passage has been deepened and dyked (Figure 4-1b). The Deep Waterway Project (DWP) was launched in 1998 and implemented in three phases to achieve water depth of (I) 8.5 m in 2002, (II) to 10 m in 2005 and (III) to 12.5 m in 2010. The regulation includes two 50-km-long jetties parallel to the channel and 19 groynes perpendicular to the channel. With additional dredging, the depth of the navigation channel reached 12.5 m in 2009. As a result, saltwater intrusion and stratification were enhanced, leading to a more landward extended and migrated ETM zone (Zhu et al., 2006; Wang et al., 2010; Jiang et al., 2013; Song and Wang, 2013; Chen et al., 2020). The ETM exhibits seasonal variations, with a relatively lower SSC and more mixed profile in the dry season and higher SSC concentrated near the bottom in the wet season (Wu et al., 2012; L. Li et al., 2018; Hua et al., 2020; Lin et al., 2020). Although the riverine sediment load has declined in recent two decades, the near-bed SSC in the ETM shows a notable increase (up to 80 $kg/m^3$) (Xu, 2009; Liu et al., 2011; Jiang et al., 2013; Wan and Zhao, 2017; Ge et al., 2018; Lin et al., 2021). The established near-bottom high SSC may further increase the actual water density and enhance the vertical density stratification (Song et al., 2013; L. Li et al., 2018; Li et al., 2019; Lin et al., 2021).



## 4.3. Materials and Methods

### 4.3.1. Data Collection

To assess the effect of DWP (i.e., channel deepening and narrowing) on estuarine stratification and sediment transport, we analysed the measurements observed in the North Passage before (June 1999) and after (August 2012) the DWP. Both field works were performed by the Changjiang Estuary Waterway Administration Bureau during spring tides (Table 4-1); see also Wan (2015). The data set in 1999 was collected at four stations along the North Passage; the measurements in 2012 included nine stations (Figure 4-1). Table 4-1 provides details for the two campaigns. The river discharges at Datong during the two observation periods were 54,300 and 52,500 $m^3/s$, respectively, with a difference of <3%. The tidal ranges during the two observations were similar, with 3.3 m before the DWP and 3.7 m after the DWP (Table 4-1). Given similar river and tidal forcing conditions, these two data sets can

be used to examine the effect of the DWP on estuarine circulation, density stratification and sediment transport dynamics. Note that the fluvial sediment supply showed a reduction of 60% due to the damming in the river basin, from 340 Mt/y before the DWP to 132 Mt/y after the DWP, although the river discharge was similar (Zhu et al., 2019).

*Table 4-1: Details on the in-situ measurements*

| Month/year | Observation period (date/h) | Observation stations | Tidal range* (m) | Discharge** ($m^3/s$) |
|---|---|---|---|---|
| June/1999 | 29/18:00-30/10:00 | CS2, CS3, CS6, CS8 | 3.3 | 54,300 |
| August/2012 | 17/05:00-17/19:00 | CS1-CS9, CS6s, CS6n | 3.7 | 52,500 |

* Tidal range measured at the mouth of the estuary (the Niupijiao Tide Gauging Station);** Monthly mean river discharge at the tidal limit (the Datong Hydrological Gauging Station).

Data of flow velocity, salinity and SSC were collected every 30 min at each station in six relative-depth layers, i.e., $z/H = 0.05$ (near the bottom), 0.2, 0.4, 0.6, 0.8, and 0.95 (near the surface), where $H$ is the water depth and $z$ denotes the height above the bed. Flow velocity and direction were obtained by rotor current meter (RCM), with an accuracy of 0.01 m/s and 1°, respectively. In addition, water samples were collected to detect salinity and SSC. A calibrated salimeter measured salinity with an accuracy of 0.01 practical salinity units (psu). SSC was determined by filtration of water samples through a pre-weighed filter and drying at 60 °C for 8 hours.



### 4.3.2. Local Sediment Flux Decomposition

Sediment fluxes are determined by integrating the velocity and concentration product over the cross-estuary section and over time. Therefore, a cross-section measurement is required, especially as the bathymetry is not uniform with the deep channel and shallower sides. The total sediment flux can be decomposed by considering temporal and spatial variations of the sediment concentration and velocity on top of the mean values (Dyer, 1974; Su and Wang, 1986). The cross-terms of the variations provide various contributions. Here, we follow a similar but slightly different approach. As we only have a vertical profile of the velocity and concentration, we decompose the product of the concentration and the velocity. The different components can be compared, and the comparison between before and after the DWP can be made. The method allows for showing the variations over the depth as well.

According to the standard procedure of decomposition (Dyer, 1974; Su and Wang, 1986), the instantaneous along-estuary (longitudinal) velocity ($u$) at any depth can be written as the sum of the tidal average ($u_0$) and the tidal oscillation ($u_t$), i.e.

$$u = u_0 + u_t \tag{4.1}$$

where turbulent fluctuation is filtered out. The tide-averaged component can be further divided into a depth-averaged component ($\overline{u_0}$) and the deviation ($u_0'$) from it,

$$u_0 = \overline{u_0} + u_0' \tag{4.2}$$

Hence,

$$u = \overline{u_0} + u_0' + u_t \tag{4.3}$$

Similarly, suspended sediment concentration ($c$) can be expressed as

$$c = \bar{c_0} + c_0' + c_t \tag{4.4}$$

According to Equations 4.3 and 4.4, the product of the velocity and concentration (local flux) at each height includes nine terms. Averaged over a tidal cycle, however, it becomes

$$\langle uc \rangle = \underbrace{\langle \overline{u_0}\bar{c_0} \rangle}_{1} + \underbrace{\langle u_0' c_0' \rangle}_{2} + \underbrace{\langle u_t c_t \rangle}_{3} + \underbrace{\langle \overline{u_0} c_0' \rangle}_{4} + \underbrace{\langle u_0' \bar{c_0} \rangle}_{5} \tag{4.5}$$

as $\langle u_t \bar{c_0} \rangle = \langle u_t c_0' \rangle = \langle \overline{u_0} c_t \rangle = \langle u_0' c_t \rangle = 0$, where the brackets stand for tidal averaging. Term 1 is the advective flux by mean flow, i.e. the barotropic component (also known as non-tidal drift). Term 2 is the flux caused by the vertical shear effect, driven by estuarine circulation. The sum of terms 1 and 2 represents the flux by advection. Term 3 denotes the tidal pumping, which is correlated with the tidal fluctuations of velocity and sediment concentration. Note that the integrals of the last two terms over the water depth are equal to zero. In other words, these two terms cannot produce residual sediment fluxes in the entire water column. Therefore, we focus on the first three terms in the subsequent analyses. Positive along-channel velocities (*u*) at stations CS1, CS2, CS3, CS4, CS5, CS6, CS7, CS8 and CS9 indicate the directions of 115°, 101°, 101°, 101°, 113°, 125°, 125°, 125° and 90° clockwise from the north, respectively.

### 4.3.3. Potential Energy Anomaly

Potential energy anomaly $\varphi$ (J/m$^3$) is a variable to quantify water density stratification (Simpson et al., 1990). It is defined as the change in potential energy relative to the well-mixed condition,

$$\varphi = \frac{1}{H}\int_0^H (\bar{\rho} - \rho) g z \mathrm{d}z \tag{4.6}$$

where $\rho$ is the water density, $\bar{\rho}$ the depth-averaged density, $z$ the vertical coordinate and $g$ the gravitational acceleration. For a given density profile, $\varphi$ represents the amount of work required for uniform vertical mixing per unit of volume. Therefore, it is a scalar parameter describing stratification intensity.

The water density is defined by:

$$\rho = \rho_w + \left(1 - \frac{\rho_w}{\rho_s}\right) C \tag{4.7}$$

with $\rho_w$ is the density of the water, and $C$ is the suspended sediment concentration. $\rho_s$ is primary particle density estimated to be 2,570 kg/m$^3$ in the Changjiang Estuary (Guo et al., 2017). The temperature variation (<1 °C) in the water column was negligible during the observations. The effect of temperature is therefore excluded in this study.

Without source and sink terms, such as surface heating, stirring and rain, the change rate of $\varphi$ is described by

$$\frac{\partial \varphi}{\partial t} = \frac{g}{H}\int_0^H \frac{\partial(\bar{\rho}-\rho)}{\partial t} z \mathrm{d}z \tag{4.8}$$



where $t$ is time. Simpson et al. (1990) proposed the concept of tidal straining for the effect of differential advection. Considering advection only in along-estuary direction ($x$) and assuming that the density gradient in that direction is independent of depth, they derived the classical tidal straining equation,

$$\frac{\partial \varphi}{\partial t} = \frac{g}{H}\frac{\partial \bar{\rho}}{\partial x}\int_0^H (u - \bar{u}) z \mathrm{d}z \tag{4.9}$$

where $u$ is along-estuary velocity and $\bar{u}$ the depth-averaged velocity.

De Boer et al. (2008) extended the potential energy anomaly equation to three dimensions (see also Burchard et al., 2008):

$$\frac{\partial \varphi}{\partial t} = \frac{g}{H}\int_0^H \left( \begin{array}{c} \overbrace{\bar{u}\frac{\partial \tilde{\rho}}{\partial x}}^{A_x} + \overbrace{\tilde{u}\frac{\partial \bar{\rho}}{\partial x}}^{S_x} + \overbrace{\tilde{u}\frac{\partial \tilde{\rho}}{\partial x}}^{N_x} - \overbrace{\frac{1}{H}\frac{\partial \bar{\tilde{u}}\bar{\tilde{\rho}}H}{\partial x}}^{C_x} + \overbrace{\frac{\partial \langle u'\rho' \rangle}{\partial x}}^{D_x} + \overbrace{w\frac{\partial \rho}{\partial z}}^{W_z} - \overbrace{\frac{1}{H}\langle w'\rho' \rangle|_{\mathrm{s}}}^{D_s} \\ + \underbrace{\bar{v}\frac{\partial \tilde{\rho}}{\partial y}}_{A_y} + \underbrace{\tilde{v}\frac{\partial \bar{\rho}}{\partial y}}_{S_y} + \underbrace{\tilde{v}\frac{\partial \tilde{\rho}}{\partial y}}_{N_y} - \underbrace{\frac{1}{H}\frac{\partial \bar{\tilde{v}}\bar{\tilde{\rho}}H}{\partial y}}_{C_y} + \underbrace{\frac{\partial \langle v'\rho' \rangle}{\partial y}}_{D_y} + \underbrace{\frac{\partial \langle w'\rho' \rangle}{\partial z}}_{M_z} + \underbrace{\frac{1}{H}\langle w'\rho' \rangle|_{\mathrm{b}}}_{D_b} + Q \end{array} \right) z \mathrm{d}z \tag{4.10}$$

where $x$, $y$ and $z$ refer to the longitudinal (along-estuary), lateral (cross-estuary) and vertical directions, respectively. This equation provides a detailed overview of the terms that control the mixing and stratification in estuarine and coastal regions. $A_x$ and $A_y$ represent the longitudinal and lateral advection, respectively. They describe

the advection of density stratification driven by depth-averaged flows. $S_x$ and $S_y$ denote straining terms, and $S_x$ is the term represented in Equation 4.9. The analyses by de Boer et al. (2008) show that advection and straining are principal terms while the contribution by the remaining terms is negligible. Therefore, we mainly examine the four terms related to advection and straining, focusing on their role in estuarine stratification and sediment transport.

### 4.3.4. Eddy viscosity

Eddy viscosity ($\nu_t$) is a representative proportionality factor describing the momentum transfer due to moving eddies in the water column, while eddy diffusivity ($K_t$) describes the mixing of salt and sediment. They link to each other by the turbulent Prandtl–Schmidt number ($Pr_t$): $k_t = \nu_t / Pr_t$. To access the eddy viscosity for the entire water column, we employed the model proposed by Munk and Anderson (1948):

$$\nu_t = \kappa u_* z \left(1 - \frac{z}{H}\right)(1 + 10Ri)^{-\frac{1}{2}} \tag{4.11}$$

where $k$ is Karman's constant (0.41), $z$ is the height above the bed, and $H$ is water depth. The friction velocity ($u_*$) is estimated by the law of the wall. The gradient Richardson number ($Ri$) is given as $Ri = -\frac{g}{\rho}\frac{\partial \rho}{\partial z} / [\left(\frac{\partial u}{\partial z}\right)^2 + \left(\frac{\partial v}{\partial z}\right)^2]$, standing for the ratio of the buoyancy term to the flow shear term. It is thus a measure of the relative importance of mechanical and stratification effects in the water column. The vertically and tidally averaged eddy viscosity ($K_M$) links stratification to estuarine circulation (also known as exchange flow) (Hansen and Rattray, 1965; MacCready and Geyer, 2010; Chant et al., 2018), as

$$U_e = \frac{1}{48}\frac{\beta_s g H^3}{K_M}\frac{\partial S}{\partial x} \tag{4.12}$$

where $U_e$ represents the intensity of estuarine circulation (i.e., exchange flow), $\beta_s$ the coefficient of saline contraction and ∂S/∂x along-channel salinity gradient. Equation 4.12 can identify how the Deep Waterway Project alters the estuarine circulation by modifying depth, stratification and salinity gradients.

## 4.4. Results

### 4.4.1. Topographic changes

The topographies in 1997 and 2013 represent pre- and post-DWP conditions, respectively. The increases in thalweg depth over this period vary along the North Passage (Figure 4-2c). The most significant increase occurred in the upper reaches between CS2 and CS3, where depths increased more than 70%. In the lower reaches between CS6 and CS9, depths increased by 40–60%. Similarly, the mean cross-

section depth doubled at CS2 and increased 10-60% in other sections (Figure 4-2b). The cross-section area decreased due to the decreased estuary width despite increased channel depth. The width of the North Passage decreased by 10-70% (Figure 4-2d). The reductions in the cross-section area increased seaward, from 10% at CS1 to 50% at CS8 (Figure 4-2a). Overall, the topographic changes indicate the deepening of the main channel and the narrowing by the reclamation in groyne fields.

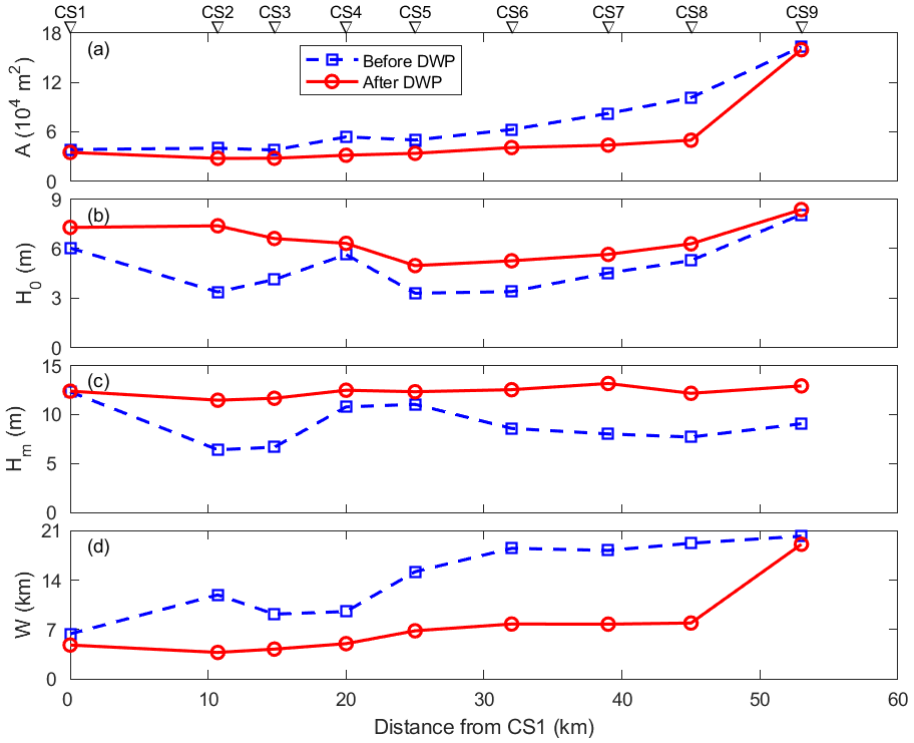


*Figure 4-2: Topographic changes along the North Passage. (a) Cross-section area versus distance from the CS1 before (1997) and after (2013) the Deep Waterway Project (DWP); (b) cross-section mean depth; (c) thalweg depth; and (d) width of the North Passage.*

### 4.4.2. Velocity, salinity and SSC

As a consequence of the narrowing, the flow velocity was accelerated in the North Passage. The maximum velocity was up to 3.2 m/s after the DWP, larger than the velocity (2.8 m/s) before the DWP. Both peak velocity and duration of ebb tides increased due to the DWP. At CS3, for instance, the peak depth-averaged ebbing velocity increased from 1.8 m/s to 2.8 m/s, while the velocity for flooding remained

at ~0.9 m/s. Meanwhile, the duration of the ebb tide increased from 7.8 hours to 8.1 hours. Accordingly, the duration of the flood tide decreased from 4.7 hours to 4.4 hours. These increases were particularly significant near the surface and in the upper reaches of the North Passage (Figure 4-3).

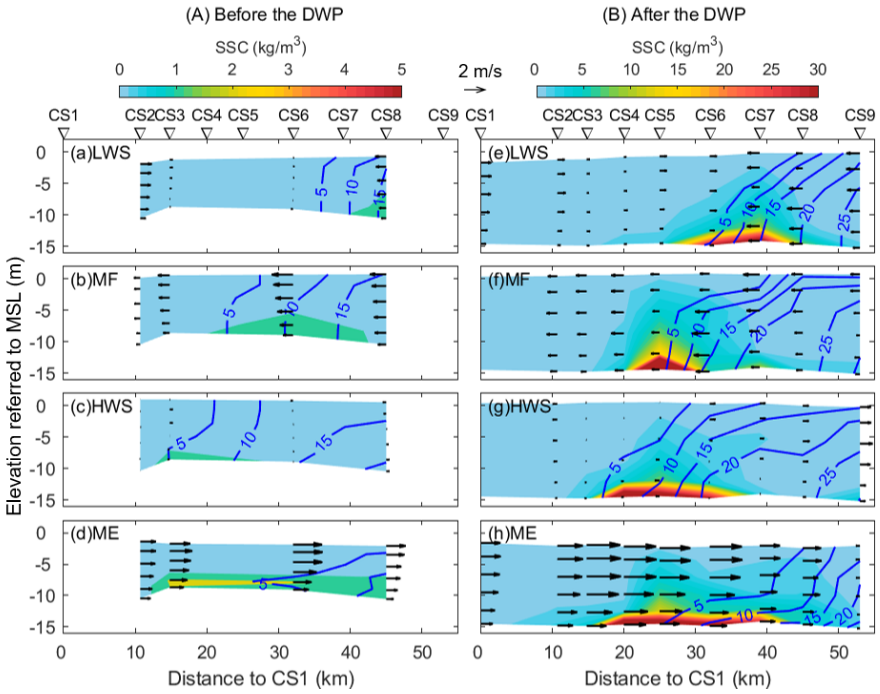


*Figure 4-3: Along-estuary distributions of velocity (arrows), salinity (contour lines) and suspended sediment concentration (SSC; filled contours) at the time of (a) (e) low-water slack (LWS), (b) (f) maximum flood (MF), (c) (g) high-water slack (HWS) and (d) (h) maximum ebb (ME) before (left panels) and after (right panels) the Deep Waterway Project (DWP). Note the different colour bars for the left and right panels. MSL: mean sea level.*

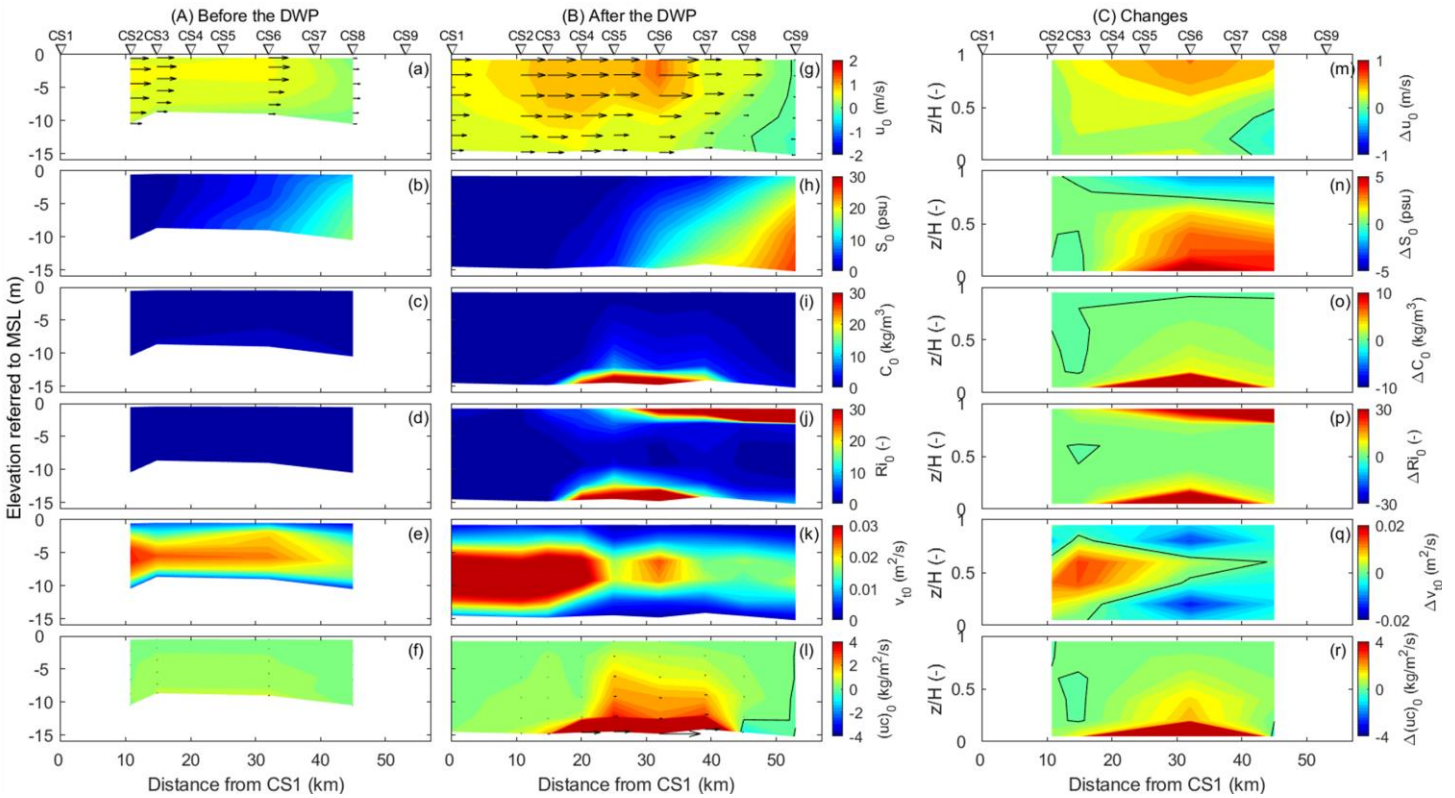


*Figure 4-4: (a) (g) Along-channel residual flow, tidally averaged (b) (h) salinity, (c) (i) suspended sediment concentration, (d) (j) Richardson number, (e) (k) eddy viscosity and (f) (l) along-channel residual sediment flux (A) before and (B) after the Deep Waterway Project (DWP) and (C) the difference in between. Positive residual flow and sediment flux denote the seaward direction along the channel and the negative landward. Black lines show the contour line of zero.*

After the DWP, the saltwater intrusion limit was similar to before the DWP. The contour line of 5 psu, for example, intruded from CS6 at low water slack to CS3 at high water slack (Figure 4-3). Over a tidal cycle, the saltwater intrusion limit was located at ~15 km from CS1 before and after the DWP (Figure 4-4b and h). However, near the mouth, saltwater intruded much further upstream after the DWP than before the DWP. For example, the salinity of 20 psu can only reach CS8 before the DWP, but it can intrude ~10 km further upstream, reaching CS6 after the DWP. Note that enhanced saltwater intrusion (i.e., salinity increase) mainly occurred near the bottom and at the mouth of the North Passage. Near the surface, increased seaward flushing of freshwater caused a reduction in salinity (Figure 4-4n). As a result, a stronger salinity stratification was developed after the DWP (Figure 4-4h). Such a stratification will be quantified by the potential energy anomaly in Section 4.4.5.

The region of the ETM was expanded, and its SSC increased significantly after the DWP (Figure 4-3). The SSC was up to 88 kg/m$^3$ after the DWP, much larger than that prior to the DWP (<5 kg/m$^3$). Figure 4-3 shows that the position of ETM varied with time and tidal currents. At each tidal phase, the ETM had a more significant length after the DWP than before the DWP, although it was maintained near the saltwater intrusion limit. Over a tidal cycle, the ETM had a mean length of ~45 km, approximately 50% longer than that (30 km) before the DWP (Figure 4-4c and i).



### 4.4.3. Residual flows and estuarine circulation

Figures 4-4a and 4-4g show along-channel residual flows before and after the DWP, respectively. Before the DWP, the residual flows were seaward-directed between CS2 and CS8 (Figure 4-4a). Their magnitude decreased toward the sea and increased from the bottom to the surface. At CS2, for instance, the residual flow was ~0.4 m/s near the bottom and ~0.6 m/s near the water surface. At CS8, it was nearly uniform throughout the water column, with a magnitude of ~0.1 m/s. No data was available in further downstream, and no circulation was observed during the campaign of 1999.

After the DWP, residual flows increased significantly, particularly near the water surface (Figure 4-4g). At CS6, for example, the residual surface flow was doubled from 0.6 m/s to 1.2 m/s. Moreover, a landward residual flow of 0.1 m/s was detected at the mouth. It suggests a residual circulation with a null point between CS8 and CS9. Note that the CS9 is out of the North Passage, where the tidal flow is rotating instead of reciprocating. The landward (westward) residual component at CS9 results from the decomposition of the south-westerly residual flow, which is part of the horizontal circulation.

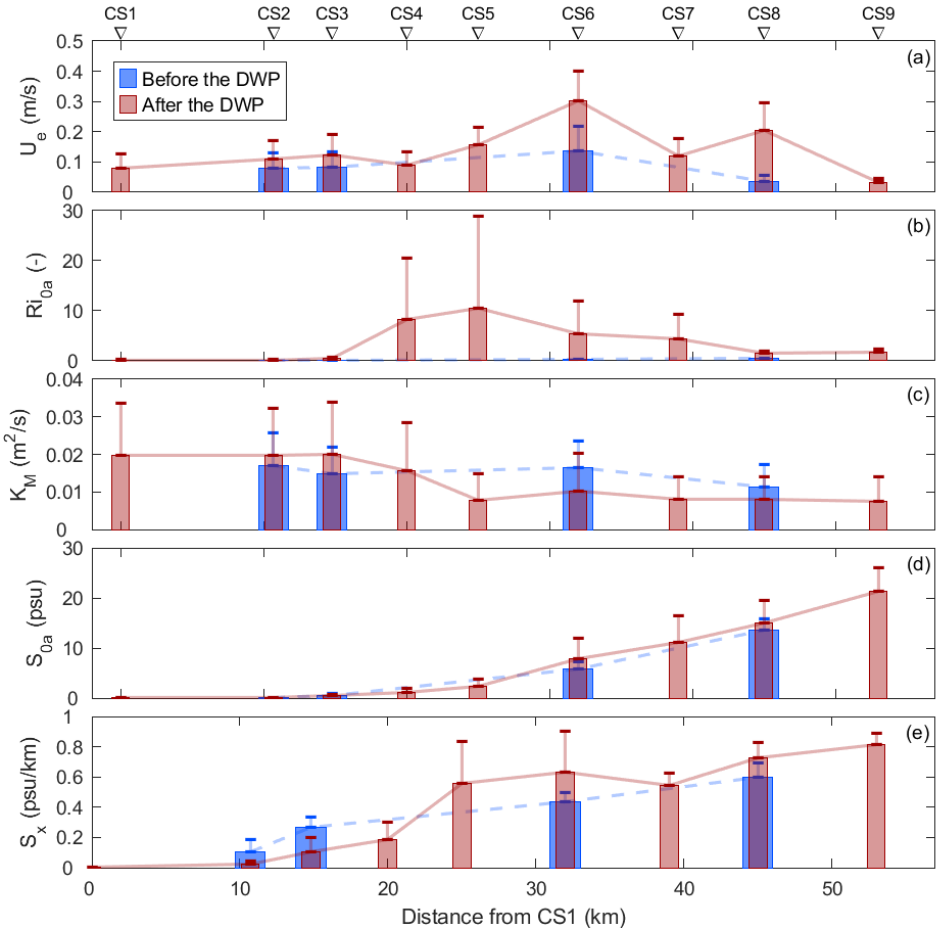


*Figure 4-5: Along-channel distributions of vertically and tidally averaged (a) exchange flow ($U_e$), (b) Richardson number ($Ri_{0a}$), (c) eddy viscosity ($K_M$), (d) salinity ($S_{0a}$) and (e) along-channel salinity gradient ($S_x$) before and after the Deep Waterway Project (DWP).*

Increased estuarine circulation is also confirmed by increases in exchange flow (Figure 4-5a). A strict definition of gravitational circulation (also known as exchange flow) includes the vertically varying component of tidally averaged velocity (Lerczak et al., 2006; MacCready, 2011). The exchange flow ($U_e$) here is calculated by Equation 4.12. Prior to the DWP, $U_e$ was generally less than 0.1 m/s. After the DWP, $U_e$ increased up to ~0.3 m/s. The increases in $U_e$ varied along the North Passage but were greatest at CS6 and CS8, where $U_e$ was three-fold than that before the DWP (Figure 4-5a).

### 4.4.4. Stratification

The potential energy anomaly was calculated to quantify the density stratification before and after the DWP, see Figure 4-6. We decomposed the total potential energy anomaly ($\phi$) into salinity-induced ($\phi_{sal}$) and sediment-induced ($\phi_{sed}$) components to reveal the feedback effect of sediment suspension.

Prior to the DWP, the stratification in the North Passage was relatively weak, with $\phi$ of <100 J/m$^3$. Salinity-induced density differences dominated the stratification, particularly in the lower reaches. The effect of sediment suspension was limited ($\phi_{sed}$ <10 J/m$^3$). Low $\phi_{sal}$ occurred during the flood tide, indicating well-mixed conditions. Salinity stratification ($\phi_{sal}$ up to 97 J/m$^3$) developed directly from the high water slack to the maximum ebb (Figure 4-8a). This pattern was similar to the classic strain-induced periodic stratification, i.e., stratification develops during ebb tides and breaks down during flood tides (Simpson et al., 1990). However, the salinity stratification broke down during the late ebb due to the retreat of the salt wedge, see Figure 4-3.



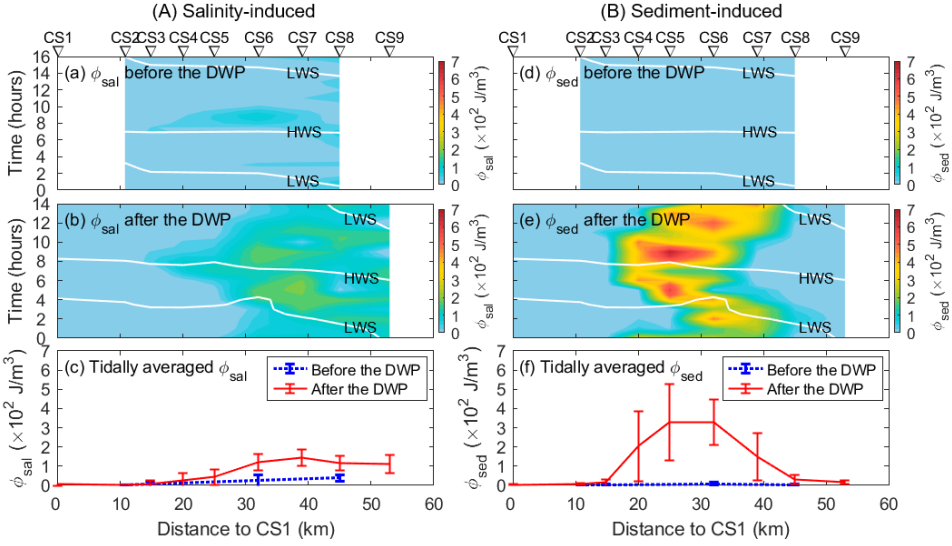


*Figure 4-6: Tidal variations of (A) salinity-induced and (B) sediment-induced potential energy anomaly (a) (d) before and (b) (e) after the Deep Waterway Project (DWP) and (c) (d) their tidal averages along the North Passage. White lines indicate high (HWS) and low water slack (LWS).*

After the DWP, the salinity-induced potential energy anomaly showed an increasing trend in the seaward direction, with a magnitude up to 220 J/m$^3$. Its intra-tidal variations followed the movement of the salt wedge, particularly at the front of the

salt wedge. During flood tides, $\phi_{sal}$ gradually increased, withstanding the advancement of the salt wedge. During ebb tides, it declined with the seaward retreat of the salt wedge (Figure 4-6b). Over a tidal cycle, averaged $\phi_{sal}$ was about three-fold (up to 140 J/m$^3$) larger after completing the DWP than before the DWP.

Sediment-induced density difference became a profound contribution to the total stratification after the DWP (Figure 4-6e). In the middle reaches (between CS4 and CS7), where highly concentrated suspensions developed, $\phi_{sed}$ was predominant compared to $\phi_{sal}$ (Figure 4-6e). The maximum $\phi_{sed}$ was up to 700 J/m$^3$. Similar to $\phi_{sal}$, $\phi_{sed}$ potentially increased and declined during the flood and ebb tides, respectively. High $\phi_{sed}$, however, occurred during the accelerating or decelerating phase, which is likely ascribed to the sediment resuspension or deposition. The tidally averaged $\phi_{sed}$ after completion of the DWP was 30-fold (up to 330 J/m$^3$) that before the DWP. An increased potential energy anomaly implies that more energy is needed to mix the water column. Enhanced stratification was also confirmed by increased Richardson number (*Ri*) (Figures 4-4j and 5b). The increases in *Ri* were most significant in the middle North Passage between CS4 and CS7, where *Ri* (>4.0) was more than 30-fold. Accordingly, eddy viscosity was reduced by 30-40% (Figure 4-5c), indicating weaker vertical mixing.



### 4.4.5. Sediment transport

Figure 4-4f shows that along-channel residual (net) sediment flux was predominantly seaward before the DWP. Since high SSC was concentrated in the bottom layer, the residual sediment flux was more significant near the bottom (0.5 kg/m$^2$/s) than near the surface (0.1 kg/m$^2$/s). Longitudinally, its magnitude slightly declined from CS3 to CS8, resulting in landward gradients and sediment trapping. After the DWP, the magnitude of residual sediment transport was greatly strengthened, particularly in the bottom layer of the middle reaches (>10.0 kg/m$^2$/s), where extremely high SSC (>80 kg/m$^3$) developed, see Figure 4-4l. In terms of direction, the residual sediment transport remained seaward between CS1 and CS8. However, landward sediment transport predominated at the mouth of the North Passage, resulting in sediment convergence around CS8.

In order to reveal the mechanism underlying the changes in sediment transport and ETM, sediment transport decomposition was conducted according to Section 4.3.2. First, the total residual sediment flux was decomposed into a tidal pumping contribution and an advective flux. Then, the latter was further divided into an exchange flow (i.e., estuarine circulation) and a barotropic component. The results show that the barotropic component was predominant, and the contributions by estuarine circulation and tidal pumping were limited before the DWP (Figure 4-7a).

The relatively high contribution of barotropic flux was likely related to the large discharge (54,300 $m^3/s$) during the observation.

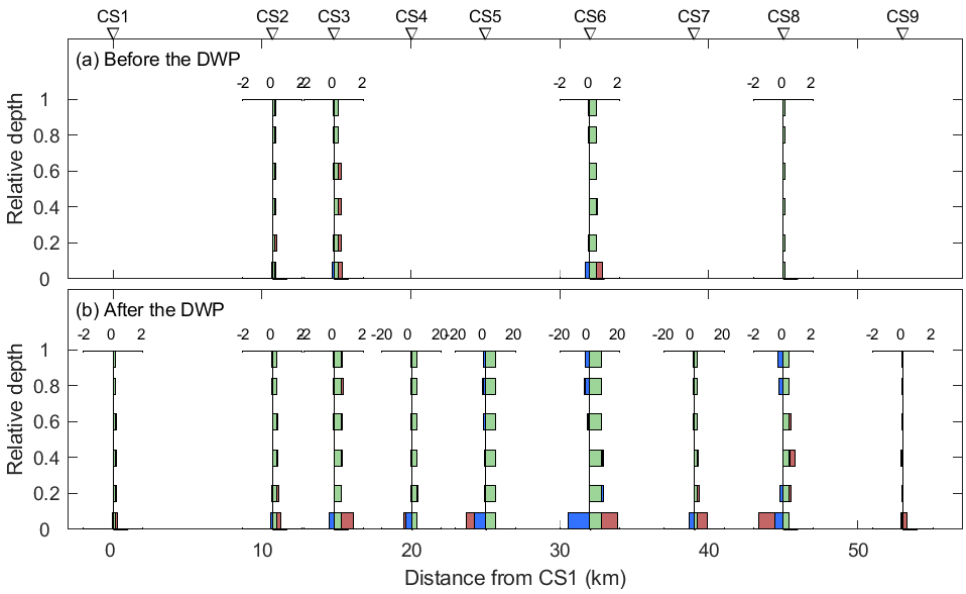


*Figure 4-7: Along-channel sediment fluxes driven by barotropic (green), estuarine circulation (blue) and tidal pumping (brown) components (a) before and (b) after the Deep Waterway Project (DWP). Positive values denote seaward direction and negative landward. Note the different scales in the lower panel at CS4, CS5, CS6 and CS7.*

After the DWP, the barotropic flux was strengthened throughout the North Passage (Figure 4-7b). It predominates over estuarine circulation and tidal pumping in the upper water columns. Increased barotropic flux benefited seaward sediment transport. However, near the bottom, the transports by estuarine circulation and tidal pumping were greatly enhanced after the DWP. Enhanced estuarine circulation resulted in significant landward sediment transport (up to 15 $kg/m^2/s$). In the middle reaches where ETM developed, tidal pumping drove sediment upstream at the riverside of the ETM (e.g., CS4) but downstream at the seaside (e.g., CS6 and CS7). At CS8, tidal pumping caused seaward sediment transport in the middle layer and landward near the bottom. Near the bottom, the sum of the three terms was seaward at CS3 but landward at CS8, indicating sediment convergence (Figure 4-7b). This near-bed sediment convergence favours the development of ETM and high SSC.

The pattern of sediment transport by advection (i.e., the sum of barotropic and estuarine circulation components) and tidal pumping is shown in Figure 4-8. Before the DWP, both advection and tidal pumping were limited, with a magnitude of <0.5 kg/m$^2$/s. The advection was seaward across the whole water column throughout the North Passage. The tidal pumping was seaward in the upper reaches (CS2 and CS3) but gradually turned landward in the downstream reaches. After the DWP, advection and tidal pumping increased (up to 10 kg/m$^2$/s), especially in the middle reaches (between CS4 and CS7). The advection exhibited a classical circulation, with seaward fluxes in the upper layer and landward near the bottom, leading to near-bed sediment convergence in the middle reaches of North Passage. The tidal pumping, however, accumulated sediment at the upstream and downstream limits of ETM (i.e. CS3 and CS8).

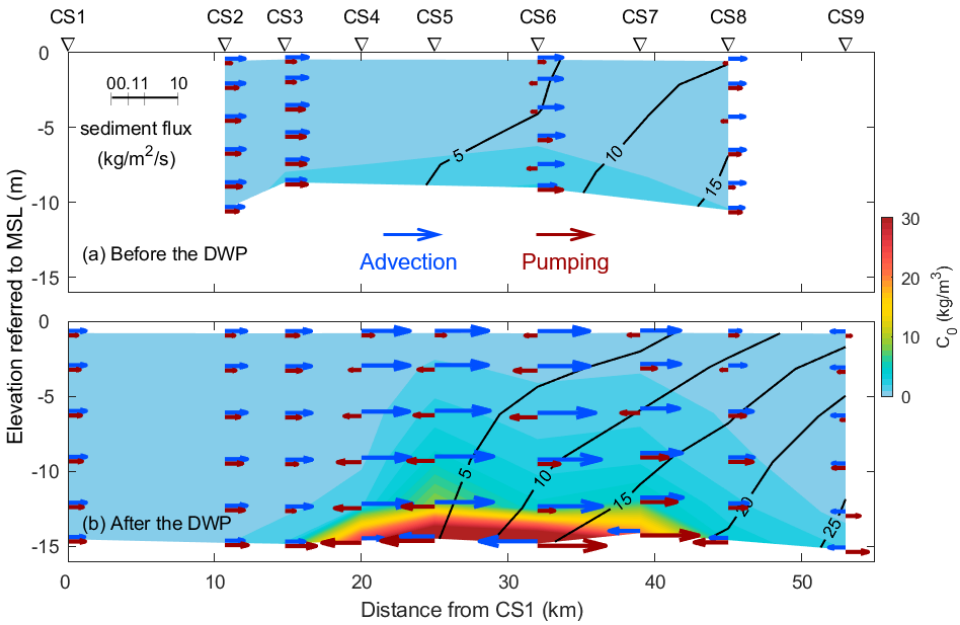


*Figure 4-8: Along-channel sediment fluxes driven by advection (blue) and pumping (red) before (a) and after (b) the Deep Waterway Project (DWP). Positive values indicate seaward direction and negative landward. Black lines denote the isohaline, and the filled colour shows tidally averaged suspended sediment concentration.*

# 4.5. Discussion

## 4.5.1. Causes for enhanced estuarine circulation

Estuarine circulation was enhanced in the deepened and narrowed North Passage, particularly near the mouth (Figure 4-5a). The steady-state theory suggests that estuarine circulation is a function of channel depth ($H$), eddy viscosity ($K_M$) and along-channel salinity gradient ($\partial S/\partial x$) (Hansen and Rattray, 1965; MacCready and Geyer, 2010; Chant et al., 2018), as shown in Equation 4.12. Note that the $H$, $K_M$ and $\partial S/\partial x$ in Equation 4.12 are cross-sectionally and tidally averaged values, and cross-sectional averages are difficult to obtain from observations. Using the values observed in the main channel before and after the DWP, however, Equation 4.12 allows identifying the contributions of $H$, $K_M$ and $\partial S/\partial x$ to estuarine circulation (see Figure 4-9).

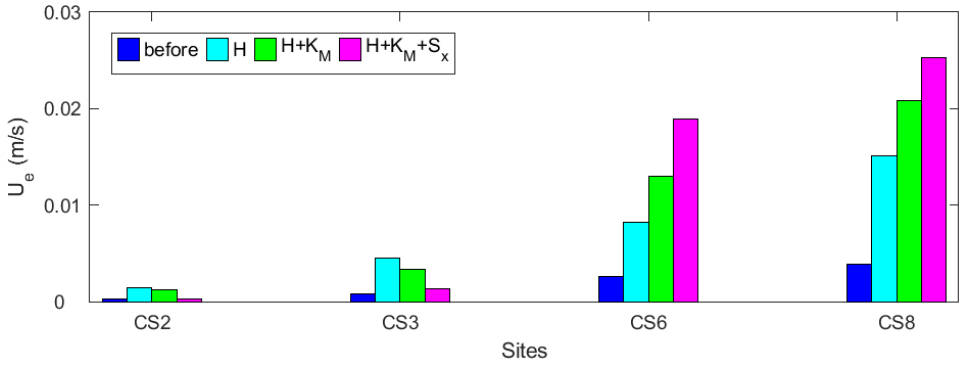


*Figure 4-9: The analysis of contributions of channel depth (H), eddy viscosity ($K_M$) and along-channel salinity gradient ($S_x$) to estuarine circulation ($U_e$) by Equation 4.12. The blue bars represent the estimates of the estuarine circulation ($U_e$) before the Deep Waterway Project (DWP), with H, $K_M$ and $S_x$ before the DWP as inputs. The cyan shows the estimates with $K_M$ and $S_x$ before the DWP and H after the DWP. The comparison between the blue and cyan indicates the effect of increased H on $U_e$. Similarly, the green and cyan comparison shows the contribution of changed $K_M$. The magenta denotes the estimates after the DWP, which, compared with the green, indicates the contribution of $S_x$ changes.*

Equation 4.12 suggests that estuarine circulation is highly sensitive to water depth because it scales with $H^3$. The magnitude of estuarine circulation is more than 3-fold, with a >50% increase in $H$ due to deepening (Figure 4-9). Nevertheless, channel deepening and narrowing may modify eddy viscosity and along-channel salinity gradient, both of which thus possibly alter the estuarine circulation. Including the eddy viscosity after the DWP, $U_e$ decreases in the upper reaches (CS2 and CS3)

but increases in the downstream (CS6 and CS8) (Figure 4-9). According to Equation 4.11, the eddy viscosity is determined by friction velocity ($u_*$) and Richardson number ($Ri$). The water column is well mixed in the upper reaches, with a low Richardson number (Figures 4-4j and 5b) and a low potential energy anomaly (Figure 4-6). Therefore, the eddy viscosity there is controlled primarily by $u_*$. Due to the narrowing (i.e., reducing estuary width), the flow is strengthened, increasing friction velocity and eddy viscosity (Figures 4-4k and 5c). It suggests that narrowing reduces estuarine circulation if its effect on the along-channel salinity gradient is negligible, for example, near the front of the salt wedge.

The increased $U_e$ related to eddy viscosity in the downstream reaches is attributed to enhanced stratification. Increased stratification (Richardson number) causes a reduction in eddy viscosity despite $u_*$ increases due to narrowing (Figures 4-4j, 4k, 5b and 5c). Deepening and narrowing are both responsible for enhanced stratification. First, narrowing increases the seaward flushing of fresh water, which overtops saltier water, thus increasing salinity stratification. Second, the salt intrusion is enhanced after deepening, particularly near the bottom, because the baroclinic (density) pressure gradient is proportional to water depth. As a result, saltier water intrudes beneath the fresher water, further enhancing salinity stratification.



In addition to the process along the channel, the narrowing can also increase the stratification through lateral processes. For example, the groyne fields trap saltwater during flood tides. During ebb tides, the water runs faster in the channel than on show shoals, producing significant lateral salinity gradients and circulation (Zhu et al., 2018; Zhou et al., 2019; Chen et al., 2020). This lateral circulation drives the salter water in the groyne fields to the main channel near the bed. This process, called lateral straining, enhances the stratification in the estuary (Zhu et al., 2018; Chen et al., 2020). Moreover, enhanced salinity stratification may suppress vertical mixing and confine sediment near the bottom, producing SSC gradients (i.e., sediment-induced stratification) (Winterwerp, 2002; Xu, 2009; Ge et al., 2018). This process may amplify the effect of stratification, resulting in a lower eddy viscosity and enhanced estuarine circulation.

The length of salt intrusion is expected to increase with deepening, resulting in a lower along-channel salinity gradient ($\partial S/\partial x$) (Hansen and Rattray, 1965; MacCready and Geyer, 2010; Ralston and Geyer, 2019). For example, in the Hudson Estuary, depth increases were even compensated by reduced $\partial S/\partial x$, and thus estuarine circulation did not significantly change after deepening (Ralston and Geyer, 2019). In the deepened and narrowed North Passage, however, $\partial S/\partial x$ decreased in the upper reaches (CS2 and CS3) but increased in the downstream (CS6 and CS8)

(Figure 4-5e). Correspondingly, including the $\partial S/\partial x$ after the DWP, $U_e$ decreases in the upper reaches but increases in the lower reaches (Figure 4-9). These results highlight the effect of narrowing (estuary width) on $\partial S/\partial x$. The North Passage was narrowed by dikes and the reclamation in groyne fields. Local structures (e.g., dikes and groynes) increase the form drag (roughness) experienced by the salt intrusion, suppressing the salt intrusion further upstream after the deepening (Song and Wang, 2013; Zhu et al., 2021b). As a result, the salt intrusion limit (or the salt intrusion length) had no significant changes, and the salinity (gradient) near the front of the salt wedge even decreased after the DWP (Figure 4-5d and e). The impacts of narrowing reduce downstream while that of deepening becomes predominant. Consequently, the salinity and gradient increased near the mouth, contributing to enhanced estuarine circulation.

Overall, near the salt wedge limit, the increase by deepening is compensated by the reduction by narrowing. However, the increase by narrowing is comparable to deepening near the mouth. Narrowing (estuary width) may thus have impacts as crucial as deepening (channel depth) on the estuarine circulation by modifying eddy viscosity and along-channel salinity gradient.



### 4.5.2. Sediment trapping by estuarine circulation

Our results show enhanced stratification and increased sediment import by estuarine circulation in the deepened and narrowed North Passage. Their interaction will be discussed in this section. First, from the view of sediment transport decomposition (see Equation 4.5), the stratification increases circulation-driven transport by enlarging vertical deviations of velocity ($u_0'$) and SSC ($c_0'$). The salinity and its vertical gradients in the middle reach of the North Passage (e.g., at CS6) increased after the DWP (Figure 4-4h). These increases suggest enhanced saltwater intrusion (see Zhu et al., 2006; Song et al., 2013). Meanwhile, high SSC and sediment stratification developed near the bottom after the DWP (Figure 4-4i). As a result, the gradient Richardson number (*Ri*) shows a notable increase, particularly near the surface and bottom (Figure 4-4j). The *Ri* was generally less than 0.25 before the DWP, but larger than 0.7 after the DWP, indicating enhanced stratification consistent with increased potential energy anomaly (see Figure 4-6). Intensified stratification inhibits turbulence and vertical mixing, reducing eddy viscosity and diffusivity (Figure 4-4k, see also Geyer, 1993). The bottom-surface differences (i.e., vertical deviations) of velocity and SSC increase due to the reduction in vertical mixing. Note that, near the bottom, $u_0'$ is negative while $c_0'$ is positive because of lower velocity and higher SSC. Therefore, enhanced stratification increases the sediment transport by estuarine circulation and produces negative (landward) net transport near the bottom.

Second, enhanced stratification induces concentrated benthic suspensions. These suspensions, driven by the near-bed inflow of estuarine circulation, produce significant sediment imports. Density stratification inhibits vertical mixing and confines sediment in the bottom layer, leading to sediment accumulation near the bed (Winterwerp, 2002; Xu, 2009; Ge et al., 2018). Accumulated sediment produces a notable vertical gradient of sediment concentration, enhancing stratification. With increasing SSC, hindered settling becomes important and favours the stability of concentrated benthic suspensions (Danker and Winterwerp, 2007; Dijkstra et al., 2018). With enhanced circulation (particularly increased inflows near the bottom), a notable sediment import is thus produced, leading to sediment convergence at the saltwater intrusion limit. This process is recognised as the primary mechanism controlling the sediment import in the deepened and narrowed North Passage, which is different from the Ems Estuary, where the sediment import is dominated by tidal pumping (Winterwerp, 2011; van Maren, et al., 2015; Dijkstra, et al., 2019).

### 4.5.3. Effect of stratification on tidal pumping



Apart from barotropic and estuarine circulation components, tidal pumping is the residual contribution to the net sediment transport, which results from the tidal covariance of flow velocity and SSC. Periodic stratification and internal asymmetry in eddy diffusivity can contribute to asymmetric sediment resuspension and tidal pumping (Scully and Friedrichs, 2007). Our results show that the stratification in the North Passage is a function of time (see Figure 4-6). Surprisingly, at CS8, a greater stratification develops during the early flood tide than during the late ebb (Figure 4-11b). Such an asymmetric stratification contrasts with the classic strain-induced periodic stratification in which stratification develops during the ebb tide and destroys during the flood tide (Simpson et al., 1990). Two processes are responsible for the unexpected stratification during the early flood tide: straining and near-bed sediment trapping.

First, during the early flood, the velocity profile with the maximum currents in the mid-lower water column results in reversed velocity shears (i.e., vertical velocity gradients) and enhanced salinity stratification (Figure 4-10f). After the DWP, increased seaward flushing of fresh water due to the decreased cross-section area accelerates ebbing flows but reduces flooding flows in the upper layers (Figure 4-2a, see also Zhao et al., 2018 and Zhu et al., 2019). As a result, ebb dominance increases near the surface. The maximum flooding velocity thus occurs in the middle layers instead of near the surface. During the early flood tide, the salter water near the bottom moves faster than the fresher water near the surface, producing a stronger stratification. Such a stratification induced by along-channel straining is

confirmed by the change rate of salinity-induced potential energy anomaly (Figure 4-11c).

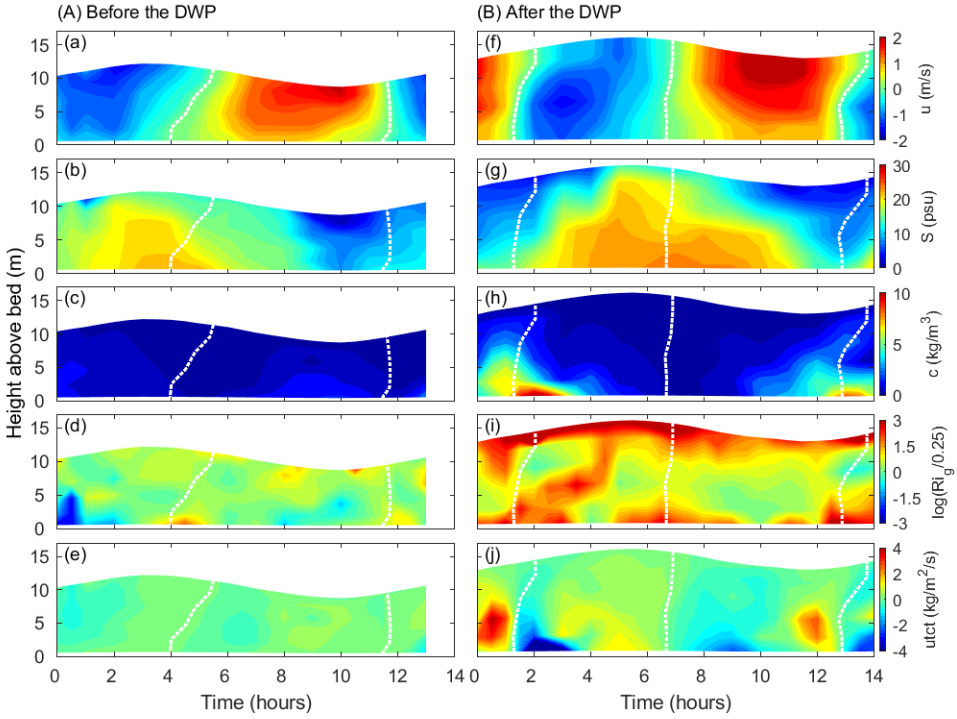


*Figure 4-10: Time-depth variations of (a) (f) along-channel velocities, (b) (g) salinity, (c) (h) suspended sediment concentrations, (d) (i) Richardson number and (e) (j) along-channel pumping at CS8 before (left panels) and after (right panels) the Deep Waterway Project (DWP). White lines represent zero velocity, and positive along-channel velocity indicates ebb tides.*

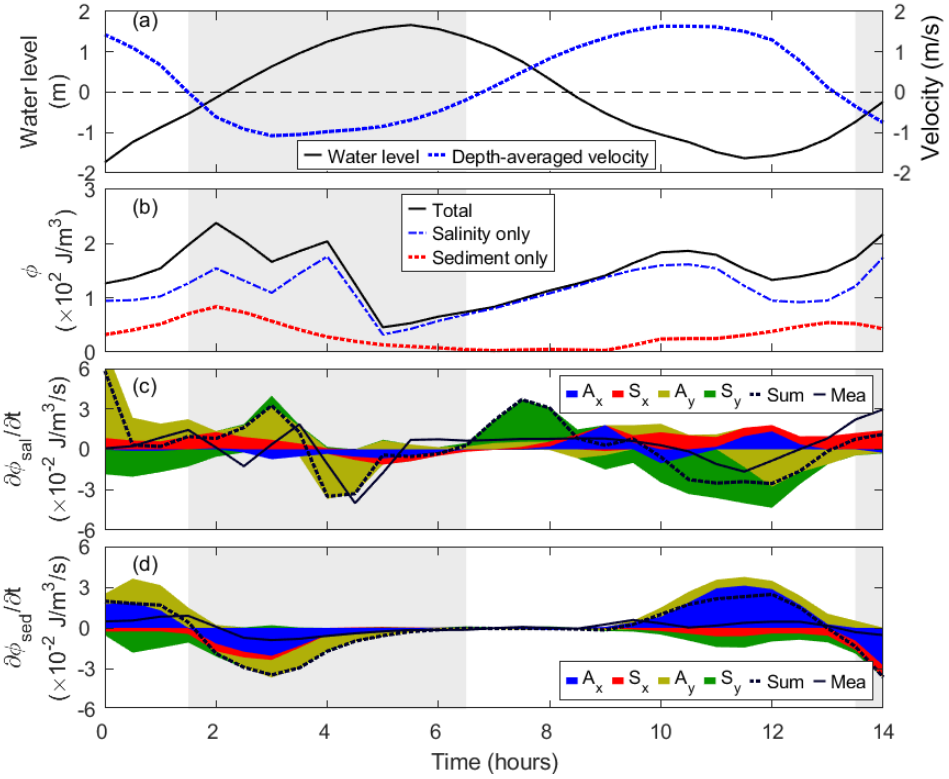


*Figure 4-11: Time series of (a) water level and depth-averaged velocity, (b) potential energy anomaly induced by salinity, sediment and their combination, (c) terms of the change rate of salinity-induced potential energy anomaly and (d) terms of the change rate of sediment-induced potential energy anomaly after the DWP. The areas are stacked. By adding the positive and negative areas at each step, one would get the calculated change rate of potential energy anomaly (dashed lines). The solid lines represent the measured change rate of potential energy anomaly by taking the time derivative of potential energy anomaly with a time step of 30 min. The grey shading denotes flood tides.*

Second, the stratification initialled by straining may trigger the positive feedback for near-bed sediment accumulation (Winterwerp, 2002; Xu, 2009; Ge et al., 2018). Strain-induced salinity stratification suppresses turbulence and vertical sediment mixing (i.e., sediment resuspension). As a result, sediment accumulates near the bottom (Geyer, 1993; Ge et al., 2018; Lin et al., 2021). Accumulated sediment causes hindered settling and produces strong SSC gradients, further enhancing density stratification and near-bed sediment accumulation (Winterwerp, 2002). Although no data is available to quantify the contribution of these vertical processes, the gap between the total change rate of $\phi_{sed}$ and the sum of straining and advection

terms highlights the importance of vertical mixing in sediment stratification (Figure 4-11d).

The asymmetric stratification (i.e., stronger stratification during early flood tides than during late ebb) results in the sediment import near the bottom and export in the middle water column. At CS8, for example, the relatively weak stratification during the late ebb allows sediment to be mixed higher up in the water column, returning lower near-bed SSC but higher mid-layer SSC than those during the early flood. In contrast, high SSC is confined near the bottom owing to the strong stratification during the early flood tide. Over a tidal cycle, such an asymmetric stratification leads to a landward flux near the bottom and a seaward flux in the middle layers (Figure 4-7b). Note that this transport pattern is site-specific, as the stratification is controlled by advection in the upstream and reversed shears (i.e., vertical velocity gradients) during flood tides are missing downstream.

### 4.5.4. ETM extension by tidal pumping

In addition to periodic stratification, tidal pumping is also related to velocity asymmetry, temporal lag, spatial lag and dispersive flux (Gatto et al., 2017). After the DWP, the tidal pumping was greatly enhanced, particularly in the middle reaches of the North Passage (Figure 4-7). This tidal pumping tends to redistribute the sediment trapped around the saltwater intrusion limit upstream and downstream. Spatial lag and dispersive flux are the two potential mechanisms for this sediment divergence. A profound flow velocity gradient is produced after the DWP. The flow velocity (hydrodynamic energy) is higher in the middle reaches (between CS4 and CS6) than in the upstream and downstream (Figure 4-4g). Spatial lag, interpreted as the transport asymmetry arising from the imbalanced velocity, produces the net transport from high- to low-energy areas (Friedrichs, 2011; Gatto et al., 2017).

Moreover, with the sediment trapping by estuarine circulation, the SSC increases in the middle North Passage, resulting in notable along-channel SSC gradients (Figure 4-8b). With such SSC gradients (up to 1.0 kg/m$^4$), the net transport by horizontal diffusion (i.e., net dispersive flux) becomes essential, although it is often negligible in tidal basins (Pritchard, 2005; Gatto et al., 2017). The net dispersive flux results in sediment transport from high- to low-SSC regions. Overall, spatial lag (velocity gradients) and dispersive flux (SSC gradients) are underlying mechanisms for landward or seaward transport by tidal pumping in the middle reaches of the North Passage. These processes are responsible for the extended ETM after the DWP.

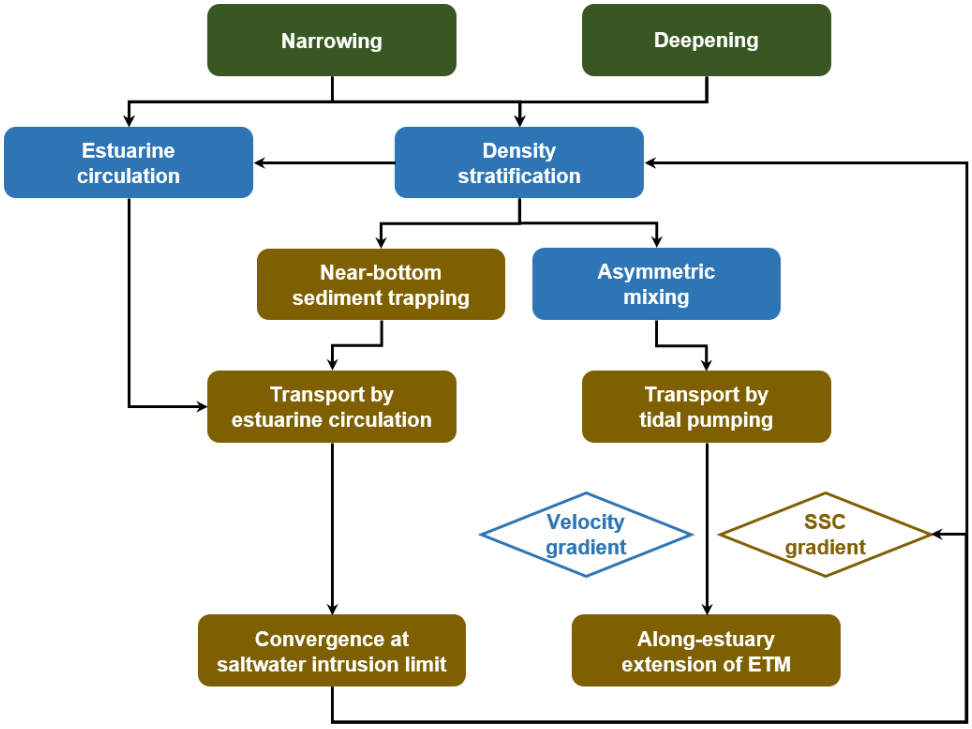


*Figure 4-12: Cause-consequence flow chart shows sediment transport changes and estuarine turbidity maximum (ETM) evolution in the deepened and narrowed North Passage.*

Figure 4-12 summarises the processes responsible for the concentrated and extended ETM in the deepened and narrowed North Passage. The lesson from the DWP is that narrowing (reduced estuary width) is not always conducive to the sediment export to seas, even in estuaries with a large Canter-Cremers number (i.e., the relative importance of river discharge and tide). We expected to increase the sediment flushing by narrowing at the very beginning of DWP. However, our results suggest that the narrowing increases the barotropic transport but leads to sediment import near the bottom due to enhanced estuarine circulation and stratification. In the North Passage, increased export may be compensated by increased circulation-driven import, resulting in sediment accumulation and intensive siltation. It implies that there is likely an optimal width that allows the maximum sediment export capacity in the estuary for a given water depth and river discharge. Width-controlled sediment transport was also found in tide-dominated estuaries, e.g., the Ems Estuary (van Maren, et al., 2016) and the North Branch (Guo et al., 2021). In these estuaries, narrowing (or reclamation) increases the sediment import by tidal pumping. We believe that a change in estuary width might substantially impact the sediment

import in other estuaries and channels worldwide, albeit that the responsible mechanism (estuarine circulation or tidal pumping) may differ.

## 4.6. Conclusions

This chapter revealed the roles of estuarine circulation and tidal pumping in the ETM evolution in response to deepening and narrowing and explored the effects of stratification on these processes in the North Passage of the Changjiang Estuary. Field data collected in June 1999 and August 2012 represent the conditions before and after the Deep Waterway Project (DWP), respectively.

Our results show that the deepened and narrowed North Passage enhanced estuarine circulation and stratification. Tidally averaged salinity-induced potential energy anomaly shows a 3-fold increase (up to 140 J/m$^3$). With near-bed sediment accumulation, sediment-induced stratification becomes essential. The tide-averaged sediment-induced potential energy anomaly after the completion of the DWP (up to 330 J/m$^3$) is 30-fold that before the DWP. It predominates the stratification around the saltwater intrusion limit, where the sediment from the river and the sea converges. Seaward residual currents near the surface increase up to 1.2 m/s, and landward flows near the bottom increase to 0.1 m/s, indicating an enhanced estuarine circulation. The increase in estuarine circulation ($U_e$) varies along the North Passage, with its maximum at CS6 and CS8, where $U_e$ is more than tripled (up to ~0.3 m/s). Both deepening and narrowing contribute to enhanced estuarine circulation. The narrowing alters the estuarine circulation by modifying density stratification and along-channel salinity gradient.

Sediment flux decomposition indicates that estuarine circulation controls the sediment import from seas and the sediment accumulation at the saltwater intrusion limit after the DWP. The enhanced stratification results in concentrated benthic suspensions. Near-bed high SSC, combined with increased landward residual currents, produces notable landward sediment transport. Such a sediment import meets fluvial sediment at the salt intrusion limit. Sediment convergence thus occurs, forming a concentrated ETM (with SSC up to 80 kg/m$^3$).

After the DWP, tidal pumping redistributes the accumulated sediment at the saltwater intrusion limit upstream and downstream, leading to an extended ETM. Along-estuary SSC gradients increase with the sediment trapping at the saltwater intrusion limit. In addition, along-estuary velocity gradients are profound after the DWP, with higher flow velocities (hydrodynamic energy) in the middle reaches (between CS4 and CS6) than in the upstream and downstream. Therefore, spatial lag (velocity gradients) and dispersive flux (SSC gradients) are underlying

mechanisms for the tidal pumping driving transport from high-SSC to low-SSC areas (i.e., ETM extension). These processes are responsible for the extended ETM after the DWP.

Moreover, a strain-enhanced stratification during the early flood was observed at CS8 after the DWP, different from the classic strain-induced periodic stratification (i.e., stratification develops during ebb tides and destroys during flood tides). The strain-enhanced stratification results from the reversed velocity shear with the maximum velocity in the mid-lower layers. Enhanced stratification increases near-bed SSC. These high sediment concentrations, coinciding with flood velocities, result in landward tidal pumping of sediment. Note that this transport is site-specific and relatively small compared to estuarine circulation.

# 5. Conclusions and Recommendations

*This thesis aims to improve the understanding of changing hydrodynamics and sediment dynamics in response to human interventions (e.g., channel deepening and narrowing). Three primary objectives are included: (1) to develop a method for measuring high sediment concentrations; (2) to identify and quantify the mechanisms responsible for the transport of fine sediment; (3) to understand how the engineering works modify the transport processes. To fulfil these three objectives, we present an example (the Changjiang Estuary) demonstrating the transition of a highly turbid estuary in response to deepening and narrowing based on field observations. The following section summarises the outcomes or feedback on these three objectives. In Section 5.2, a synthesis gives an overview of the changing hydrodynamics and sediment dynamics in the deepened and narrowed Changjiang Estuary. Section 5.3 discusses the implications of the main findings in this thesis for other systems. Finally, recommendations and an outlook for future open research questions are given in Section 5.4.*

## 5.1. Responses to objectives

**(1) Develop a method for measuring high sediment concentrations**

Accessing accurate sediment concentrations in highly turbid environments by optical or acoustic sensors has been a problem due to signal saturation and attenuation. The saturation returns a limited measurement range, e.g., Argus Suspension Meter (ASM) only provides estimates of sediment concentrations <9 g/L. The attenuation of optical or acoustic signal raises an ambiguity problem, as a low (optical or acoustic) output could mean a low or high sediment concentration, e.g., the output of Optical Backscatter Sensor (OBS) decreases when sediment concentration >10 g/L and Acoustic Doppler Velocimeter (ADV) when sediment concentration >2 g/L.

Based on the different responses of ASM, OBS and ADV, an integrated optical and acoustic (IOA) approach is proposed to (i) overcome the ambiguity problem, (ii) access a broader measurement range, and (iii) obtain high-resolution profiles of sediment concentration (**Chapter 2**). ASM-derived sediment concentrations are preferred in this approach because of the lowest relative error (~25%). When the ASM is unsaturated, it can also provide high-resolution (1 cm interval) sediment concentration profiles. When the ASM is saturated, the OBS recover the estimate, with a relative error of ~30%. Since the ambiguity problem is solved by combining optical or acoustic sensors, the measurement range can be extended to >100 g/L. The best way to use the ADV is to have a rough estimation and assist in the OBS conversion, as its estimates contain significant uncertainty (relative error >80%). In-situ water samples for sensor calibrations are suggested further to mitigate the impact of grain size on the retrieval.

The IOA approach successfully captured and measured the concentrated benthic suspensions (>10 g/L) in the Changjiang Estuary. The comparison between estimates from the IOA approach and in-situ water samples indicates the reliability of the IOA approach with relative errors of 17–34%. The observed near-bed sediment concentration was up to 63 g/L. The sediment concentration profiles in the Changjiang Estuary exhibit notable seasonal variations. High sediment concentrations were confined in the benthic layer (within 2 m above the bed) in the wet season, whereas the suspension was mixed throughout the water column in the dry season, resulting in a more uniform and nearly linear profile.

**(2) Identify and quantify the mechanisms responsible for the transport of fine sediment**

Observations in the Changjiang Estuary from 1988 to 2015 were collected and analysed to identify the transition in vertical suspended sediment concentration profiles (**Chapter 3**). During this period, the fluvial sediment load from the Changjiang River decreased by ~70% (at Datong), while the annual river discharge was relatively stable. Meanwhile, a deep-water navigation channel was built in the North Passage of the Changjiang Estuary. As a result, the water depth of the channel increased from 6.5 m to 12.5 m. In addition, the estuary was narrowed to strengthen the flow, which was expected to increase sediment flushing and reduce siltation.

The results indicate decreasing sediment concentrations in the upper water column and increasing concentrations near the bottom. The increase in near-bed sediment concentration is attributed to estuarine engineering works (e.g., deepening and narrowing) and the interaction between stratification, turbulence damping and hindered settling. Estuarine density stratification is strengthened due to the deepening and narrowing (**Chapter 4**). Enhanced stratification triggers the positive feedback among stratification, turbulence damping and hindered settling (**Chapter 3**). As a consequence of enhanced stratification, eddy viscosity and diffusivity reduce (i.e., turbulence damping). Vertical sediment entrainment to the upper water column is therefore suppressed, and hence sediment tends to be trapped near the bottom. Near-bed sediment concentrations thus increase. With increasing sediment concentration, hindered settling becomes important. It allows trapped sediment to keep in suspension and produces significant vertical gradients of suspended sediment concentration (i.e., sediment-induced stratification) near the bottom, further enhancing stratification. Such a positive feedback loop favours the stability of concentrated benthic suspensions.



However, two processes are responsible for decreasing sediment concentrations in the upper water column (**Chapter 3**). First, the enhanced stratification and consequent positive feedback inhibit the vertical mixing and sediment entrainment to the higher water column. Second, declined fluvial sediment supply reduces the sediment availability in the estuary. For example, the annual sediment load of the Changjiang River decreased by about 70% (1985-2015), while the annual river discharge barely changed. It suggests that the freshwater with lower sediment concentrations is delivered to the estuary, diluting the sediment concentrations near the water surface.

The integrated bottom-mounted tripod system measured the drag reduction in response to suspended sediment concentration (**Chapter 3**). The drag/friction coefficient reduces with increasing concentrations of suspended sediments when sediment concentrations are less than 10 g/L and maintains at its minimum (with a drag reduction of 60%) in concentrated benthic suspensions (10-80 g/L). The drag

reduction predominately results from turbulence damping, and the drag increases because of increasing viscous stress at higher concentrations. Once concentrated benthic suspensions develop, turbulence damping and viscous stress are of comparable importance, resulting in a minimum drag coefficient that is almost constant. The friction experienced by water motion significantly reduces, while the bed stress for erosion maintains as high as in a low-concentration state. Hence, in addition to hindered settling (Dijkstra et al., 2018), increased viscous stress supports accumulated sediment in suspension. This finding supports the hypothesis by Dijkstra et al. (2019) that drag reduction has a negligible effect on erosion in a hyper-turbid state.

Hindered settling and increased viscous stress allow the trapped sediment to keep in suspension, while enhanced stratification and turbulence damping inhibit the entrainment to the higher water column. As a result, sediment accumulates near the bottom, generating concentrated benthic suspensions (10-80 g/L) and fluid mud (>80 g/L). With enough sediment supply from the river or the sea, the concentrated benthic suspensions and fluid mud can further develop, i.e., the thickening of concentrated benthic suspension and fluid mud layers. A mobile pool of concentrated benthic suspensions was observed in the North Passage of the Changjiang Estuary after the deepening and narrowing (**Chapter 3**). It has a tidally averaged length of ~20 km and a mean thickness of ~4 m. Concentrated benthic suspensions and fluid mud were also observed in estuaries that have undergone the regime shift from low- to hyper-turbid state (e.g., the Ems Estuary (Winterwerp et al., 2017)). They are expected to develop in other deepened estuaries, e.g., the Hudson Estuary and the Seine Estuary.



**(3) Determine how the engineering works modify the transport processes**

To improve the understanding of how estuarine turbidity maximum evolutes in response to the engineering works, we reveal the hydrodynamics (e.g., estuarine circulation and stratification) and sediment transport (residual flux) changes in the deepened and narrowed North Passage (**Chapter 4**). The results show that both estuarine circulation and stratification are enhanced after the deepening and narrowing. In addition, sediment-induced stratification becomes essential near the saltwater intrusion limit, where riverine and marine sediments converge.

The steady-state theory suggests that the estuarine circulation is a function of depth ($H$), along-estuary salinity gradient ($\partial S/\partial x$) and eddy viscosity ($K_M$) (Hansen and Rattray, 1965; MacCready and Geyer, 2010; Chant et al., 2018). Since the estuarine circulation scales with $H^3$, deepening (i.e., increased $H$) is generally considered as the leading cause for enhanced estuarine circulation. Our results argue that

narrowing (estuary width) may contribute as crucial as deepening (channel depth) to the estuarine circulation by modifying eddy viscosity and along-channel salinity gradient. An increasing salt intrusion length is expected with deepening, resulting in a lower along-channel salinity gradient ($\partial S/\partial x$) (Hansen and Rattray, 1965; MacCready and Geyer, 2010; Ralston and Geyer, 2019). For example, in the Hudson Estuary, depth increases were even compensated by reduced $\partial S/\partial x$, and hence the estuarine circulation was barely changed by deepening (Ralston and Geyer, 2019). In the deepened and narrowed North Passage, however, narrowing inhibited the salt intrusion by increasing (dike-induced) form drag and strengthened the seaward flushing of fresh water. As a result, $\partial S/\partial x$ decreased in the upper North Passage but increased downstream. In addition, the narrowing also contributes to enhanced stratification and hence reduced eddy viscosity. Our analysis shows that the increase in ($\partial S/\partial x$) and the reduction in $K_M$ are comparable to depth increases. It implies that estuary width plays a role as vital as channel depth in estuarine circulation by modifying eddy viscosity and along-channel salinity gradient.

The local sediment flux decomposition indicates that the sediment transport by estuarine circulation and tidal pumping play different roles in the evolution of estuarine turbidity maximum in the North Passage (**Chapter 4**). The estuarine circulation controls the sediment import from the sea and the sediment accumulation at the saltwater intrusion limit. After the deepening and narrowing, the enhanced stratification results in concentrated benthic suspensions (**Chapter 3**). Near-bed high sediment concentrations, driven by increased estuarine circulation inflows, produce significant landward sediment transport near the bottom. Such a sediment import meets fluvial sediment at the salt intrusion limit. Thus, sediment convergence occurs, forming a concentrated estuarine turbidity maximum (with a sediment concentration of up to 80 kg/m$^3$).



However, the tidal pumping redistributes the sediment accumulated at the saltwater intrusion limit upstream and downstream, resulting in an extended estuarine turbidity maximum. Consequently, the sediment accumulation at the saltwater intrusion limit increases along-estuary sediment concentration gradients. In addition, along-estuary velocity gradients are profound after the Deep Waterway Project, with higher flow velocities (hydrodynamic energy) in the middle North Passage than in the upstream and downstream. Therefore, spatial lag (velocity gradients) and dispersive flux (sediment concentration gradients) are the underlying mechanisms for the tidal pumping driving sediment from high-energy (or high sediment concentration) to low-energy (or low sediment concentration) areas, leading to the along-estuary extension of estuarine turbidity maximum.

Overall, in estuaries with a large river discharge (e.g., the Changjiang Estuary), the sediment import/trapping is primarily controlled by estuarine circulation, while tidal pumping is responsible for the extension of estuarine turbidity maximum. The roles of these processes are different from those in tidal estuaries, e.g., the Ems Estuary, where the sediment import is primarily controlled by tidal pumping (Winterwerp, 2011; Dijkstra et al., 2019). The evolution of estuarine turbidity maximum (i.e., increasing near-bed sediment concentration and along-estuary extension) observed in the North Passage is expected to develop in other river-dominated estuaries, e.g., the Mississippi, if it is deepened or narrowed.

## 5.2. A synthesis

Although section 5.1 gives detailed insights into each initial objective, a summary is required for a comprehensive understanding of the transition of the whole system. Therefore, this section synthesises the changes in hydrodynamics and sediment dynamics in response to deepening, narrowing and declined fluvial sediment supply in a river- and tide-dominated estuary (see Figure 5-1).

As a result of deepening and narrowing, both density stratification and estuarine circulation are strengthened. Enhanced stratification triggers the positive feedback between vertical mixing and hindered settling, resulting in near-bed sediment accumulation and concentrated benthic suspensions. These concentrated benthic suspensions, driven by increased landward flows (the lower part of estuarine circulation), produce a sediment convergence at the saltwater intrusion limit. As a result, near-bed sediment concentrations of the estuarine turbidity maximum increase. However, the sediment concentrations in the upper water column decrease due to reduced sediment resuspension (by turbulence damping) and fluvial sediment supply. Hindered settling and viscous stress become important with increasing near-bed sediment concentrations, allowing accumulated sediment to keep in suspension. In addition, the friction experienced by water motion reduces (i.e., drag reduction), resulting in tidal amplification.

Furthermore, the sediment convergence at the saltwater intrusion limit (by estuarine circulation) increases along-estuary gradients of sediment concentrations. Therefore, the contribution of tidal pumping becomes vital, driving the accumulated sediment upstream and downstream. Consequently, an extended estuarine turbidity maximum develops. Overall, after deepening and narrowing, concentrated benthic suspensions and a longitudinally extended ETM are expected to develop in estuaries with a large river discharge.

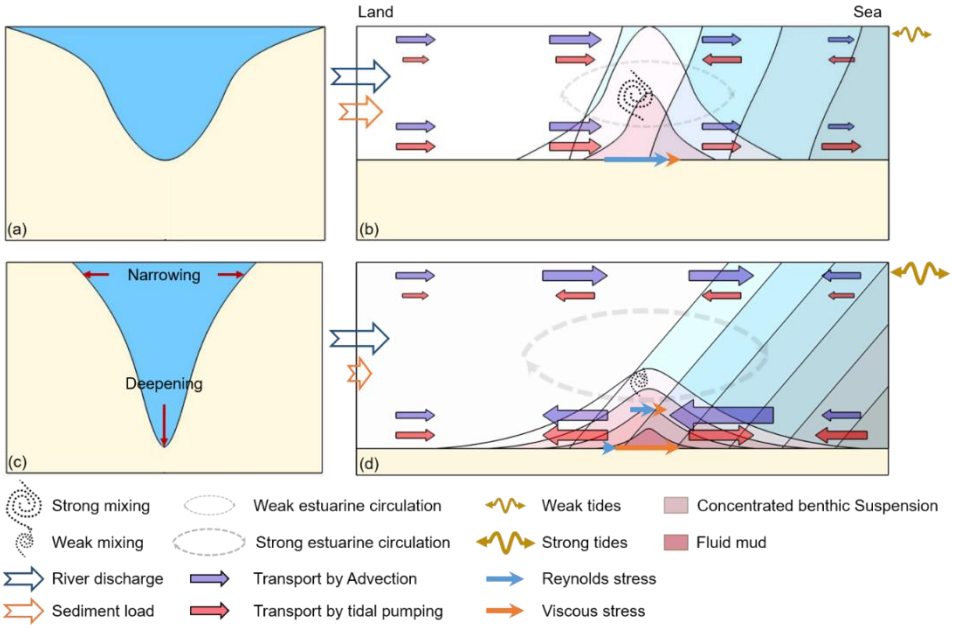


*Figure 5-1: (a) (c) Cross-section and (b) (d) along-channel schematic of bathymetry, hydrodynamics and sediment dynamics before (upper panels) and after (lower panels) deepening and narrowing in a river- and tide-dominated estuary.*



## 5.3. Applications

This section summarises the practical applications of the results and findings in this thesis.

**(1) Measuring sediment concentration**

An integrated optic and acoustic (IOA) approach is suggested in this thesis to access reliable measurements of sediment concentrations in highly turbid environments. Since the ambiguity problem in signal conversion is resolved by combining optical and acoustic sensors, this approach increases the measurement range to high sediment concentrations (>60 g/L). Therefore, the IOA approach is expected to be applied in environments with large spatial (e.g., estuarine turbidity maximum zone) or temporal (e.g., during storms) variabilities of sediment concentrations. For example, during a storm, the conventional method (i.e., single usage of the optical or acoustic sensor) may underestimate the sediment concentration due to the signal attenuation in high sediment concentrations, so the sediment dynamics (e.g., erosion, deposition and sediment transport) could be misinterpreted. The IOA

approach, however, can avoid these errors and obtain accurate sediment concentrations by the mutual correction between optical and acoustic sensors. This approach thus helps to improve our understanding of the sediment dynamics in the bottom boundary layer or during an extreme event.

**(2) Construction and management strategies**

The movements of the CBS pool, combined with the tidal asymmetry (e.g., slack-water asymmetry and lateral flow asymmetry), indicate the locations of sediment trapping and siltation in an estuary. In the North Passage, for example, the slack-water asymmetry suggests a longer slack (when the bed stress is lower than the critical stress for erosion) after high water than after low water. Much more sediment thus settles from the CBS to the bed during the high-water slack (in the middle reaches) than during the low-water slack (in the lower reaches). Moreover, the longer slack favours the consolidation of deposited sediment, which increases the critical stress for erosion and thus reduces the sediment resuspension during subsequent tidal acceleration. As a result, much more intensive silation occurs in the middle than in the lower North Passage. This along-channel asymmetry in silation could be amplified if high-concentration-induced drag reduction and the salinity effect on floc settling are considered. In addition, lateral density gradients and the curvature lead to the lateral flow asymmetry in the North Passage (Chen and de Swart, 2018; Zhu et al., 2018; Zhou et al., 2019), by which the CBS pool tends to move to the south flank of the channel, especially when the deposition occurs. More intensive deposition thus occurs on the south than on the north flank of the channel. Overall, the mobile CBS pool, driven by the asymmetries of slack water and lateral flows, indicates an intensive siltation region in the middle reaches and on the south flank of the North Passage, which is of great significance to the design of dredging and dumping area.

The Deep Waterway Project (DWP) was expected to increase the seaward sediment flushing and export by narrowing the estuary. In fact, the narrowing only increases the sediment export driven by river discharge (i.e., barotropic flux) but leads to near-bed sediment import by enhancing estuarine circulation and stratification. Increased stratification leads to near-bed sediment trapping and concentrated benthic suspensions. These highly concentrated suspensions, driven by the increased near-bed inflows of estuarine circulation, produces significant sediment import. This sediment transport may compensate or exceed the export by barotropic flux, leading to sediment convergence at the saltwater intrusion limit. Our analysis suggests that narrowing (estuary width) is vital as deepening (channel depth) to estuarine circulation and stratification. Therefore, the lesson from the DWP is that narrowing does not always benefit the sediment export to the sea, even in estuaries with large

river discharges. An optimal width likely allows the maximum sediment export capacity for a given water depth and river discharge. Width-controlled sediment transport was also found in tide-dominated estuaries, e.g., the Ems Estuary (van Maren et al., 2016) and the North Branch (Guo et al., 2021). The narrowing (by reclamation) increases the sediment import by tidal pumping in these estuaries. We believe that estuary width is a critical factor determining sediment import in other estuaries and channels worldwide, although the responsible mechanism may differ.

## 5.4. Recommendations

The IOA approach affordably provides more information about sediment dynamics, e.g., turbulent sediment flux (Lin et al., 2020) and sediment composition (Pearson et al., 2021). Recently, Pearson et al. (2021) proposed a sediment composition index based on the relative optical and acoustic backscatter. With this index, one can estimate the fraction of sand and mud in suspensions. Combined with the flow velocity measured synchronously, one can further quantify the fluxes of sand and mud. Therefore, the IOA approach can improve the understanding of sediment dynamics in coastal and estuarine environments. To date, however, the sediment composition index is only tested and validated within low sediment concentrations (<2 g/L) (Pearson et al., 2021). It is expected to be extended and applied in high-concentration environments, improving our understanding of the transport of sand and mud in high-turbid environments.



Our results suggest that narrowing (estuary width) has crucial impacts on estuarine circulation, stratification, and sediment transport. An optimal estuary width is likely to allow the most efficient sediment export to the sea for a given river discharge and water depth. Yet, the optimal estuary width or its function is not clear. The total sediment transport in estuaries is a sum of the transport by barotropic flux, estuarine circulation and tidal pumping. In a river- and tide-dominated estuary (e.g., the North Passage), estuarine circulation dominates the sediment import from the sea and depends on river discharge and estuary width (this thesis). In tide-dominated estuaries, the sediment import is primarily controlled by tidal pumping determined by tide conditions (e.g., tidal asymmetries in velocity and ebb/flood duration) (Winterwerp et al., 2017). It implies that the optimal estuary width is probably a function of river discharge and tides for a given water depth. In the future, an idealised model is recommended to access the exact function of the optimal estuary width. This function will help design engineering works and the management of estuaries.

A transition in vertical sediment concentration profile was observed in the deepened and narrowed North Passage, with increasing concentrations near the bottom and

decreasing in the upper water column. The vertical sediment concentration profile is a function of (friction) velocity, eddy diffusivity and settling velocity. The (friction) velocity is determined by river discharge, tides and bathymetry, while the eddy diffusivity depends on stratification and the settling velocity on particle size and sediment concentration. Strong stratification suppresses turbulence and inhibits the sediment suspension from higher up in the water column. Hence, the surface concentration of a strongly stratified estuary is less likely to increase than that of well-mixed estuaries. It implies that well-mixed (tide-dominated) estuaries are at a higher risk of hyper-turbid states throughout the water column than strongly stratified estuaries (with large river discharge). This idea is still a hypothesis, and it is recommended to test it by numerical models.

# Appendix A. Field measurements used in this thesis

*Table A-A1: Information about the measurements used in this thesis*

| Time | Locations | Measurements | Sources/Contributors | References |
|---|---|---|---|---|
| Jul. 2014* | CS4 | Velocity, salinity, SSC, FSD, PPSD profiles<br>Near-bed velocity, salinity and SSC | SKLEC, Qing He's group | Guo et al. (2017) |
| Jan. 2016* | CS4 | Velocity, salinity, SSC, FSD, PPSD profiles<br>Near-bed velocity, salinity and SSC | SKLEC, Qing He's group | |
| 1986, 1997, 2002, 2007, 2010 | Changjiang Estuary | Bathymetry | Shanghai Dredging Corporation, Ministry of Transport of China | Zhu et al. (2019) |
| 2013, 2016 | Changjiang Estuary | Bathymetry | Navigation Guarantee Department of Chinese Navy Headquarters | Zhu et al. (2019) |
| August, 1988 | CS4 | SSC profiles | SKLEC, Jiyu Chen | |
| Jun. 1999, Aug. 2005, Aug. 2009, Aug. 2012 | CS4 | SSC profiles | Yangtze Estuary Waterway Administration Bureau | |
| Aug. 2015* | CS4 | SSC profiles | SKLEC, Qing He's group | |
| Jun. 1999 | CS2, CS3, CS6, CS8 | velocity, salinity, SSC profiles | Yangtze Estuary Waterway Administration Bureau | Wan (2015) |
| Aug. 2012 | CS1-9, CS6s, CS6n | velocity, salinity, SSC profiles | Yangtze Estuary Waterway Administration Bureau | Wan (2015) |

SSC denotes suspended sediment concentration. FSD and PPSD stand for flocculate and primary particle size distribution, respectively. The symbol * indicates the filed work in which the author was involved. The locations of observation stations refer to Figure 4.1.

# References

Allen, G.P., Salomon, J.C., Bassoullet, P., Du Penhoat, Y., De Grandpre, C., 1980. Effects of tides on mixing and suspended sediment transport in macrotidal estuaries. Sediment. Geol. 26, 69–90. https://doi.org/10.1016/0037-0738(80)90006-8

Anastasiou, S., Sylaios, G.K., Tsihrintzis, V.A., 2015. Suspended particulate matter estimates using optical and acoustic sensors: Application in Nestos River plume (Thracian Sea, North Aegean Sea). Environ. Monit. Assess. 187, 392. https://doi.org/10.1007/s10661-015-4599-y

Argus, 2014. User Manual: Argus Suspension Meter V., http://argusnet.de/wp-content/uploads/2016/12/asm_V_reference.pdf.

Baeye, M., Fettweis, M., 2015. In situ observations of suspended particulate matter plumes at an offshore wind farm, southern North Sea. Geo-Marine Lett. 35, 247–255. https://doi.org/10.1007/s00367-015-0404-8

Becherer, J., Flöser, G., Umlauf, L., Burchard, H., 2016. Estuarine circulation versus tidal pumping: Sediment transport in a well-mixed tidal inlet. J. Geophys. Res. Ocean. 121, 6251–6270. https://doi.org/10.1002/2016JC011640

Becherer, J., Stacey, M.T., Burchard, H., Umlauf, L., 2015. Lateral circulation generates flood tide stratification and estuarine cxchange flow in a curved tidal inlet. J. Phys. Oceanogr. 45, 638–656. https://doi.org/10.1175/JPO-D-14-0001.1

Becker, M., Maushake, C., Winter, C., 2018. Observations of mud-induced periodic stratification in a hyperturbid estuary. Geophys. Res. Lett. 45, 5461–5469. https://doi.org/10.1029/2018GL077966

Besset, M., Anthony, E.J., Bouchette, F., 2019. Multi-decadal variations in delta shorelines and their relationship to river sediment supply: An assessment and review. Earth-Science Rev. 1993, 199–219. https://doi.org/10.1016/j.earscirev.2019.04.018

Bianchi, T.S., 2006. Biogeochemistry of Estuaries. Oxford Univ. Press, Oxford, UK.

Brown, C.J., Saunders, M.I., Possingham, H.P., Richardson, A.J., 2013. Managing for interactions between local and global stressors of ecosystems. PLoS One 8, E65765. https://doi.org/10.1371/journal.pone.0065765

Bruens, A.W., Winterwerp, J.C., Kranenburg, C., 2012. Physical and numerical modeling of the entrainment by a high-concentration mud suspension. J. Hydraul. Eng. 138, 479–490. https://doi.org/10.1061/(ASCE)HY.1943-7900.0000545

Burchard, H., Baumert, H., 1998. The formation of estuarine turbidity maxima due to density effects in the salt wedge: A hydrodynamic process study. J. Phys. Oceanogr. 28, 309–321.

Burchard, H., Hetland, R.D., 2010. Quantifying the contributions of tidal straining and gravitational circulation to residual circulation in periodically stratified tidal estuaries. J. Phys. Oceanogr. 40, 1243–1262. https://doi.org/10.1175/2010JPO4270.1

Burchard, H., Hetland, R.D., Schulz, E., Schuttelaars, H.M., 2011. Drivers of residual estuarine circulation in tidally energetic estuaries: Straight and irrotational channels with parabolic cross section. J. Phys. Oceanogr. 41, 548–570. https://doi.org/10.1175/2010JPO4453.1

Burchard, H., Hofmeister, R., 2008. A dynamic equation for the potential energy anomaly for analysing mixing and stratification in estuaries and coastal seas. Estuar. Coast. Shelf Sci. 77, 679–687. https://doi.org/10.1016/j.ecss.2007.10.025

Burchard, H., Schuttelaars, H.M., 2012. Analysis of tidal straining as driver for estuarine circulation in well-mixed estuaries. J. Phys. Oceanogr. 42, 261–271. https://doi.org/10.1175/JPO-D-11-0110.1

Burchard, H., Schuttelaars, H.M., Geyer, W.R., 2013. Residual sediment fluxes in weakly-to-periodically stratified estuaries and tidal inlets. J. Phys. Oceanogr. 43, 1841–1861. https://doi.org/10.1175/JPO-D-12-0231.1

Burchard, H., Schuttelaars, H.M., Ralston, D.K., 2018. Sediment trapping in estuaries. Ann. Rev. Mar. Sci. 10, 371–395. https://doi.org/10.1146/annurev-marine-010816-060535

Cai, H., Savenije, H.H.G., Toffolon, M., 2012. A new analytical framework for assessing the effect of sea-level rise and dredging on tidal damping in estuaries. J. Geophys. Res. Ocean. 117, C09023. https://doi.org/10.1029/2012JC008000

Cai, W.J., Feely, R.A., Testa, J.M., Li, M., Evans, W., Alin, S.R., Xu, Y.Y., Pelletier, G., Ahmed, A., Greeley, D.J., Newton, J.A., Bednarscaronek, N., 2021. Natural and anthropogenic drivers of acidification in large estuaries. Ann. Rev. Mar. Sci. 13, 19.1-19.33. https://doi.org/10.1146/annurev-marine-010419-011004

Cameron W.M., Pritchard D.W., 1963. Estuaries, in: Hill M.N. (Ed.), the Sea. Interscience, New York, vol 2, pp. 306–324.

Campbell Scientific, I., 2018. Operator's Manual: OBS-3A Turbidity and Temperature Monitoring System. https://s.campbellsci.com/documents/us/manuals/obs-3a.pdf.

Campbell, C.G., Laycak, D.T., Hoppes, W., Tran, N.T., Shi, F.G., 2005. High concentration suspended sediment measurements using a continuous fiber optic in-stream transmissometer. J. Hydrol. 311, 244–253.

https://doi.org/10.1016/j.jhydrol.2005.01.026

Canuel, E.A., Hardison, A.K., 2016. Sources, ages, and alteration of organic matter in estuaries. Ann. Rev. Mar. Sci. 8, 15.1-15.26. https://doi.org/10.1146/annurev-marine-122414-034058

Cellino, M., Graf, W.H., 1999. Sediment-laden flow in open-channels under noncapacity and capacity conditions. J. Hydraul. Eng. 125, 455–462.

Chanson, H., Trevethan, M., Aoki, S., 2008. Acoustic Doppler velocimetry (ADV) in small estuary: Field experience and signal post-processing. Flow Meas. Instrum. 19, 307–313. https://doi.org/10.1016/j.flowmeasinst.2008.03.003

Chant, R.J., Sommerfield, C.K., Talke, S.A., 2018. Impact of channel deepening on tidal and gravitational circulation in a highly engineered estuarine basin. Estuaries and Coasts 41, 1587–1600. https://doi.org/10.1007/s12237-018-0379-6

Chen, W., de Swart, H.E., 2018. Longitudinal variation in lateral trapping of fine sediment in tidal estuaries: Observations and a 3D exploratory model. Ocean Dyn. 68, 309–326. https://doi.org/10.1007/s10236-018-1134-z

Chen, Y., He, Q., Shen, J., Du, J., 2020. The alteration of lateral circulation under the influence of human activities in a multiple channel system, Changjiang Estuary. Estuar. Coast. Shelf Sci. 242, 106823. https://doi.org/10.1016/j.ecss.2020.106823

Cheng, N.-S., 2015. Representative grain size and equivalent roughness height of a sediment bed. J. Hydraul. Eng. 123, 149–152. https://doi.org/10.1061/(ASCE)HY.1943-7900.0001069

Chernetsky, A.S., Schuttelaars, H.M., Talke, S.A., 2010. The effect of tidal asymmetry and temporal settling lag on sediment trapping in tidal estuaries. Ocean Dyn. 60, 1219–1241. https://doi.org/10.1007/s10236-010-0329-8

China Water Resources Ministry (CWRM), 2015. River sediment bulletin of China 2014. Water Publication Press, Beijing, China. http://www.mwr.gov.cn/sj/tjgb/zghlnsgb

Chow V.T., 1959. Open channel hydraulics. McGraw-Hill Book Company, New York.

Cloern, J.E., Foster, S.Q., Kleckner, A.E., 2014. Phytoplankton primary production in the world's estuarine-coastal ecosystems. Biogeosciences 11, 2477–2501. https://doi.org/10.5194/bg-11-2477-2014

Conner, C.S., De Visser, A.M., 1992. A laboratory investigation of particle size effects on an optical backscatterance sensor. Mar. Geol. 108, 151–159. https://doi.org/10.1016/0025-3227(92)90169-I

Dalrymple, R.W., Zaitlin, B.A., Boyd, R., 1992. Estuarine facies models: Conceptual basis and stratigraphic implications. J. Sediment. Petrol. 62, 1130–1146.

Dankers, P.J.T., Winterwerp, J.C., 2007. Hindered settling of mud flocs: Theory and validation. Cont. Shelf Res. 27, 1893–1907. https://doi.org/10.1016/j.csr.2007.03.005

de Boer, G.J., Pietrzak, J.D., Winterwerp, J.C., 2008. Using the potential energy anomaly equation to investigate tidal straining and advection of stratification in a region of freshwater influence. Ocean Model. 22, 1–11. https://doi.org/10.1016/j.ocemod.2007.12.003

de Jonge, V.N., 1992. Tidal flow and residual flow in the Ems estuary. Estuar. Coast. Shelf Sci. 34, 1–22. https://doi.org/10.1016/S0272-7714(05)80123-4

de Jonge, V.N., Schuttelaars, H.M., van Beusekom, J.E.E., Talke, S.A., de Swart, H.E., 2014. The influence of channel deepening on estuarine turbidity levels and dynamics, as exemplified by the Ems estuary. Estuar. Coast. Shelf Sci. 139, 46–59. https://doi.org/10.1016/j.ecss.2013.12.030

de Nijs, M.A.J., 2012. On sedimentation processes in a stratified estuarine system. Ph.D. thesis. Delft University of Technology.

Deng, Z., He, Q., Safar, Z., Chassagne, C., 2019. The role of algae in fine sediment flocculation: In-situ and laboratory measurements. Mar. Geol. 413, 71–84. https://doi.org/10.1016/j.margeo.2019.02.003

Dijkstra, Y.M., Schuttelaars, H.M., Burchard, H., 2017. Generation of exchange flows in estuaries by tidal and gravitational eddy viscosity-shear covariance (ESCO). J. Geophys. Res. Ocean. 122, 4217–4237. https://doi.org/10.1002/2016JC012379

Dijkstra, Y.M., Schuttelaars, H.M., Schramkowski, G.P., Brouwer, R.L., 2019. Modeling the transition to high sediment concentrations as a response to channel deepening in the Ems River Estuary. J. Geophys. Res. Ocean. 124, 1578–1594. https://doi.org/10.1029/2018JC014367

Dijkstra, Y.M., Schuttelaars, H.M., Winterwerp, J.C., 2018. The hyperturbid state of the water column in estuaries and rivers: The importance of hindered settling. Ocean Dyn. 68, 377–389. https://doi.org/10.1007/s10236-018-1132-1

Downing, J., 2006. Twenty-five years with OBS sensors: The good, the bad, and the ugly. Cont. Shelf Res. 26, 2299–2318. https://doi.org/10.1016/j.csr.2006.07.018

Druine, F., Verney, R., Deloffre, J., Lemoine, J.-P., Chapalain, M., Landemaine, V., Lafite, R., 2018. In situ high frequency long term measurements of suspended sediment concentration in turbid estuarine system (Seine Estuary, France): Optical turbidity sensors response to suspended sediment characteristics. Mar. Geol. 400, 24–37. https://doi.org/10.1016/j.margeo.2018.03.003

Dyer, K.R., 1974. The salt balance in stratified estuaries. Estuar. Coast. Mar. Sci. 2, 273–281. https://doi.org/10.1016/0302-3524(74)90017-6

Dyer, K.R., 1997. Estuaries: a physical introduction (2nd ed.). John Wiley and Sons, Chichester, pp. 195.

Elliott, M., Day, J.W., Ramachandran, R., Wolanski, E., 2019. A synthesis: What is the future for coasts, estuaries, deltas and other transitional habitats in 2050 and beyond? in: Wolanski, E., Day, J.W., Elliott, M., Ramachandran, R. (Eds.), Coasts and Estuaries: The Future. Elsevier, pp. 1–28.

Familkhalili, R., Talke, S.A., 2016. The effect of channel deepening on tides and storm surge: A case study of Wilmington, NC. Geophys. Res. Lett. 43, 9138–9147. https://doi.org/10.1002/2016GL069494

Familkhalili, R., Talke, S.A., Jay, D.A., 2020. Tide-storm surge interactions in highly altered estuaries: How channel deepening increases surge vulnerability. J. Geophys. Res. Ocean. 125, e2019JC015286. https://doi.org/10.1029/2019JC015286

Festa, J.F., Hansen, D. V., 1978. Turbidity maxima in partially mixed estuaries: A two-dimensional numerical model. Estuar. Coast. Mar. Sci. 7, 347–359. https://doi.org/10.1016/0302-3524(78)90087-7

Fettweis, M., Baeye, M., 2015. Seasonal variation in concentration, size, and settling velocity of muddy marine flocs in the benthic boundary layer. J. Geophys. Res. Ocean. 120, 5648–5667. https://doi.org/10.1002/2014JC010644

Friedrichs, C., 2010. Barotropic tides in channelized estuaries, in: Valle-Levinson, A. (Ed.), Contemporary Issues in Estuarine Physics. Cambridge University Press, Cambridge, UK, pp. 27–61. https://doi.org/10.1017/CBO9780511676567.004

Friedrichs, C.T., 2011. Tidal Flat Morphodynamics: A Synthesis, in: Wolanski, E., McLusky, D. (Eds.), Treatise on Estuarine and Coastal Science. Waltham, MA: Academic, pp. 137–170.

Friedrichs, C.T., Wright, L.D., 1997. Sensitivity of bottom stress and bottom roughness estimates to density stratification, Eckernförde Bay, southern Baltic Sea. J. Geophys. Res. Ocean. 102, 5721–5732. https://doi.org/10.1029/96JC03550

Fugate, D.C., Friedrichs, C.T., 2002. Determining concentration and fall velocity of estuarine particle populations using ADV, OBS and LISST. Cont. Shelf Res. 22, 1867–1886. https://doi.org/10.1016/S0278-4343(02)00043-2

Gatto, V.M., van Prooijen, B.C., Wang, Z.B., 2017. Net sediment transport in tidal basins: Quantifying the tidal barotropic mechanisms in a unified framework. Ocean Dyn. 67, 1385–1406. https://doi.org/10.1007/s10236-017-1099-3

Ge, J., Shen, F., Guo, W., Chen, C., Ding, P., 2015. Estimation of critical shear stress for erosion in the Changjiang Estuary: A synergy research of observation, GOCI sensing and modeling. J. Geophys. Res. Ocean. 120, 8439–8465. https://doi.org/10.1002/2015JC010992

Ge, J., Zhou, Z., Yang, W., Ding, P., Chen, C., Wang, Z.B., Gu, J., 2018. Formation of concentrated benthic suspension in a time-dependent salt wedge estuary. J. Geophys. Res. Ocean. 123, 8581–8607. https://doi.org/10.1029/2018JC013876

Geyer, W.R., 1993. The importance of suppression of turbulence by stratification on the estuarine turbidity maximum. Estuaries 16, 113–125. https://doi.org/10.1007/BF02690231

Geyer, W.R., MacCready, P., 2014. The estuarine circulation. Annu. Rev. Fluid Mech. 46, 175–197. https://doi.org/10.1146/annurev-fluid-010313-141302

Geyer, W.R., Woodruff, J.D., Traykovski, P., 2001. Sediment transport and trapping in the Hudson River estuary. Estuaries 24, 670–679. https://doi.org/10.2307/1352875

Gibbs, R.J., Wolanski, E., 1992. The effect of flocs on optical backscattering measurements of suspended material concentration. Mar. Geol. 107, 289–291. https://doi.org/10.1016/0025-3227(92)90078-V

Grasso, F., Le Hir, P., 2019. Influence of morphological changes on suspended sediment dynamics in a macrotidal estuary: Diachronic analysis in the Seine Estuary (France) from 1960 to 2010. Ocean Dyn. 69, 83–100. https://doi.org/10.1007/s10236-018-1233-x

Gray, J.R., Gartner, J.W., 2010. Technological advances in suspended-sediment surrogate monitoring. Water Resour. Res. 45, W00D29. https://doi.org/10.1029/2008WR007063

Green, M.O., Boon, III, J.D., 1993. The measurement of constituent concentrations of non homogenous sediments suspension using optical backscatter sensors. Mar. Geol. 110, 73–81.

Guerrero, M., Szupiany, R.N., Amsler, M., 2011. Comparison of acoustic backscattering techniques for suspended sediments investigation. Flow Meas. Instrum. 22, 392–401. https://doi.org/10.1016/j.flowmeasinst.2011.06.003

Guo, C., He, Q., Guo, L., Winterwerp, J.C., 2017. A study of in-situ sediment flocculation in the turbidity maxima of the Yangtze Estuary. Estuar. Coast. Shelf Sci. 191, 1–9. https://doi.org/10.1016/j.ecss.2017.04.001

Guo, C., He, Q., van Prooijen, B.C., Guo, L., Manning, A.J., Bass, S., 2018. Investigation of flocculation dynamics under changing hydrodynamic forcing on an intertidal mudflat. Mar. Geol. 395, 120–132. https://doi.org/10.1016/j.margeo.2017.10.001

Guo, L., 2014. Modeling estuarine morphodynamics under combined river and tidal forcing. Ph.D. thesis. Delft University of Technology.

Guo, L., Su, N., Townend, I., Wang, Z.B., Zhu, C., Wang, X., Zhang, Y., He, Q., 2019. From the headwater to the delta: A synthesis of the basin-scale sediment

load regime in the Changjiang River. Earth-Science Rev. 197, 102900. https://doi.org/10.1016/j.earscirev.2019.102900

Guo, L., Su, N., Zhu, C., He, Q., 2018. How have the river discharges and sediment loads changed in the Changjiang River basin downstream of the Three Gorges Dam? J. Hydrol. 560, 259–274. https://doi.org/10.1016/j.jhydrol.2018.03.035

Guo, L., van der Wegen, M., Jay, D.A., Matte, P., Wang, Z.B., Roelvink, D., He, Q., 2015. River-tide dynamics: Exploration of nonstationary and nonlinear tidal behavior in the Yangtze River estuary. J. Geophys. Res. Ocean. 120, 3499–3521. https://doi.org/10.1002/2014JC010491

Guo, L., Xie, W., Xu, F., Wang, X., Zhu, C., Meng, Y., Zhang, W., He, Q., 2021. A historical review of sediment export–import shift in the North Branch of Changjiang Estuary. Earth Surf. Process. Landforms 1–13. https://doi.org/10.1002/esp.5084

Ha, H.K., Hsu, W.Y., Maa, J.P.Y., Shao, Y.Y., Holland, C.W., 2009. Using ADV backscatter strength for measuring suspended cohesive sediment concentration. Cont. Shelf Res. 29, 1310–1316. https://doi.org/10.1016/j.csr.2009.03.001

Ha, H.K., Maa, J.P.Y., 2009. Evaluation of two conflicting paradigms for cohesive sediment deposition. Mar. Geol. 265, 120–129. https://doi.org/10.1016/j.margeo.2009.07.001

Ha, H.K., Maa, J.P.Y., Park, K., Kim, Y.H., 2011. Estimation of high-resolution sediment concentration profiles in bottom boundary layer using pulse-coherent acoustic Doppler current profilers. Mar. Geol. 279, 199–209. https://doi.org/10.1016/j.margeo.2010.11.002

Hansen, D. V., Rattray, M., 1965. Gravitational circulation in straits and estuaries. J. Mar. Res. 23, 104–122.

He, Q., Li, J.F., Li, Y., Jin, X.S., Che, Y., 2001. Field measurements of bottom boundary layer processes and sediment resuspension in the Changjiang Estuary. Sci. China Ser. B 44, 80–86. https://doi.org/Doi 10.1007/Bf02884812

He, Q., Tang, J., Cheng, J., 2008. A study of in situ floc size in turbidity maximum, in: Kusuda, T., Yamanishi, H., Spearman, J., Gailani, J.Z. (Eds.), Sediment and Ecohydraulics: INTERCOH 2005. Elsevier, pp. 287–294.

Hua, X., Huang, H., Wang, Y., Yu, X., Zhao, K., Chen, D., 2020. Seasonal estuarine turbidity maximum under strong tidal dynamics: Three-year observations in the Changjiang River Estuary. Water 12, 1854. https://doi.org/10.3390/w12071854

Huettel, M., Berg, P., Kostka, J.E., 2014. Benthic exchange and biogeochemical cycling in permeable sediments. Ann. Rev. Mar. Sci. 6, 23–51. https://doi.org/10.1146/annurev-marine-051413-012706

Huijts, K.M.H., Schuttelaars, H.M., Swart, H.E. De, Friedrichs, C.T., 2009. Analytical study of the transverse distribution of along-channel and transverse residual flows in tidal estuaries. Cont. Shelf Res. 29, 89–100. https://doi.org/10.1016/j.csr.2007.09.007

Jamieson, G., 1911. Yangtsze-Kiang, in: Chisholm, H. (Ed.), Encyclopædia Britannica (11th ed.). Cambridge Univ. Press. pp. 903.

Jay, D. a., Musiak, J.D., 1994. Particle trapping in estuarine tidal flows. J. Geophys. Res. 99, 20445–20461. https://doi.org/10.1029/94JC00971

Jiang, C., de Swart, H.E., Li, J., Liu, G., 2013. Mechanisms of along-channel sediment transport in the North Passage of the Yangtze Estuary and their response to large-scale interventions. Ocean Dyn. 63, 283–305. https://doi.org/10.1007/s10236-013-0594-4

Karimpour, F., Venayagamoorthy, S.K., 2014. A simple turbulence model for stably stratified wall-bounded flows. J. Geophys. Res. Ocean. 119, 870–880. https://doi.org/10.1002/2013JC009622

Kim, S.C., Friedrichs, C.T., Maa, J.P.Y., Wright, L.D., 2000. Estimating bottom stress in tidal boundary layer from acoustic Doppler velocimeter data. J. Hydraul. Eng. 126, 399–406. https://doi.org/10.1061/(ASCE)0733-9429(2000)126:6(399)

Kineke, G.C., Sternberg, R.W., 1992. Measurements of high concentration suspended sediments using the optical backscatterance sensor. Mar. Geol. 108, 253–258. https://doi.org/10.1016/0025-3227(92)90199-R

Kumar, M., Schuttelaars, H.M., Roos, P.C., 2017. Three-dimensional semi-idealized model for estuarine turbidity maxima in tidally dominated estuaries. Ocean Model. 113, 1–21. https://doi.org/10.1016/j.ocemod.2017.03.005

Lerczak, J.A., Geyer, W.R., 2004. Modeling the lateral circulation in straight, stratified estuaries. J. Phys. Oceanogr. 34, 1410–1428. https://doi.org/10.1175/1520-0485(2004)034<1410:MTLCIS>2.0.CO;2

Lerczak, J.A., Geyer, W.R., Chant, R.J., 2006. Mechanisms driving the time-dependent salt flux in a partially stratified estuary. J. Phys. Oceanogr. 36, 2296–2311. https://doi.org/10.1175/JPO2959.1

Li, J., Zhang, C., 1998. Sediment resuspension and implications for turbidity maximum in the Changjiang Estuary. Mar. Geol. 148, 117–124. https://doi.org/10.1016/S0025-3227(98)00003-6

Li, L., He, Z., Xia, Y., Dou, X., 2018. Dynamics of sediment transport and stratification in Changjiang River Estuary, China. Estuar. Coast. Shelf Sci. 213, 1–17. https://doi.org/10.1016/j.ecss.2018.08.002

Li, L., Ni, J., Chang, F., Yue, Y., Frolova, N., Magritsky, D., Borthwick, A.G.L., Ciais, P., Wang, Y., Zheng, C., Walling, D.E., 2020a. Global trends in water and

sediment fluxes of the world's large rivers. Sci. Bull. 65, 62–69. https://doi.org/10.1016/j.scib.2019.09.012

Li, L., Zhu, J., Chant, R.J., Wang, C., Pareja-Roman, L.F., 2020b. Effect of dikes on saltwater intrusion under various wind conditions in the Changjiang Estuary. J. Geophys. Res. Ocean. 125, e2019JC015685. https://doi.org/10.1029/2019JC015685

Li, M.Z., Gust, G., 2000. Boundary layer dynamics and drag reduction in flows of high cohesive sediment suspensions. Sedimentology 47, 71–86. https://doi.org/10.1046/j.1365-3091.2000.00277.x

Li, X., Zhu, J., Yuan, R., Qiu, C., Wu, H., 2016. Sediment trapping in the Changjiang Estuary: Observations in the North Passage over a spring-neap tidal cycle. Estuar. Coast. Shelf Sci. 177, 8–19. https://doi.org/10.1016/j.ecss.2016.05.004

Li, Y., Jia, J., Zhu, Q., Cheng, P., Gao, S., Wang, Y.P., 2018. Differentiating the effects of advection and resuspension on suspended sediment concentrations in a turbid estuary. Mar. Geol. 403, 179–190. https://doi.org/10.1016/j.margeo.2018.06.001

Li, Y., Wang, Y., Zhu, Q., Limaye, A.B., Wu, H., 2021. Roles of advection and sediment resuspension-settling in the turbidity maximum zone of the Changjiang Estuary, China. Cont. Shelf Res. 229, 104559. https://doi.org/10.1016/j.csr.2021.104559

Li, Z., Jia, J., Wu, Y., Zong, H., Zhang, G., Wang, Y.P., Yang, Y., 2019. Vertical distributions of suspended sediment concentrations in the turbidity maximum zone of the periodically and partially stratified Changjiang Estuary. Estuaries and Coasts 42, 1475–1490. https://doi.org/10.1007/s12237-019-00616-z

Liang, D., Wang, X., Bockelmann-Evans, B.N., Falconer, R.A., 2013. Study on nutrient distribution and interaction with sediments in a macro-tidal estuary. Adv. Water Resour. 52, 207–220. https://doi.org/10.1016/J.ADVWATRES.2012.11.015

Lin, J., He, Q., Guo, L., van Prooijen, B.C., Wang, Z.B., 2020. An integrated optic and acoustic (IOA) approach for measuring suspended sediment concentration in highly turbid environments. Mar. Geol. 421, 106062. https://doi.org/10.1016/j.margeo.2019.106062

Lin, J., van Prooijen, B.C., Guo, L., Zhu, C., He, Q., Wang, Z.B., 2021. Regime shifts in the Changjiang (Yangtze River) Estuary: The role of concentrated benthic suspensions. Mar. Geol. 433, 106403. https://doi.org/10.1016/j.margeo.2020.106403

Little, S., Spencer, K.L., Schuttelaars, H.M., Millward, G.E., Elliott, M., 2017. Unbounded boundaries and shifting baselines: Estuaries and coastal seas in a

rapidly changing world. Estuar. Coast. Shelf Sci. 198, 311–319. https://doi.org/https://doi.org/10.1016/j.ecss.2017.10.010

Liu, G., Zhu, J., Wang, Y., Wu, H., Wu, J., 2011. Tripod measured residual currents and sediment flux: Impacts on the silting of the Deepwater Navigation Channel in the Changjiang Estuary. Estuar. Coast. Shelf Sci. 93, 192–201. https://doi.org/10.1016/j.ecss.2010.08.008

Liu, J., Cheng, H., Han, L., Wang, Z., 2019. Interannual variations on siltation of the 12.5-m deepwater navigation channel in Yangtze Estuary. Adv. Water Sci. 30, 65–75. https://doi.org/10.14042/j.cnki.32.1309.2019.01.007 (in Chinese with English abstract)

Lu, Y., Lueck, R.G., 1999. Using a broadband ADCP in a tidal channel. Part I: Mean flow and shear. J. Atmos. Ocean. Technol. 16, 1556–1567. https://doi.org/10.1175/1520-0426(1999)016<1556:UABAIA>2.0.CO;2

Ludwig, K.A., Hanes, D.M., 1990. A laboratory evaluation of optical backscatterance suspended solids sensors exposed to sand-mud mixtures. Mar. Geol. 94, 173–179. https://doi.org/10.1016/0025-3227(90)90111-V

Maa, J.P.Y., Kim, S.C., 2002. A constant erosion rate model for fine sediment in the York River, Virginia. Environ. Fluid Mech. 1, 345–360. https://doi.org/10.1023/A:1015799926777

Maa, J.P.Y., Xu, J., Victor, M., 1992. Notes on the performance of an optical backscatter sensor for cohesive sediments. Mar. Geol. 104, 215–218. https://doi.org/10.1016/0025-3227(92)90096-Z

MacCready, P., 2011. Calculating estuarine exchange flow using isohaline coordinates. J. Phys. Oceanogr. 41, 1116–1124. https://doi.org/10.1175/2011JPO4517.1

MacCready, P., Geyer, W.R., 2010. Advances in estuarine physics. Ann. Rev. Mar. Sci. 2, 35–58. https://doi.org/10.1146/annurev-marine-120308-081015

Manning, A.J., Langston, W.J., Jonas, P.J.C., 2010. A review of sediment dynamics in the Severn Estuary: Influence of flocculation. Mar. Pollut. Bull. 61, 37–51. https://doi.org/10.1016/j.marpolbul.2009.12.012

McHenry, J.R., Coleman, N.L., Willis, J.C., Murphree, C.E., Bolton, G.C., Sansom, O.W., Gill, A.C., 1967. Performance of nuclear-sediment concentration gauges. Isot. Hydrol. 38, 207–225.

McSweeney, J.M., Chant, R.J., Sommerfield, C.K., 2016. Lateral variability of sediment transport in the Delaware Estuary. J. Geophys. Res. Ocean. 121, 725–744. https://doi.org/10.1002/2015JC010974

McSweeney, J.M., Chant, R.J., Wilkin, J.L., Sommerfield, C.K., 2017. Suspended-sediment impacts on light-limited productivity in the Delaware Estuary.

Estuaries and Coasts 40, 977–993. https://doi.org/10.1007/s12237-016-0200-3

Mehta, A.J., 1988. Laboratory studies on cohesive sediment deposition and erosion, in: Dronkers, J., van Leussen, W. (Eds.), Physical Processes in Estuaries. Springer, Berlin, Heidelberg, pp. 427–445. https://doi.org/10.1007/978-3-642-73691-9_21

Mellor, G.L., Yamada, T., 1974. A hierarchy of turbulence closure models for planetary boundary layers. J. Atmos. Sci. 31, 1791–1806. https://doi.org/10.1175/1520-0469(1974)031<1791:AHOTCM>2.0.CO;2

Merckelbach, L.M., Ridderinkhof, H., 2006. Estimating suspended sediment concentration using backscatterance from an acoustic Doppler profiling current meter at a site with strong tidal currents. Ocean Dyn. 56, 153–168. https://doi.org/10.1007/s10236-005-0036-z

Merten, G.H., Capel, P.D., Minella, J.P.G., 2014. Effects of suspended sediment concentration and grain size on three optical turbidity sensors. J. Soils Sediments 14, 1235–1241. https://doi.org/10.1007/s11368-013-0813-0

Moura, M.G., Quaresma, V.S., Bastos, A.C., Veronez Jr, P., 2011. Field observations of SPM using ADV, ADP, and OBS in a shallow estuarine system with low SPM concentration-Vitória Bay, SE Brazil. Ocean Dyn. 61, 273–283. https://doi.org/10.1007/s10236-010-0364-5

Munk, W.H., Anderson, E.R., 1948. Note on a theory of the thermocline. J. Mar. Res. 7, 276–295.

Nauw, J.J., Merckelbach, L.M., Ridderinkhof, H., van Aken, H.M., 2014. Long-term ferry-based observations of the suspended sediment fluxes through the Marsdiep inlet using acoustic Doppler current profilers. J. Sea Res. 87, 17–29. https://doi.org/10.1016/j.seares.2013.11.013

Neumann, B., Vafeidis, A.T., Zimmermann, J., Nicholls, R.J., 2015. Future coastal population growth and exposure to sea-level rise and coastal flooding - A global assessment. PLoS One 10, e0118571. https://doi.org/10.1371/journal.pone.0118571

Nichols, M.M., 1986. Effects of fine sediment resuspension in estuaries. Springer, New York, pp. 5–42.

Nortek, A.S., 2005. Technical Specification: Vector-300m., https://www.nortekgroup.com/export/pdf/Vector%20-%20300%20m.pdf.

Palomares, M.L.D., Pauly, D., 2019. Coastal fisheries: The past, present, and possible futures, in: Wolanski, E., Day, J.W., Elliott, M., Ramachandran, R. (Eds.), Coasts and Estuaries: The Future. Elsevier, pp. 569–576. https://doi.org/10.1016/B978-0-12-814003-1.00032-0

Parmesan, C., Burrows, M.T., Duarte, C.M., Poloczanska, E.S., Richardson, A.J., Schoeman, D.S., Singer, M.C., 2013. Beyond climate change attribution in conservation and ecological research. Ecol. Lett. 16, 58–71. https://doi.org/10.1111/ele.12098

Pearson, S.G., Verney, R., van Prooijen, B.C., Tran, D., Hendriks, E.C.M., Jacquet, M., Wang, Z.B., 2021. Characterizing the composition of sand and mud suspensions in coastal and estuarine environments using combined optical and acoustic measurements. J. Geophys. Res. Ocean. 126, e2021JC017354. https://doi.org/10.1029/2021jc017354

Postma, H., 1954. Hydrography of the Dutch Wadden Sea. Ph.D. thesis. Groningen University.

Postma, H., Kalle, H., 1955. Die Entstehung von Trübungszonen im Unterlauf der Flüsse, speziell im Hinblick auf die Verhältnisse in der UnterElbe. Dtsch. Hydrogr. Z8, 137–144.

Pritchard, D., 2005. Suspended sediment transport along an idealised tidal embayment: Settling lag, residual transport and the interpretation of tidal signals. Ocean Dyn. 55, 124–136. https://doi.org/10.1007/s10236-005-0004-7

Pritchard, D.W., 1967. What is an estuary: A physical viewpoint. American Association for the Advancement of Science, 83: 3–5.

Pu, X., Shi, J.Z., Hu, G.D., Xiong, L.B., 2015. Circulation and mixing along the North Passage in the Changjiang River Estuary, China. J. Mar. Syst. 148, 213–235. https://doi.org/10.1016/j.jmarsys.2015.03.009

Rai, A.K., Kumar, A., 2015. Continuous measurement of suspended sediment concentration: Technological advancement and future outlook. Measurement 76, 209–227. https://doi.org/10.1016/j.measurement.2015.08.013

Ralston, D.K., Geyer, W.R., 2019. Response to channel deepening of the salinity intrusion, estuarine circulation, and stratification in an urbanized estuary. J. Geophys. Res. Ocean. 124, 4784–4802. https://doi.org/10.1029/2019JC015006

Ralston, D.K., Talke, S., Geyer, W.R., Al-Zubaidi, H.A.M., Sommerfield, C.K., 2019. Bigger tides, less flooding: Effects of dredging on barotropic dynamics in a highly modified estuary. J. Geophys. Res. Ocean. 124, 196–211. https://doi.org/10.1029/2018JC014313

Rockström, J., Steffen, W., Noone, K., Persson, Å., Chapin, F.S., Lambin, E.F., Lenton, T.M., Scheffer, M., Folke, C., Schellnhuber, H.J., Nykvist, B., de Wit, C.A., Hughes, T., van der Leeuw, S., Rodhe, H., Sörlin, S., Snyder, P.K., Costanza, R., Svedin, U., Falkenmark, M., Karlberg, L., Corell, R.W., Fabry, V.J., Hansen, J., Walker, B., Liverman, D., Richardson, K., Crutzen, P., Foley, J.A., 2009. A safe operating space for humanity. Nature 461, 472–475.

Rymszewicz, A., O'Sullivan, J.J., Bruen, M., Turner, J.N., Lawler, D.M., Conroy, E., Kelly-Quinn, M., 2017. Measurement differences between turbidity instruments, and their implications for suspended sediment concentration and load calculations: A sensor inter-comparison study. J. Environ. Manage. 199, 99–108. https://doi.org/10.1016/j.jenvman.2017.05.017

Sahin, C., Safak, I., Hsu, T.J., Sheremet, A., 2013. Observations of suspended sediment stratification from acoustic backscatter in muddy environments. Mar. Geol. 336, 24–32. https://doi.org/10.1016/j.margeo.2012.12.001

Salehi, M., Strom, K., 2011. Using velocimeter signal to noise ratio as a surrogate measure of suspended mud concentration. Cont. Shelf Res. 31, 1020–1032. https://doi.org/10.1016/j.csr.2011.03.008

Scheu, K.R., Fong, D.A., Monismith, S.G., Fringer, O.B., 2015. Sediment transport dynamics near a river inflow in a large alpine lake. Limnol. Oceanogr. 60, 1195–1211. https://doi.org/10.1002/lno.10089

Schulz, E., Schuttelaars, H.M., Gräwe, U., Burchard, H., 2015. Impact of the depth-to-width ratio of periodically stratified tidal channels on the estuarine circulation. J. Phys. Oceanogr. 45, 2048–2069. https://doi.org/10.1175/JPO-D-14-0084.1

Scully, M.E., Friedrichs, C.T., 2003. The influence of asymmetries in overlying stratification on near-bed turbulence and sediment suspension in a partially mixed estuary. Ocean Dyn. 53, 208–219. https://doi.org/10.1007/s10236-003-0034-y

Scully, M.E., Friedrichs, C.T., 2007. Sediment pumping by tidal asymmetry in a partially mixed estuary. J. Geophys. Res. Ocean. 112, C07028. https://doi.org/10.1029/2006JC003784

Shao, Y., Maa, J.P.Y., 2017. Comparisons of different instruments for measuring suspended cohesive sediment concentrations. Water 9, 968. https://doi.org/10.3390/w9120968

Shen, H.T., He, S.L., Pan, D.A., 1993. Study on turbidity maximum in the South and North Passages of the Changjiang Estuary, in: Su, J.L. (Ed.), Proceedings of the Symposium on the Physical and Chemical Oceanography of the China Seas. China Ocean Press, Beijing, pp. 237–243.

Shen, H.T., Zhu, H.F., Mao, Z.C., 1982. Circulation of the Changjiang and its effect on the transport of suspended sediment, in: Kennedy, V.S. (Ed.), Estuarine Comparisons. Academic Press, New York, pp. 677–691.

Shen, Q., Huang, W., Wan, Y., Gu, F., Qi, D., 2020. Observation of the sediment trapping during flood season in the deep-water navigational channel of the Changjiang Estuary, China. Estuar. Coast. Shelf Sci. 237, 106632. https://doi.org/10.1016/j.ecss.2020.106632

Shi, J.Z., 2010. Tidal resuspension and transport processes of fine sediment within the river plume in the partially-mixed Changjiang River estuary, China: A personal perspective. Geomorphology 121, 133–151. https://doi.org/10.1016/j.geomorph.2010.04.021

Shi, J.Z., Zhang, S.Y., Hamilton, L.J., 2006. Bottom fine sediment boundary layer and transport processes at the mouth of the Changjiang Estuary, China. J. Hydrol. 327, 276–288. https://doi.org/10.1016/j.jhydrol.2005.11.039

Shi, Z., 2004. Behaviour of fine suspended sediment at the North passage of the Changjiang Estuary, China. J. Hydrol. 293, 180–190. https://doi.org/10.1016/j.jhydrol.2004.01.014

Simpson, J.H., Brown, J., Matthews, J., Allen, G., 1990. Tidal straining, density currents, and stirring in the control of estuarine stratification. Estuaries 13, 125–132. https://doi.org/10.2307/1351581

Song, D., Wang, X.H., 2013. Suspended sediment transport in the Deepwater Navigation Channel, Yangtze River Estuary, China, in the dry season 2009: 2. Numerical simulations. J. Geophys. Res. Ocean. 118, 5568–5590. https://doi.org/10.1002/jgrc.20411

Song, D., Wang, X.H., Cao, Z., Guan, W., 2013. Suspended sediment transport in the Deepwater Navigation Channel, Yangtze River Estuary, China, in the dry season 2009: 1. Observations over spring and neap tidal cycles. J. Geophys. Res. Ocean. 118, 5555–5567. https://doi.org/10.1002/jgrc.20410

Soulsby, R.L., 1983. The bottom boundary layer of shelf seas, in: Johns, B. (Ed.), Physical Oceanography of Coastal and Shelf Seas, Elsevier Oceanography Series. Elsevier, Amsterdam, pp. 189–266. https://doi.org/10.1016/S0422-9894(08)70503-8

Stacey, M.T., 1996. Turbulent mixing and residual circulation in a partially stratified estuary. Ph.D. thesis. Stanford University.

Stapleton, K.R., Huntley, D.A., 1995. Seabed stress determinations using the intertial dissipation method and the turbulent kinetic energy method. Earth Surf. Process. Landforms 20, 807–815. https://doi.org/10.1002/esp.3290200906

Steffen, W., Crutzen, P.J., McNeill, J.R., 2007. The Anthropocene: Are humans now overwhelming the great forces of nature? AMBIO A J. Hum. Environ. 36, 614–621. https://doi.org/10.1579/0044-7447(2007)36[614:TAAHNO]2.0.CO;2

Su, J., Wang, K., 1986. The suspended sediment balance in Changjiang estuary. Estuar. Coast. Shelf Sci. 23, 81–98. https://doi.org/10.1016/0272-7714(86)90086-7

Su, M., Yao, P., Wang, Z., Zhang, C., Chen, Y., Stive, M.J.F., 2016. Conversion of electro-optical signals to sediment concentration in a silt–sand suspension

environment. Coast. Eng. 114, 284–294. https://doi.org/10.1016/j.coastaleng.2016.04.014

Syvitski, J.P.M., Vörösmarty, C.J., Kettner, A.J., Green, P., 2005. Impact of humans on the flux of terrestrial sediment to the global coastal ocean. Science 308, 376–380. https://doi.org/10.1126/science.1109454

Talke, S.A., de Swart, H.E., de Jonge, V.N., 2009a. An idealized model and systematic process study of oxygen depletion in highly turbid estuaries. Estuaries and Coasts 32, 602–620. https://doi.org/10.1007/s12237-009-9171-y

Talke, S.A., de Swart, H.E., Schuttelaars, H.M., 2009b. Feedback between residual circulations and sediment distribution in highly turbid estuaries: An analytical model. Cont. Shelf Res. 29, 119–135. https://doi.org/10.1016/j.csr.2007.09.002

Talke, S.A., Jay, D.A., 2020. Changing tides: The role of natural and anthropogenic factors. Ann. Rev. Mar. Sci. 12, 121–151. https://doi.org/10.1146/annurev-marine-010419-010727

Talke, S.A., Orton, P., Jay, D.A., 2014. Increasing storm tides in New York Harbor, 1844–2013. Geophys. Res. Lett. 41, 3149–3155. https://doi.org/10.1002/2014GL059574

Thompson, C.E.L., Amos, C.L., Angelaki, M., Jones, T.E.R., Binks, C.E., 2006. An evaluation of bed shear stress under turbid flows. J. Geophys. Res. Ocean. 111, C04008. https://doi.org/10.1029/2005JC003287

Thorne, P.D., Hanes, D.M., 2002. A review of acoustic measurement of small-scale sediment processes. Cont. Shelf Res. 22, 603–632. https://doi.org/10.1016/S0278-4343(01)00101-7

Uncles, R.J., Elliott, R.C.A., Weston, S.A., 1985. Dispersion of salt and suspended sediment in a partially mixed estuary. Estuaries 8, 256–269. https://doi.org/10.1016/0272-7714(85)90035-6

Uncles, R.J., Joint, I., Stephens, J.A., 1998. Transport and retention of suspended particulate matter and bacteria in the Humber-Ouse Estuary, United Kingdom, and their relationship to hypoxia and anoxia. Estaurine Coast. Shelf Sci. 21, 597–612. https://doi.org/10.2307/1353298

Valle-Levinson, A., 2010. Definition and classification of estuaries, in: Valle-Levinson, A. (Ed.), Contemporary issues in estuarine physics. pp. 1–11.

van Kessel, T., Winterwerp, H., van Prooijen, B., van Ledden, M., Borst, W., 2011. Modelling the seasonal dynamics of SPM with a simple algorithm for the buffering of fines in a sandy seabed. Cont. Shelf Res. 31, S124–S134. https://doi.org/10.1016/j.csr.2010.04.008

van Koningsveld, M., Verheij, H.J., Taneja, P., de Vriend, H.J., 2021. Ports and Waterways: Navigating the changing world. TU Delft Open. https://doi.org/10.5074/T.2021.004

van Maren, D.S., Oost, A.P., Wang, Z.B., Vos, P.C., 2016. The effect of land reclamations and sediment extraction on the suspended sediment concentration in the Ems Estuary. Mar. Geol. 376, 147–157. https://doi.org/10.1016/j.margeo.2016.03.007

van Maren, D.S., Winterwerp, J.C., Vroom, J., 2015. Fine sediment transport into the hyper-turbid lower Ems River: The role of channel deepening and sediment-induced drag reduction. Ocean Dyn. 65, 589–605. https://doi.org/10.1007/s10236-015-0821-2

van Straaten, L.V., Kuenen, P.H., 1957. Accumulation of fine grained sediments in the Dutch Wadden Sea. Geologie Mijnb, 19, 329–354.

Vijverberg, T., Winterwerp, J.C., Aarninkhof, S.G.J., Drost, H., 2011. Fine sediment dynamics in a shallow lake and implication for design of hydraulic works. Ocean Dyn. 61, 187–202. https://doi.org/10.1007/s10236-010-0322-2

Wan, Y., 2015. Multiscale physical processes of fine sediment in an estuary, Ph.D. thesis. Delft University of Technology.

Wan, Y., Roelvink, D., Li, W., Qi, D., Gu, F., 2014. Observation and modeling of the storm-induced fluid mud dynamics in a muddy-estuarine navigational channel. Geomorphology 217, 23–36. https://doi.org/10.1016/j.geomorph.2014.03.050

Wan, Y., Wang, L., 2017. Numerical investigation of the factors influencing the vertical profiles of current, salinity, and SSC within a turbidity maximum zone. Int. J. Sediment Res. 32, 20–33. https://doi.org/10.1016/j.ijsrc.2016.07.003

Wan, Y., Wu, H., Roelvink, D., Gu, F., 2015. Experimental study on fall velocity of fine sediment in the Yangtze Estuary, China. Ocean Eng. 103, 180–187. https://doi.org/10.1016/j.oceaneng.2015.04.076

Wan, Y., Zhao, D., 2017. Observation of saltwater intrusion and ETM dynamics in a stably stratified estuary: The Yangtze Estuary, China. Environ. Monit. Assess. 189, 89. https://doi.org/10.1007/s10661-017-5797-6

Wang, L., 2010. Tide driven dynamics of subaqueous fluid mud layers in turbidity maximum zones of German estuaries, Ph.D. thesis. University of Bremen.

Wang, X.H., 2002. Tide-induced sediment resuspension and the bottom boundary layer in an idealized estuary with a muddy bed. J. Phys. Oceanogr. 32, 3113–3131. https://doi.org/10.1175/1520-0485(2002)032<3113:TISRAT>2.0.CO;2

Wang, Y., Shen, J., He, Q., 2010. A numerical model study of the transport timescale and change of estuarine circulation due to waterway constructions in the

Changjiang Estuary, China. J. Mar. Syst. 82, 154–170. https://doi.org/10.1016/j.jmarsys.2010.04.012

Wang, Y., Yu, Q., Gao, S., 2011. Relationship between bed shear stress and suspended sediment concentration: Annular flume experiments. Int. J. Sediment Res. 26, 513–523. https://doi.org/10.1016/S1001-6279(12)60009-2

Wang, Y.P., Voulgaris, G., Li, Y., Yang, Y., Gao, J., Chen, J., Gao, S., 2013. Sediment resuspension, flocculation, and settling in a macrotidal estuary. J. Geophys. Res. Ocean. 118, 5591–5608. https://doi.org/10.1002/jgrc.20340

Wang, Z.Y., Larsen, P., Nestmann, F., Dittrich, A., 1998. Resistance and drag reduction of flows of clay suspensions. J. Hydraul. Eng. 124, 41–49. https://doi.org/10.1061/(ASCE)0733-9429(1998)124:1(41)

Waters, C.N., Zalasiewicz, J., Summerhayes, C., Barnosky, A.D., Poirier, C., Ga, A., Cearreta, A., Edgeworth, M., Ellis, E.C., Ellis, M., Jeandel, C., Leinfelder, R., Mcneill, J.R., Richter, D., Steffen, W., Syvitski, J., Vidas, D., Wagreich, M., Williams, M., Zhisheng, A., Grinevald, J., Odada, E., Oreskes, N., Wolfe, A.P., 2016. The Anthropocene is functionally and stratigraphically distinct from the Holocene. Science 351, aad2622. https://doi.org/10.1126/science.aad2622

Wei, X., Kumar, M., Schuttelaars, H.M., 2018. Three-dimensional sediment dynamics in well-mixed estuaries: Importance of the internally generated overtide, spatial settling lag, and gravitational circulation. J. Geophys. Res. Ocean. 123, 1062–1090. https://doi.org/10.1002/2017JC012857

Winterwerp, J.C., 2001. Stratification effects by cohesive and noncohesive sediment. J. Geophys. Res. 106, 22559–22574. https://doi.org/10.1029/2000JC000435

Winterwerp, J.C., 2002. Scaling parameters for high-concentrated mud suspensions in tidal flow. Proc. Mar. Sci. 5, 171–186. https://doi.org/10.1016/S1568-2692(02)80015-8

Winterwerp, J.C., 2011. Fine sediment transport by tidal asymmetry in the high-concentrated Ems River: Indications for a regime shift in response to channel deepening. Ocean Dyn. 61, 203–215. https://doi.org/10.1007/s10236-010-0332-0

Winterwerp, J.C., Lely, M., He, Q., 2009. Sediment-induced buoyancy destruction and drag reduction in estuaries. Ocean Dyn. 59, 781–791. https://doi.org/10.1007/s10236-009-0237-y

Winterwerp, J.C., Vroom, J., Wang, Z.B., Krebs, M., Hendriks, E.C.M., van Maren, D.S., Schrottke, K., Borgsmüller, C., Schöl, A., 2017. SPM response to tide and river flow in the hyper-turbid Ems River. Ocean Dyn. 67, 559–583. https://doi.org/10.1007/s10236-017-1043-6

Winterwerp, J.C., Wang, Z.B., 2013. Man-induced regime shifts in small estuaries-I: Theory. Ocean Dyn. 63, 1279–1292. https://doi.org/10.1007/s10236-013-0662-9

Winterwerp, J.C., Wang, Z.B., van Braeckel, A., van Holland, G., Kösters, F., 2013. Man-induced regime shifts in small estuaries-II: A comparison of rivers. Ocean Dyn. 63, 1293–1306. https://doi.org/10.1007/s10236-013-0663-8

Wolanski, E., Day, J.W., Elliott, M., Ramachandran, R., 2019. Coasts and estuaries: The future. Elsevier.

Wolf, J., 1999. The estimation of shear stresses from near-bed turbulent velocities for combined wave-current flows. Coast. Eng. 37, 529–543. https://doi.org/10.1016/S0378-3839(99)00042-3

Wren, B.D.G., Barkdoll, B.D., Kuhnle, R. a, Derrow, R.W., 2000. Field techniques for suspended-sediment measurement. J. Hydraul. Eng. 126, 97–104.

Wu, J., Liu, H., Ren, J., Deng, J., 2011. Cyclonic spirals in tidally accelerating bottom boundary layers in the Zhujiang (Pearl River) Estuary. J. Phys. Oceanogr. 41, 1209–1226. https://doi.org/10.1175/2011JPO4565.1

Wu, J., Liu, J.T., Wang, X., 2012. Sediment trapping of turbidity maxima in the Changjiang Estuary. Mar. Geol. 303–306, 14–25. https://doi.org/10.1016/j.margeo.2012.02.011

Xing, C., 2016. A study on hydrodynamics and sediment transport dynamics between flats and channels in estuary-a case study of North Passage mouth region in the Yangtze Estuary, MSc thesis. East China Normal University, China. (in Chinese with English abstract).

Xu, J., 2009. Study on near bottom dynamics and sediment processes in turbidity maximum. Master thesis. East China Normal University, China. (in Chinese with English abstract).

Yang, Y., Wang, Y.P., Gao, S., Wang, X.H., Shi, B.W., Zhou, L., Wang, D.D., Dai, C., Li, G.C., 2016. Sediment resuspension in tidally dominated coastal environments: New insights into the threshold for initial movement. Ocean Dyn. 66, 401–417. https://doi.org/10.1007/s10236-016-0930-6

Yoshiyama, K., Sharp, J.H., 2006. Phytoplankton response to nutrient enrichment in an urbanized estuary: Apparent inhibition of primary production by overeutrophication. Limnol. Oceanogr. 51, 424–434. https://doi.org/10.4319/lo.2006.51.1_part_2.0424

YSI Incorporated, 2012. User Manual: 6-Series Multiparameter Water Quality Sondes., https://www.ysi.com/File%20Library/Documents/Manuals/069300-YSI-6-Series-Manual-RevJ.pdf.

Zhang, M., Townend, I.H., Cai, H., Zhou, Y., 2016. Seasonal variation of tidal prism and energy in the Changjiang River estuary: A numerical study. Chinese J. Oceanol. Limnol. 34, 219–230. https://doi.org/10.1007/s00343-015-4302-8

Zhao, J., Guo, L., He, Q., Wang, Z.B., van Maren, D.S., Wang, X., 2018. An analysis on half century morphological changes in the Changjiang Estuary: Spatial variability under natural processes and human intervention. J. Mar. Syst. 181, 25–36. https://doi.org/10.1016/j.jmarsys.2018.01.007

Zhou, Z., Ge, J., van Maren, D.S., Wang, Z.B., Kuai, Y., Ding, P., 2021. Study of sediment transport in a tidal channel-shoal system: Lateral effects and slack-water dynamics. J. Geophys. Res. Ocean. 126, e2020JC016334. https://doi.org/10.1029/2020JC016334

Zhou, Z., Ge, J., Wang, Z.B., van Maren, D.S., Ma, J., Ding, P., 2019. Study of lateral flow in a stratified tidal channel-shoal system: The importance of intratidal salinity variation. J. Geophys. Res. Ocean. 124, 6702–6719. https://doi.org/10.1029/2019jc015307

Zhu, C., Guo, L., van Maren, D.S., Tian, B., Wang, X., He, Q., Wang, Z.B., 2019. Decadal morphological evolution of the mouth zone of the Yangtze Estuary in response to human interventions. Earth Surf. Process. Landforms 44, 2319–2332. https://doi.org/10.1002/esp.4647

Zhu, C., Guo, L., van Maren, D.S., Wang, Z.B., He, Q., 2021a. Exploration of decadal tidal evolution in response to morphological and sedimentary changes in the Yangtze Estuary. J. Geophys. Res. Ocean. 126, e2020JC017019. https://doi.org/10.1029/2020JC017019

Zhu, C., van Maren, D.S., Guo, L., Lin, J., He, Q., Wang, Z.B., 2021b. Effects of sediment-induced density gradients on the estuarine turbidity maximum in the Yangtze Estuary. J. Geophys. Res. Ocean. 126, e2020JC016927. https://doi.org/10.1029/2020JC016927

Zhu, J., Ding, P., Zhang, L., Wu, H., Cao, H., 2006. Influence of the deep waterway project on the Changjiang Estuary, in: Wolanski, E. (Ed.), The Environment in Asia Pacific Harbours. Springer, Dordrecht, pp. 79–92. https://doi.org/10.1007/1-4020-3655-8_6

Zhu, L., He, Q., Shen, J., 2018. Modeling lateral circulation and its influence on the along-channel flow in a branched estuary. Ocean Dyn. 68, 177–191. https://doi.org/10.1007/s10236-017-1114-8

Zhu, Q., van Prooijen, B.C., Wang, Z.B., Ma, Y.X., Yang, S.L., 2016. Bed shear stress estimation on an open intertidal flat using in situ measurements. Estuar. Coast. Shelf Sci. 182, 190–201. https://doi.org/10.1016/j.ecss.2016.08.028

# About the Author

Jianliang Lin was born on 30 July 1991 in Foshan, Guangdong Province, southern China. He studied Marine Science and Coastal Engineering for a bachelor's degree at Sun Yat-Sen University (SYSU) from 2010 to 2014. After graduation, he joined Prof. Qing He's group and started his PhD research in the State Key Laboratory of Estuarine and Coastal Research at East China Normal University (ECNU). His work focused on the transport and fate of high-concentrated suspensions in the Changjiang Estuary. In 2017, he participated in the project 'Coping with deltas in transition' within the Programme of Strategic Scientific Alliance between China (No. 2016YFE0133700) and The Netherlands (No. PSA-SA-E-02). He won a scholarship from the China Scholarship Council (No. 201706140180) and started his PhD study in the Netherlands in October 2017. His PhD is within the framework of Joint Doctoral Supervision and Dual Diploma between Delft University of Technology and ECNU. Since then, he has been working on estuarine sediment dynamics and their response to human interventions (e.g., deepening and narrowing) and declined fluvial sediment supply.

# List of Publications

**Jianliang Lin**, Qing He, Leicheng Guo, Bram C van Prooijen, and Zheng Bing Wang. 2020. An Integrated Optic and Acoustic (IOA) Approach for Measuring Suspended Sediment Concentration in Highly Turbid Environments. Marine Geology 421: 106062. doi:10.1016/j.margeo.2019.106062.

**Jianliang Lin**, Bram C. van Prooijen, Leicheng Guo, Chunyan Zhu, Qing He, and Zheng Bing Wang. 2021. Regime Shifts in the Changjiang (Yangtze River) Estuary: The Role of Concentrated Benthic Suspensions. Marine Geology 433: 106403. doi: 10.1016/j.margeo.2020.106403.

**Jianliang Lin**, Bram C. van Prooijen, Chunyan Zhu, Leicheng Guo, Qing He, and Zheng Bing Wang. 2021. Response of estuarine circulation, stratification and sediment transport to deepening and narrowing. (Submitted).

Chunyan Zhu, Dirk Sebastiaan van Maren, Leicheng Guo, **Jianliang Lin**, Qing He, and Zheng Bing Wang. 2021. Feedback effects of sediment suspensions on transport mechanisms in an estuarine turbidity maximum. Journal of Geophysical Research: Oceans. doi: 10.1029/2021JC018029

Chunyan Zhu, Dirk Sebastiaan van Maren, Leicheng Guo, **Jianliang Lin**, Qing He, and Zheng Bing Wang. 2021. Effects of Sediment-Induced Density Gradients on the Estuarine Turbidity Maximum in the Yangtze Estuary. Journal of Geophysical Research: Oceans 126 (5). doi:10.1029/2020JC016927.

Jie Jiang, Qing He, Jian Shen, **Jianliang Lin**, Leicheng Guo, Zhong Peng, and Weiming Xie. 2021. Field data reveal strong storm wave impact on sediment transport in the North Passage of the Changjiang Estuary. (Submitted).

**Jianliang Lin**, Qing He, Qingshu Yang, Feng Liu and Zhirui Deng. 2017. Study on sediment flocculation mechanism at Modaomen in the Pearl River Estuary in flood season. Journal of Sediment Research 42(1): 60-67. doi: 10.16239/j.cnki.0468-155x.2017.01.010. (In Chinese with English abstract)

Jian Dong, Qing He, **Jianliang Lin**, Jiamin Chen, Simin Zhou, Fan Xu, Weiming Xie, and Leicheng Guo. 2021. The distribution of suspended sediment grain size in Yangtze Estuary turbidity maximum zone during the catastrophic flood. (Submitted, in Chinese with English abstract).

Jie Jiang, Qing He, Lei Zhu, and **Jianliang Lin**. 2019. Analysis of hydrodynamic features of the North Passage in the turbidity maximum, Changjiang Estuary. Acta Oceanologica Sinica 41(1): 11-20. doi: 10.3969/j.issn.0253-4193.2019.01.003. (In Chinese with English abstract)

Yu Chen, Qing He, Yuning Zhang, and **Jianliang Lin**. 2019. Grain size distribution of suspended sediment in Yangtze River estuary turbidity maximum in wet season. Journal of Sediment Research 44(5): 47-54. doi: 10.16239/j.cnki.0468-155x.2019.05.008. (In Chinese with English abstract)

Zhirui Deng, Qing He, Qingshu Yang, and **Jianliang Lin**. 2015. Observations of in

situ flocs characteristic in the Modaomen Estuary of the Pearl River. Acta Oceanologica Sinica 37(9): 152-161. doi: 10.3969/j.issn.0253-4193.2015.09.015. (In Chinese with English abstract)

**Jianliang Lin**, Qing He, Leicheng Guo, and Chao Guo. 2016. Sediment trapping mechanics in the turbidity maximum of the Yangtze Estuary. 18th Physics of Estuaries and Coastal Seas Conference. Den Hague, the Netherlands.

**Jianliang Lin**, Qing He, Leicheng Guo, Bram C van Prooijen, and Zheng Bing Wang. 2019. How to obtain reliable high-resolution profiles of suspended sediment concentration in highly turbid environments. 15th International Conference on Cohesive Sediment Transport Processes. İstanbul, Turkey.

# Acknowledgements

This doctoral dissertation is the result of a collaborative research project entitled "Coping with Deltas in Transition", funded by the Ministry of Science and Technology of the People's Republic of China (No. 2016YFE0133700) and the Royal Netherlands Academy of Arts and Sciences (KNAW, No. PSA-SA-E-02) within the Programme of Strategic Scientific Alliance between China and the Netherlands. This work was also partly supported by National Nature Science Foundation of China (Nos. 51739005, U2040216, 41876091, 51909101, 42006150) and Shanghai Committee of Science and Technology (Nos. 20DZ1204700; 21230750600). I have been able to study in Delft for the past four years within the framework of the Joint Doctoral Supervision and Dual Diploma between East China Normal University (ECNU) and Delft University of Technology. These projects and the China Scholarship Council (CSC, No. 201706140180) are much appreciated for supporting my life and study.

Conducting my doctoral research in the Netherlands was a truly unforgettable event in my life. It allowed me access to a worldwide academic environment and exposed me to new ways of thinking, life, and cultural traditions. Although this experience had a few difficult times, all efforts were repaid with the completion of this thesis. This accomplishment was made possible by the assistance and participation of many individuals. Therefore, I would like to convey my appreciation to those who have significantly contributed to my research and who have led, encouraged, and accompanied me throughout the years.

First, departments and institutions that provided data for this dissertation are appreciated, such as Shanghai Dredging Corporation of the Ministry of Transport of the People's Republic of China, the Navigation Guarantee Department of Chinese Navy Headquarters, the Yangtze Estuary Waterway Administration Bureau, and the State Key Laboratory of Estuarine and Coastal Research (SKLEC) at ECNU.

Special thanks go to Prof. He Qing, who initiated this PhD project as my promotor at ECNU. Your encouragement motivates me to do coastal and estuarine research. I am grateful for your thorough guidance in becoming a "professional scientist" (i.e., making a livelihood with science), including research planning, field observations, presentation, international collaboration and student supervision. Thank you for giving me all possibilities and freedoms within this doctoral project. They helped me become a proactive and independent researcher.

Prof. Zheng Bing Wang, one of my promotors at TU Delft, is sincerely acknowledged for his insightful advice, thoughtful guidance, and inspiration. Your support with my

CSC scholarship application and my life in Delft is greatly appreciated. Your expertise and expansive vision kept me on the right track, while your comprehensive assessments and comments elevated our work. In addition, your rigorous academic attitude, such as always looking for the "true" facts and mechanisms, inspired me throughout my PhD. I believe this attitude will lead me in my academic career and life.

Dr. Bram C. van Prooijen, who has been involved in my study PhD project as one of my promotors at TU Delft and a "super" daily supervisor, deserves my deepest gratitude. Thank you for your expertise, support, patience and time in helping me stay on track and correcting my writing. Your detailed comments and suggestions taught me a great deal, such as writing with simple words and presenting academic concepts delicately. In addition, each time I met with you, I felt so driven and inspired. Even a brief conversation with you can illuminate the darkness for me.

Wang yuanye, Gu Jinghua, Zhang Wenxiang, Zhao Jie, Zhu Lei, Zhang Dai, Xie Weiming, Guo Chao, Chen Yu, Deng Zhirui, Xing Chaofeng, Zhu Chunyan, Jiang Jie, Shen Yi, Zhang Yuning and Sun Jianwei are acknowledged for their technical assistance with fieldwork and data gathering. Conversations with Han Winterwerp, Ian Townend, Bas van Maren, Huib de Swart, Henk Schuttelaars, Yoeri Dijkstra, Shen Jian, Jerome Ping-Ya Maa, Jin Liu, Guo Leicheng, Peng Zhong, Wang Xianye, Xie Weiming, Xu Fan, etc. have also inspire me in this work. Edward Anthony and anonymous reviewers are thanked for their helpful comments and suggestions on Chapters 2 and 3. My sincere gratitude goes to the committee for their insightful evaluation and comments on this thesis. In addition, my BSc supervisor Prof. Yang Qingshu, Liu Feng, and Cai Huayang are recognized for their continuous encouragement and care in my career.

I could not complete my PhD without the assistance of my colleagues. Many colleagues at TU Delft, including Lodewijk, Irene, Stuart, Erik, Ana, Jill, Liu Sien, Zhang Rong, Zhou Yang, Li Runxiang, Zhu Chunyan, Kuai Yu, Zhan Yujian, Zhou Zaiyang, Zhang Yuning, Sun Jianwei, etc., and colleagues at SKLEC, e.g., Zhao Jie, Zhu Lei, Zhang Dai, Xie Weiming, Guo Chao, Chen Yu, Deng Zhirui, Xing Chaofeng, Zhu Chunyan, Jiang Jie, Shen Yi, Zhang Yuning, Sun Jianwei, Liu Shuai, Yu Shang and Zhou Simin are acknowledged for pleasant conversations and help. I appreciate the assistance of Inge, Otti and Eefke throughout my time in Delft. During my time in Shanghai, I am grateful to Jin Can, Huo Xiaoli, Tan Li, Li Junhong, Jiang Hong, Li Wei, Zhang Guoan, Zhao Changqing, Pu Meiyan, etc., for their support.

Numerous hot pot, BBQ, and sports (volleyball, basketball and badminton) friends in the Netherlands and China (beyond a name list I can make) are valued for sharing enjoyable and relaxing times with me. These moments are like a beam of sunlight amid the gloom, providing me with vigour and fervour through times of frustration and despondency. Best wishes to all of you wherever you are.

I always have unconditional support and love from my family. Thanks to my parents and in-laws for supporting me in pursuing my dreams and always being there when I need them. Thank you for accompanying and caring for my parents and in-laws, my older brother, sister-in-law, and brother-in-law. Your efforts reduce my concerns about studying overseas. Thank you, lovely nieces, for reminding me of the joys of exploration and discovery during our facetime. Finally, I owe my deepest gratitude to my wife, He Xiaoyan. Thank you for your love and support since high school, for always being the first to listen to my ideas and presentations, and for motivating me to become a better version of myself.

在我的个人生活中，我一直被家人的支持和无条件的爱所祝福。感谢我的父母和岳父母支持我追求梦想，并总在我需要的时候给予我鼓励。谢谢我的大哥，大嫂和小舅子！感谢你们一直陪伴和照顾我的父母和岳父岳母，你们的付出消除了我出国留学时的后顾之忧。谢谢我三个可爱的小侄女！每一次与你们的视频通话都提醒着我应该童真地探索这个世界以及享受发现新事物的乐趣。最后，我要衷心感谢我的妻子何肖妍女士！感谢你自高中开始的支持与爱护，也谢谢你一直愿意当我的想法和演讲的第一位听众，并激励我成为更好的自己。

*Jianliang Lin*

*Delft, June 2022*